He, Jiabao (2005) Functional brain imaging with fMRI and MEG. PhD thesis, University of Nottingham.

Access from the University of Nottingham repository:
http://eprints.nottingham.ac.uk/12371/1/431336.pdf

Copyright and reuse:

The Nottingham ePrints service makes this work by researchers of the University of Nottingham available open access under the following conditions.

- Copyright and all moral rights to the version of the paper presented here belong to the individual author(s) and/or other copyright owners.
- To the extent reasonable and practicable the material made available in Nottingham ePrints has been checked for eligibility before being made available.
- Copies of full items can be used for personal research or study, educational, or not-for-profit purposes without prior permission or charge provided that the authors, title and full bibliographic details are credited, a hyperlink and/or URL is given for the original metadata page and the content is not changed in any way.
- Quotations or similar reproductions must be sufficiently acknowledged.

Please see our full end user licence at:
http://eprints.nottingham.ac.uk/end_user_agreement.pdf

A note on versions:

The version presented here may differ from the published version or from the version of record. If you wish to cite this item you are advised to consult the publisher’s version. Please see the repository url above for details on accessing the published version and note that access may require a subscription.

For more information, please contact eprints@nottingham.ac.uk

Functional Brain Imaging with fMRI and MEG

by

Jiabao He BSc

Thesis submitted to the University of Nottingham for the degree of Doctor of Philosophy, June 2005.

Acknowledgements

The author would like to thank Prof Peter Morris for selecting the author to carry out this work and for providing high quality supervisional guidance. Prof Morris has shown great patience and faith in the work, together with his kindness and encouragement. This has proven to be of enormous importance to the final outcome of this work. The author would also like to express gratitude to the Medical Research Council in Great Britain for providing financial support, and the Sir Peter Mansfield Magnetic Resonance Centre at the University of Nottingham and the Wellcome Trust MEG Laboratory at Aston University for facilitating this work.

Many scientists from different backgrounds have contributed to the research phase of this work. This includes: Dr Sue Francis, Dr Gareth Barnes, Dr Arjan Hillebrand, Prof Richard Bowtell, Dr Andy Gibson, Matt Brookes, Kay Head, Dr Paul Furlong, Dr Andy Peters, Dr Ian Holliday and Prof Peter Morris. The author is much indebted to these highly respectable scientists, who work diligently and selflessly to reveal the mystery of the human brain. The author is also immensely grateful to Dr Jonathan Fulford, Prof Peter Morris, Dr Sue Francis, Nikolas Anderson, Dr Andy Peters, Dr James Leggett, Dr Dan Green and Dr Ben Wilton for their advice on the presentation of this work.

The author would also like to thank and send best wishes to many friends met during the period of this work, although unfortunately there are too many to be listed here. Finally, the author would like to dedicate this achievement to his parents for their persistent and unreserved support at all times.

Abstract

The work described in this thesis was performed by the author, except where indicated. All the studies were accomplished on the 3 Tesla system within the Magnetic Resonance Centre at the University of Nottingham, and the Wellcome Trust MEG Laboratory at the Aston University during the period between October 1999 and June 2005. *Functional Magnetic Resonance Imaging* (fMRI) and *Magnetoencephalography* (MEG) are two promising brain function research modalities, sensitive to the hemodynamic and electrophysiological responses respectively during brain activites. The feasibility of joint employment of both modalities was examined in both spatial and temporal domains. A somatosensory tactile stimulus was adopted to induce simple functional reaction. It was shown that a reasonable spatial correspondence between fMRI and MEG can be established. Attempts were made on MEG recordings to extract suitable aspects for temporal features matching fMRI with a method reflecting the physical principles. It was shown that the this method is capable of exposing the nature of neural electric activities, although further development is required to perfect the strategy.

Contents

List of Figures

List of Tables

Chapter 1

Introduction

1.1 Aim of this Thesis

After years of evolution, the human body can respond to and adapt to nearly any kind of external environment, interactively and intelligently, with advanced functional division between tissues. The human brain contains more than 100 billion nerve cells, interconnected by miles of complex fiber tracks [32] and it is thus not difficult to appreciate that our understanding of the human brain remains severely limited. However, in the last decade of the 20th century, the availability of new brain functional imaging modalities has provided significant insight into the workings of the human brain.

Functional Magnetic Resonance Imaging (fMRI) and *Magnetoencephalography* (MEG) are amongst the most successful modalities presently available for exploring the function of the human brain. The aim of this thesis focuses on attempts to perform functional brain imaging at both high spatial and temporal resolution based on the combination of fMRI and MEG.

The first three chapters provide fundamental background information regarding the present position of functional brain imaging. The first chapter briefly describes the popular modalities available to functional brain research, their underlying physics principles and characteristics, together with the histories of fMRI and MEG and the future direction of development. The second chapter describes the fMRI technique in terms of both physics and physiology perspectives. A description of the source of the signal and contrast is given, followed by a discussion of conventional fMRI acquisition techniques and statistical analysis methods. The third chapter concentrates on MEG techniques. It examines fundamental brain electrophysiology phenomena, and the physical principles governing the observed magnetic field patterns induced by current dipoles are stated and explored. To enable the possibility of computing dipole sources, a set of physical head models are listed. In turn, the conventional dipole fitting analysis is summarized, and its advantage and limitations discussed.

Chapter four gives detailed descriptions of the instruments on which the current work was carried out. These include the specifications of the fMRI scanner, MEG scanner, anatomical MRI scanner, stimulator and other supporting equipment. The fifth chapter presents a comparison of the spatial location of activation indicated by fMRI and MEG in a simple somatosensory study. This focal response based study indicates the optimal way of combining information from these two modalities. The sixth chapter examines MEG from a signal decomposition aspect in an attempt to extract the fMRI compatible features from MEG. Both adaptive linear decomposition and time frequency analysis were applied to expose potential components and features of MEG. Both advantages and disadvantages of this methodology were addressed.

The final chapter summarizes the whole thesis and discusses possible future work.

1.2 Functional Imaging Modalities

Functional analysis of the human brain [59] was originally conducted by inferences from relating brain clinical symptoms and anatomical images acquired from structural imaging methods. However, the significant advance in human brain function research seen in the last 20 years may be credited to the development of a variety of new functional imaging modalities. These modalities have arisen from either the modification and refinement of existing imaging methods or the introduction of new approaches.

Positron Emission Tomography (PET) [69–71] was introduced in the early 1970's and represented one of the first technologies to allow complete localization of functional responses in the human brain. By injecting appropriate short-lived radio-labelled compounds, PET is capable of tracing biochemical or physiological processes involved in cerebral metabolism. Positrons generated during the decay of radioactive compounds, subsequently collide with negative electrons, releasing two photons, often referred to as γ-rays, in opposite directions. Accurate detection of these photons provides the location of the collision and in turn the position of the radioactive compound. Cerebral blood circulation can thus be monitored by determining the spatial concentration of these labelled compounds. However, as PET involves the use of radio-active agents, it is not suitalbe for regular and repetitive functional studies. Moreover, positron emitting radio-active materials usually have a relatively short decay time, increasing the expense of this technique, due to the need for on-site isotopic production equipment.

Single Photon Emission Computed Tomography (SPECT) [68] monitors brain functions through the detection of γ-rays generated by the decay of labelled radio-active pharmaceuticals injected into the body. Unlike PET, SPECT utilizes a collimator to determine the direction of γ-rays instead of coupling the detected photons, and subsequently the source position can be reconstructed by standard backprojection methods. SPECT generally costs less to operate, as the life time of the radio-active agents is relatively long. However, compared to PET, SPECT is of lower spatial resolution. As with PET, SPECT has limited applicability to repeat studies on healthy volunteers, due to the requirements of using a radio-active source.

Functional Magnetic Resonance Imaging (fMRI) [60, 66, 67], based on *Magnetic Resonance Imaging* (MRI) techniques, has become perhaps the most popular functional research modality in recent years. The acquired images are reconstructed through a simple *Fourier Transform* (FT) , through which a spatial resolution of a few millimeters can be reached. The most popular FMRI technique assesses brain function via *Blood Oxygen Level Dependent* (BOLD) contrast that measures changes in the local susceptibility due to changes in the concentration of deoxyhaemoglobin. The temporal resolution of fMRI is actually limited by the physiological latency and extended nature of BOLD contrast, rather than the technique itself. Perfusion and diffusion studies may be carried out in conjunction with fMRI to assess *cerebral blood flow* (CBF) and fibre morphology respectively. One of the main advantages of fMRI lies in the fact that image contrast occurs naturally without the necessity of introducing hazardous materials. Thus, repeat studies can be really carried out without ethical concerns.

Magnetic Resonance Spectroscopy (MRS) [54] is effectively *Nuclear Magnetic Resonance* (NMR) spectroscopy enhanced by spatial localization techniques. With slice selection gradients in three orthogonal directions, a NMR spectrum can be obtained from a single voxel. These spectra can be used to identify and measure certain key metabolism. For example, isotopic labelled compounds, such as ^{13}C -labelled glucose, may be introduced into the body to investigate biochemical pathways involved in brain energy metabolism nd neurotransmitter cycling. It is also possible to use protons as the probe nuclei after suitable water signal suppression has been carried out. MRS is highly chemically specific, but is compromised by poor sensitivity. Spatial resolution is therefore poor and signal averaging procedures are essential.

Electroencephalography (EEG) detects the brain electro-activity by measuring electrical potentials at the scalp. As a result, EEG is of extremely high temporal resolution, compared to those modalities mentioned above. However, electric fields often deflect significantly at boundaries, which causes intrinsic difficulty in source localization. The location of activation sites determined by EEG may be tens of centimetres from those found by fMRI. Potential field maps, instead of localized sources, are therefore often used to investigate brain function. Conventionally, epoch-averaged field maps and frequency spectrum analysis are the primary analysis methods. Although these methods are inadequate to interpret fully the underlying regional brain electro-physiology behavior, EEG remains the primary tool for psychological and psychiatric studies, due to its simplicity and non-invasive nature.

Magnetoencephalography (MEG) [40] monitors brain electro-activity via the measurements of magnetic fields outside of the brain. As with EEG, MEG is capable of reaching temporal resolutions of hundreds of microseconds. In addition, the spatial accuracy of MEG is far superior to EEG and is on the order of several millimetres. However, although it is feasible to localize magnetic sources,the relationship between source strength and the corresponding underlying regional brain electro-physiology behavior is not quantified and may not be achievable. As for EEG, MEG represents a passive modality, in which no biochemical agents are injected into body, and no stimulating signals are transmitted into the brain.

1.3 History of fMRI

The first observation of the *Nuclear Magnetic Resonance* (NMR) phenomenon in bulk matter was reported by Purcell *et* al [98] and Bloch *et* al [33] independently in 1946, which led to the winning of the 1952 Nobel Prize for physics. In 1950, Hahn *et* al [79] introduced the spin echo sequence based on pulsed *radiofrequency* (rf) excitation, enabling manipulation of spin systems to acquire further structural information. In addition, Ernst *et* al [77] introduced *Fourier Transform* (FT) analysis techniques into NMR spectroscopy, which significantly enhanced the efficiency of spectrum acquisition and earned him the Nobel Prize for Chemistry in 1991. This encouraged the development of more complicated sequences constructed for specific purposes, and hardware designs adapted for pulse sequences.

The first *Magnetic Resonance Imaging* (MRI) image, a two-dimensional image of a test tube object, was taken by Lauterbur *et* al [82] in 1973 through the application of magnetic field gradients and backprojection reconstruction. In the same year, Mansfield *et* al [81] produced an image using NMR diffraction and FT techniques. The importance of this early work together with their later contributions was recognized by the award of the Nobel Prize for Medicine to Mansfield and Lauterbur in 2003. Garroway *et* al [78] proposed the application of a magnetic field gradient in conjunction with a frequency selective rf pulse to enable the imaging of a single slice. A more efficient way of data acquisition and image reconstruction via reciprocal space and FT analysis was presented by Kumar *et* al [80] in 1975, followed by the first *in vivo* human image, a cross-sectional image of a finger, obtained by Mansfield *et* al [83] in 1976, and the first whole body image, acquired by Damadian *et* al [72] in 1977. Mansfield *et* al [84] in 1977 proposed the *Echo Planar Imaging* (EPI) sequence, a fast technique capable of imaging tissue movement and monitoring physiological change over time. In 1980, Edelstein *et* al [76] developed the spin-warp imaging sequence, now widely used on clinical MRI scanners.

Functional Magnetic Resonance Imaging (fMRI) detects *Blood Oxygen Level Dependent* (BOLD) contrast, and was first reported by Ogawa *et* al [96] in 1990. This modality is still in development, since the mechanism of BOLD contrast and the corresponding analysis approaches are still areas of intense research.

1.4 History of MEG

The first document referring to neuronal electrical effects can be traced back to an ancient Egyptian hieroglyph from 4,000 BC, in which pain and muscle contraction were shown to be caused by an electric sheatfish (catfish). The first carefully documented scientific experiment in neuromuscular physiology was conducted by Swammerdam *et* al [100], in which motor nerve stimulations were achieved from an *electromotive force* (emf) , generated at a bimetallic junction [50]. In 1747, Jallabert [85] carried out the first documented experiment on the therapeutic stimulation of muscles by electricity on a patient with a paralyzed hand. The first evidence of electricity being the medium of information transfer through nerves was an experiment in neuromuscular electric stimulation carried out by Galvani *et* al [86] in 1781, in which violent muscular contraction was observed on a frog following electrical stimulation of the femoral nerve. The first magnetic field stimulation of the nervous system was of a retina stimulated by a strong alternating magnetic field reported by d'Arsonval *et* al [73] in 1896, resulting in a flickering visual sensation.

The first measurement of bioelectric currents was performed by Matteucci *et* al [87,88] in 1838, in which the impulse in frog muscle was measured. Inspired by this work, du Bois-Reymond *et* al [89] measured the current arising from a frog nerve impulse. Adopting this recording technique, Caton *et* al [90] carried out measurements of brain electrical activity in rabbits and monkeys, and reported the presence of brain rhythms in 1875. Beck *et* al [91,92] succeed in demonstrating the non-attenuated propagation of electric impulse along a nerve fiber and reached similar conclusions to Caton.

The first non-invasive measurement of human brain electro-activity was reported by Berger *et* al [93] in 1924 with EEG, which resulted in two major rhythms, α and β, being identified. The demonstration of ultra low frequency brain electro-oscillations associated with petit mal absence seizures by Gibbs *et* al [94] consolidated the position of EEG in clinical applications. However, it was not until 1963 that the first attempt to record biomagnetic data was carried out by Baule *et* al [1], with a two million-turn induction coil on the human heart. The first MEG recording, also showing the α rhythm, was conducted by Cohen *et* al [51] within a magnetically shielded room. The birth of the *superconducting quantum interference device* (SQUID) revolutionized the world of biomagnetic field detection. Subsequently Cohen *et* al [57] introduced SQUID into MEG with the advance of spontaneous brain rhythm recordings without signal averaging.

1.5 fMRI and MEG together

FMRI has undoubtably been the most successful functional brain modality over the last 12 years, with studies on nearly all areas within the cortex. However, the mechanism of BOLD contrast and the quantitative relationship between actual brain activation strength and detected signal remain obstacles for the correct interpretation of acquired data. The usual spatial resolution of fMRI is a few millimetres, and is restricted by the *signal to noise ratio* (SNR) which is principally determined by the polarization of protons in a voxel. This resolution is usually adequate to discriminate nearby functional tissues to the desired level. Unfortunately the usual temporal accuracy is of the order of a second, although it is sufficiently high to monitor the haemodynamic response. The slow reaction of the haemodynamic response to external stimuli, rather than technical issues, restricts the observation of instantaneous brain responses. This limitation seriously impairs the ability of fMRI to investigate the temporal sequence of activation, and in turn, functional path or connectivity within the brain, since the BOLD signal timescale depends on factors other than the time of brain electro-activity.

The spatial accuracy of MEG is much better than EEG due to magnetic fields suffering less distortion when travelling through different materials than electrical fields. However, the intrinsic difficulty associated with the inverse problem in determining the location of the field sources from a limited number of field strength measurements and significant amounts of physical abstraction and approximation means that MEG is not ideal as the primary modality to localize brain functions. However, by detecting biomagnetic field changes, MEG is capable of reaching a temporal resolution adequate to follow evoked cerebral processes in real time. MEG has been widely used to investigate brain electro-physiological behavior, examining both cortical functional organization and inter-cortical coordination. Moreover, MEG can provide a better indication of the strength of actual brain activation, although it is true that MEG is blind to certain signal components and has non-uniform sensitivity over space to the sources.

Thus, it is easy to conclude that an effective combination of fMRI and MEG could add significantly to our understanding of the human brain. With the assistance of MEG, information pertaining to the underlying mechanism of BOLD contrast may be obtained allowing more robust analysis techniques in functional brain research. In addition, MEG may illustrate the temporal order of activation within the brain via the anatomical information provided by fMRI. FMRI results may also be used to provide likely field source locations for MEG analysis, making MEG data in which a large number of sources are present solvable. Although the combination of fMRI and MEG brings benefits to functional brain research, it is worth noting that a trade-off between these two modalities is inevitable and thus a careful combining of data is crucial to attain optimized results.

Chapter 2

NMR, MRI and fMRI theories

2.1 NMR Theory

2.1.1 Spin and Spin Magnetic Momentum

Spin is an intrinsic property of nuclei, whereby two orthogonal spin states

$$|+\rangle = \begin{pmatrix} 1 \\ 0 \end{pmatrix} \quad |-\rangle = \begin{pmatrix} 0 \\ 1 \end{pmatrix} \tag{2.1.1}$$

are defined as base vectors to compose any spin state of a spin-$\frac{1}{2}$ nucleus such that $|\phi\rangle = c_+|+\rangle + c_-|-\rangle$, where c_+ and c_- are complex coefficients. Based on the concept of spin, Pauli [97] proposed a set of spin angular momentum operators

$$\hat{S}_x = \frac{\hbar}{2}\begin{pmatrix} 0 & 1 \\ 1 & 0 \end{pmatrix}, \quad \hat{S}_y = \frac{\hbar}{2}\begin{pmatrix} 0 & -\imath \\ \imath & 0 \end{pmatrix}, \quad \hat{S}_z = \frac{\hbar}{2}\begin{pmatrix} 1 & 0 \\ 0 & -1 \end{pmatrix}, \tag{2.1.2}$$

along Cartesian axes, in which the two base spin vectors are the eigenvectors to $\hat{S}_z$ with eigenvalues of $+\frac{\hbar}{2}$ and $-\frac{\hbar}{2}$, such that $\hat{S}_z|+\rangle = +\frac{\hbar}{2}|+\rangle$ and $\hat{S}_z|-\rangle = -\frac{\hbar}{2}|-\rangle$. The spin magnetic moment, $\hat{\mu}$, is expressed as

$$\hat{\mu} = \gamma\hat{\mathbf{S}}, \tag{2.1.3}$$

where γ is the magnetogyric ratio, a property of the nuclear species. The *Hamiltonian* component, $\hat{H}_m$, arising from the interaction between the magnetic moment and an external magnetic field is

$$\hat{H}_m = -\hat{\mu} \cdot \mathbf{B} = -\gamma \hat{\mathbf{S}} \cdot \mathbf{B} \tag{2.1.4}$$

taking the form $\hat{H}_m = -\gamma B_0 \hat{S}_z = \omega_0 \hat{S}_z$ under a magnetic field $B_0\mathbf{k}$, where $\omega_0 = -\gamma B_0$ and is known as the *Larmor* frequency. The energy of pure spin states is given by

$$E_+ = \langle +|\hat{H}_m|+\rangle = \omega_0 \langle +|\hat{S}_z|+\rangle = +\tfrac{\hbar\omega_0}{2} \tag{2.1.5}$$

$$E_- = \langle -|\hat{H}_m|-\rangle = \omega_0 \langle -|\hat{S}_z|-\rangle = -\tfrac{\hbar\omega_0}{2} \quad , \tag{2.1.6}$$

indicating an energy splitting of $\Delta E = E_+ - E_- = \hbar\omega_0$, known as the *Zeeman Splitting* (Fig 2.1).

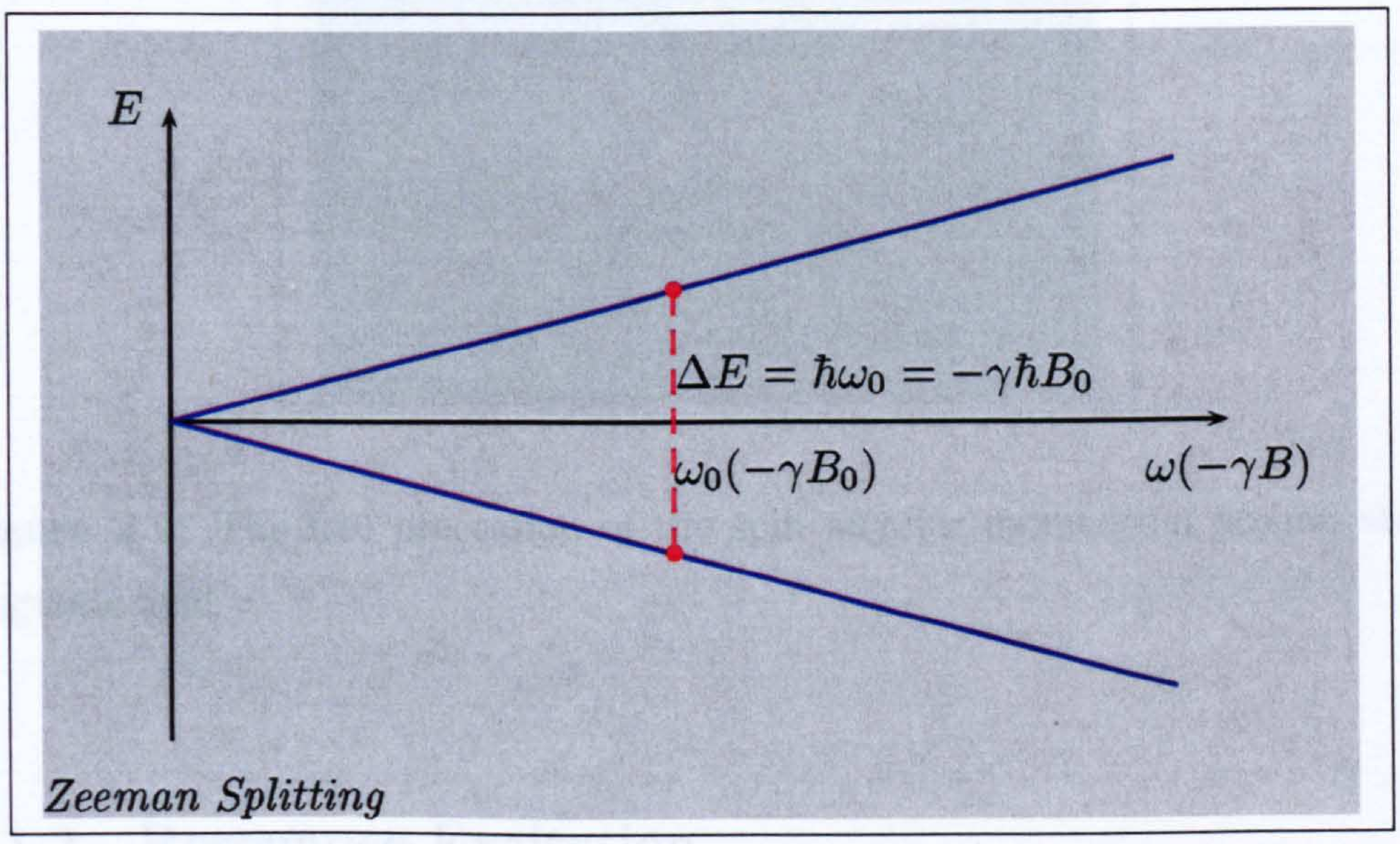

Figure 2.1: The energy level splitting due to the interaction between different spin states and the external magnetic field

The dynamics of a spin system are governed by the *time dependent Schrödinger equation* $\imath\hbar\frac{d}{dt}|\phi\rangle = \hat{H}|\phi\rangle$. Consequently a spin system in a static field with corresponding Larmor frequency ω_0 is given by

$$\begin{pmatrix} c_+(t) \\ c_-(t) \end{pmatrix} = \begin{pmatrix} c_+(0)e^{-\imath\frac{\omega_0}{2}t} \\ c_-(0)e^{+\imath\frac{\omega_0}{2}t} \end{pmatrix} = e^{-\imath\frac{\omega_0}{\hbar}\hat{S}_z t} \begin{pmatrix} c_+(0) \\ c_-(0) \end{pmatrix} . \tag{2.1.7}$$

It can be calculated that the spin angular momentum rotates at the Larmor frequency around the external magnetic field

$$\begin{aligned} S_x(t) + \imath S_y(t) &= (S_x(0) + \imath S_y(0))e^{+\imath\omega_0 t} && (2.1.8) \\ S_z(t) &= S_z(0), && (2.1.9) \end{aligned}$$

and is called the *free precession* movement (Fig 2.2).

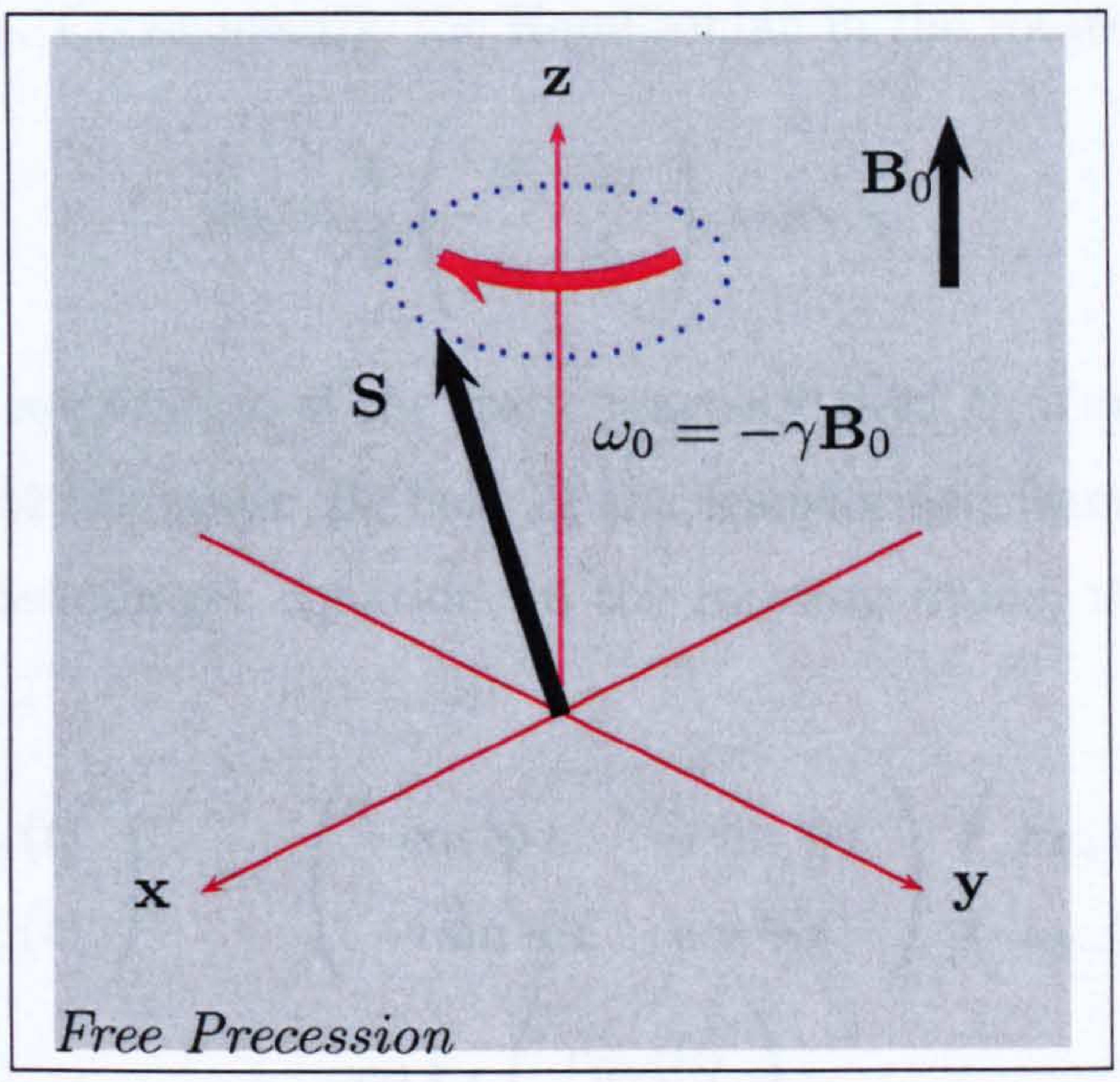

Figure 2.2: The free precession of the spin angular momentum around static magnetic field

2.1.2 Resonance Excitation

The rotating frame rotates at the Larmor frequency around the z-axis, and is described by the transformation $|\phi_R\rangle = \hat{R}_{\omega_0}|\phi\rangle$, where $|\phi\rangle$ and $|\phi_R\rangle$ are the spin states observed in the static frame and rotating frame respectively, and

$$\hat{R}_{\omega_0} = e^{+\imath\frac{\omega_0}{\hbar}\hat{S}_z t} = \begin{pmatrix} e^{+\imath\frac{\omega_0}{2}t} & 0 \\ 0 & e^{-\imath\frac{\omega_0}{2}t} \end{pmatrix}. \qquad (2.1.10)$$

The Schrödinger equation in the rotating frame can subsequently be derived as

$$\imath\hbar\frac{d}{dt}|\phi_R\rangle = \imath\hbar\left\{\frac{d\hat{R}_{\omega_0}}{dt}|\phi\rangle + \hat{R}_{\omega_0}\frac{d|\phi\rangle}{dt}\right\} = \hat{H}_R|\phi_R\rangle, \qquad (2.1.11)$$

where the Hamiltonian in the rotating frame is $\hat{H}_R = -\omega_0 \hat{S}_z + \hat{R}_{\omega_0} \hat{H} \hat{R}_{\omega_0}^{-1}$. In the static frame the application of an additional rotating magnetic field, *radiofrequency* (rf) field, $\mathbf{B}_1 (\cos\omega_0 t\mathbf{i} + \sin\omega_0 t\mathbf{j})$ in the $x - y$ plane, contributes to the Hamiltonian as

$$\hat{H} = \frac{\hbar}{2} \begin{pmatrix} \omega_0 & \omega_1 e^{-\imath\omega_0 t} \\ \omega_1 e^{\imath\omega_0 t} & -\omega_0 \end{pmatrix}, \tag{2.1.12}$$

where $\omega_1 = -\gamma B_1$. Consequently, the Hamiltonian in the rotating frame, $\hat{H}_R$, is

$$\hat{H}_R = \frac{\hbar}{2} \begin{pmatrix} 0 & \omega_1 \\ \omega_1 & 0 \end{pmatrix} = \omega_1 \hat{S}_x, \tag{2.1.13}$$

equivalent to the application of the static magnetic field B_1 along the x-axis and the cancellation of the static B_0 field in the transformed frame. Based on the time dependent Schödinger equation, in the rotating frame, the spin system is given by

$$\begin{pmatrix} c_{R+}(t) \\ c_{R-}(t) \end{pmatrix} = \begin{pmatrix} \cos\frac{\omega_1}{2}t & -\imath\sin\frac{\omega_1}{2}t \\ -\imath\sin\frac{\omega_1}{2}t & \cos\frac{\omega_1}{2}t \end{pmatrix} \begin{pmatrix} c_{R+}(0) \\ c_{R-}(0) \end{pmatrix} \tag{2.1.14}$$

$$= e^{-\imath\frac{\omega_1}{\hbar}\hat{S}_x t} \begin{pmatrix} c_{R+}(0) \\ c_{R-}(0) \end{pmatrix}, \tag{2.1.15}$$

illustrating that the spin system performs a free precession of angular frequency ω_1 around the x-axis in the rotating frame

$$S_{Rx}(t) = S_{Rx}(0) \tag{2.1.16}$$

$$S_{Ry}(t) + \imath S_{Rz}(t) = \{S_{Ry}(0) + \imath S_{Rz}(0)\} e^{\imath\omega_1 t}. \tag{2.1.17}$$

The dynamics of spin angular momentum in a static frame is therefore a combination of rotation in both the x and z axis (Fig 2.3).

By controlling the amplitude B_1 and duration t of the rotating field, the flip angle (Fig 2.4) representing the amount of rotation θ in the rotating frame can be calculated from $\theta = \omega_1 t$. Consequently an rf pulse can be effectively denoted by the direction and flip angle it induces.

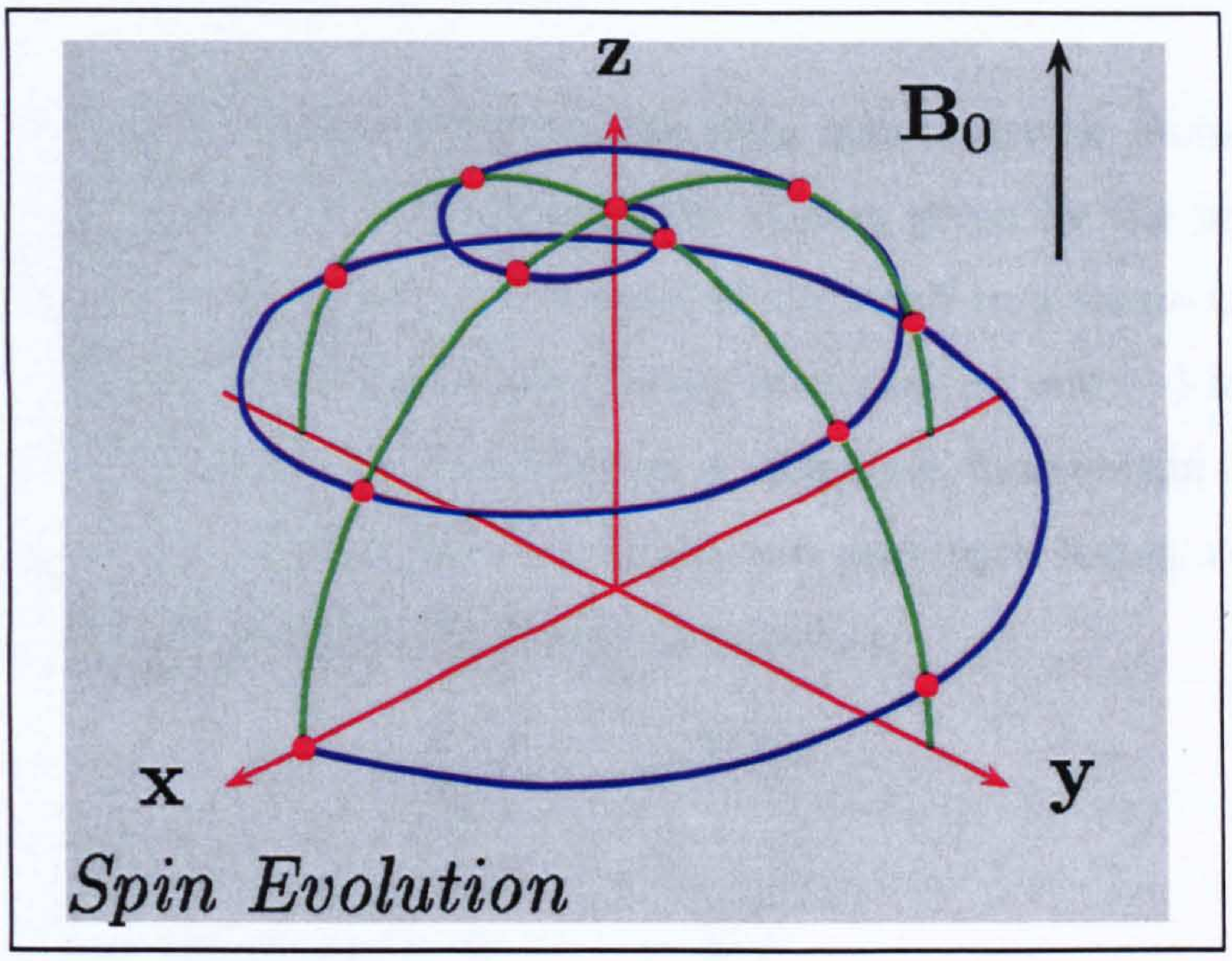

Figure 2.3: The evolution path of the spin angular momentum under a rotating magnetic field and a static magnetic field, with the amplitude of the rotating magnetic field exaggerated for illustrative purposes.

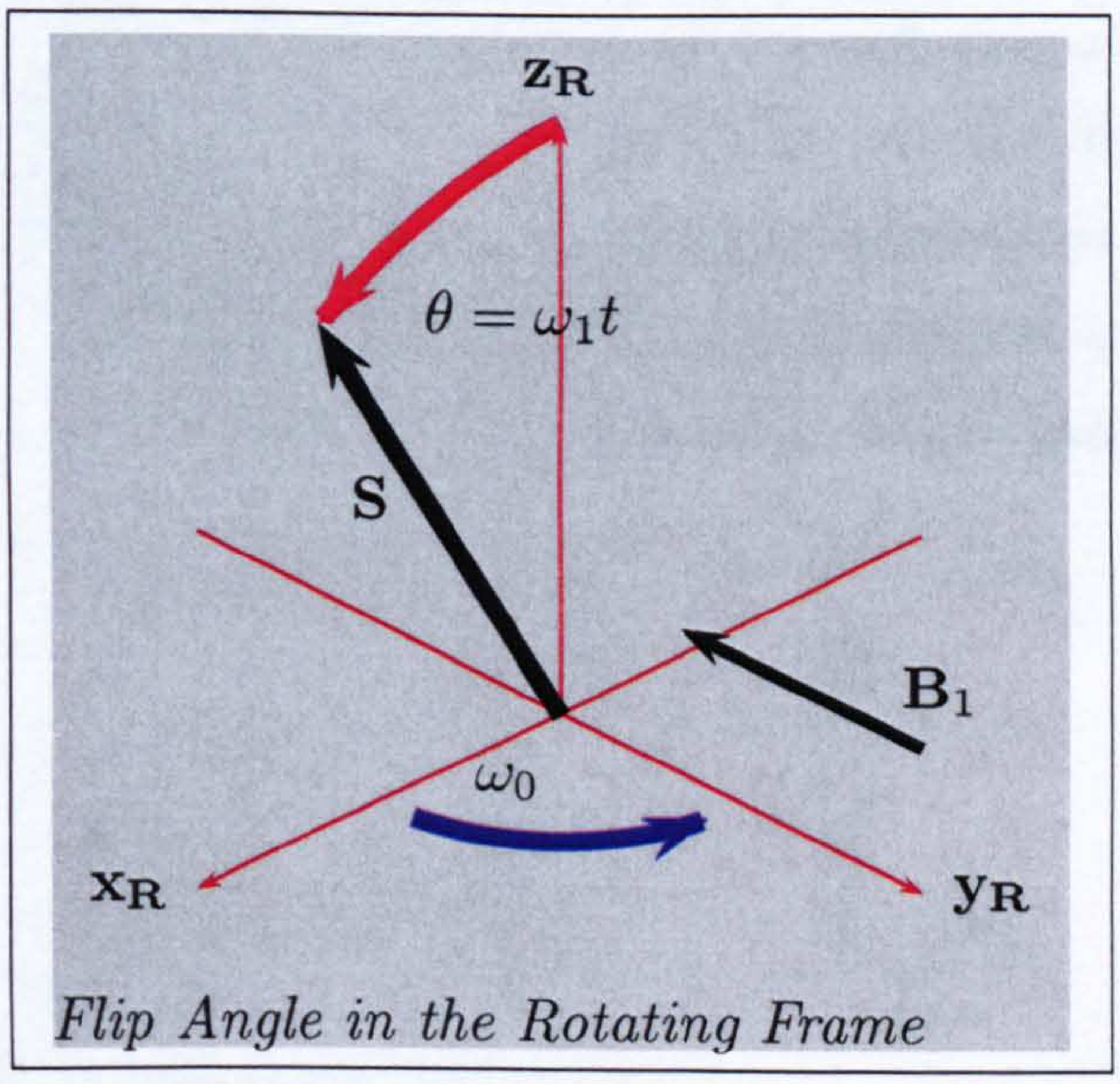

Figure 2.4: The flip angle determined by the application of excitation field, presented in rotating frame.

2.1.3 Bulk Magnetization

The bulk magnetization represents the total spin magnetic moment of a sample, depending upon the total energy of the system given by the temperature T and the magnetic enviroment. At thermal equilibrium in a static magnetic field $B_0\mathbf{k}$, the probabilities of a spin system being in states $|+\rangle$ and $|-\rangle$ are $p_+ = c_+c_+^*$ and $p_- = c_-c_-^*$ respectively, resulting in a magnetic momentum $\mathbf{M}_0$ given by $\mathbf{M}_0 = \frac{n\gamma\hbar}{2}(p_+ - p_-)$. The populations of the two pure spin states, $n_+ = np_+$ and $n_- = np_-$ follow the classical Boltzman distribution

$$\frac{n_+}{n_-} = e^{-\frac{E_+ - E_-}{kT}} \tag{2.1.18}$$

$$\frac{\Delta n}{n} \simeq \frac{E_+ - E_-}{2kT}, \tag{2.1.19}$$

where k is the Boltzman constant, $n = n_+ + n_-$ the total population and $\Delta n = n_+ - n_-$ the population difference between states. Consequently, the bulk magnetization is given by $\mathbf{M}_0 = \frac{1}{2}\hbar\gamma\Delta n\mathbf{k}$.

After disturbances to the spin populations, spin interactions restore the system's thermal equilibrium, at a rate given by T_1 and T_2. The longitudinal relaxation time T_1 governs the recovery of the bulk magnetization along the z-axis, while the transverse relaxation time T_2 governs the decay of the magnetization component in the $x-y$ plane. Although magnetization relaxation can be considered at a fundamental level, it is extremely complex to do so and the following model is a good approximation to reality. The dynamics of the system can be expressed as

$$\frac{d}{dt}M_x = -\frac{M_x}{T_2} \tag{2.1.20}$$

$$\frac{d}{dt}M_y = -\frac{M_y}{T_2} \tag{2.1.21}$$

$$\frac{d}{dt}M_z = -\frac{M_z - M_0}{T_1}. \tag{2.1.22}$$

in the rotating frame rotating at the Larmor frequency around the z-axis, where M_x, M_y and M_z are the magnetization components along x, y and z axes respectively. Consequently, the evolution of magnetization or *Free Induction De-*

cay (FID) , in the static frame is given by

$$\mathbf{M}_{x,y}(t) = \mathbf{M}_{x,y}(0)e^{\imath\omega_0 t}e^{-\frac{t}{T_2}} \tag{2.1.23}$$

$$M_z(t) = M_z(0)e^{-\frac{t}{T_1}} + M_0(1 - e^{-\frac{t}{T_1}}), \tag{2.1.24}$$

where $\mathbf{M}_{x,y} = M_x + \imath M_y$ is the primary signal in NMR.

When the signal (Fig 2.5) is $\mathbf{M}_{x,y}(0) = S_0 e^{\imath\delta}$, the Fourier transformed signal (Fig 2.6) can be written as

$$\mathbf{S}(\omega) = \frac{S_0 e^{\imath\delta} T_2}{1 + \imath\Delta\omega T_2}, \tag{2.1.25}$$

where $\Delta\omega = \omega - \omega_0$. The line width of the real part of the spectrum, or absorption spectrum, is $\frac{1}{\pi T_2}$ according to the *Full Width at Half Maximun* (FWHM) of a Lorentzian line.

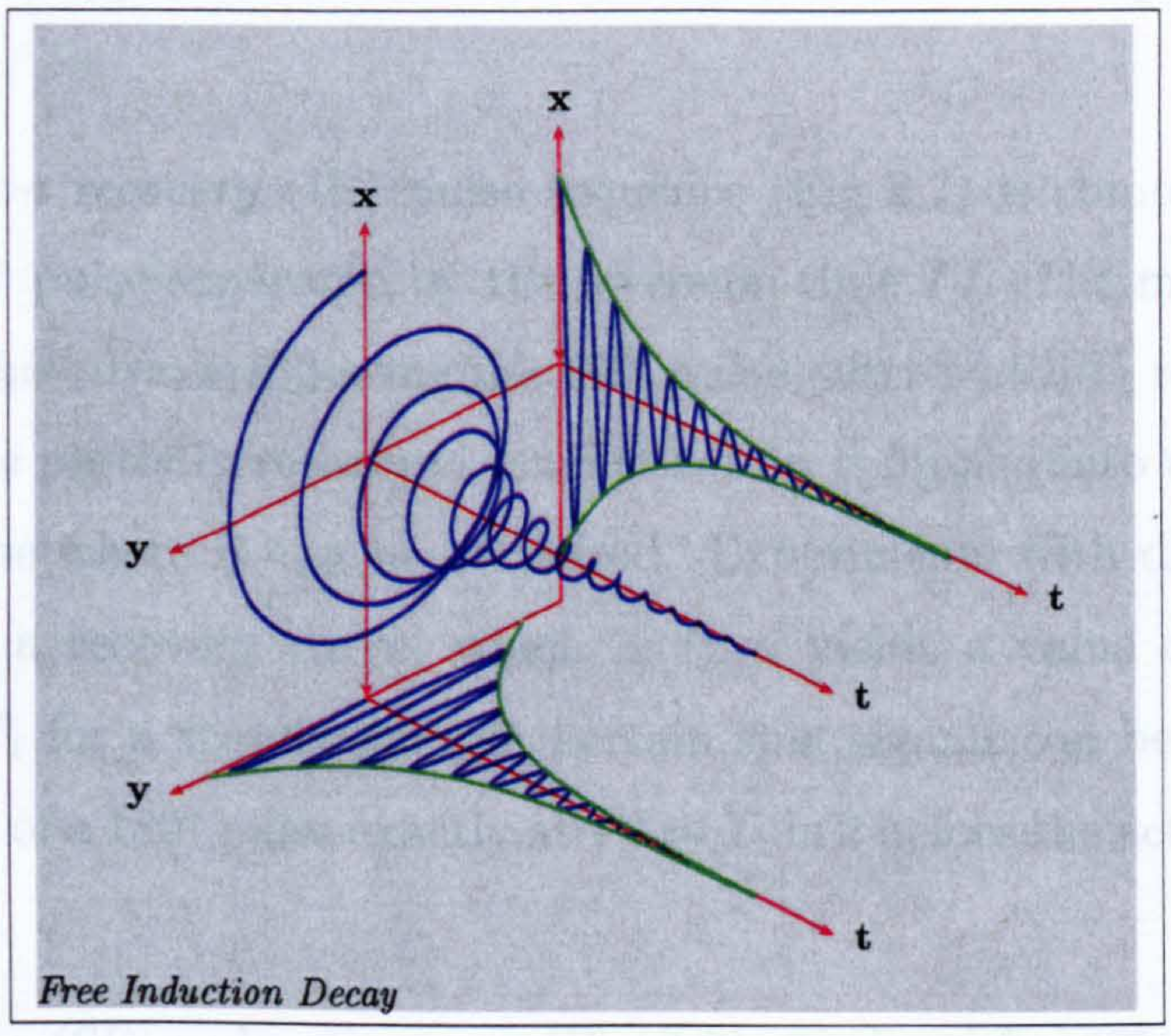

Figure 2.5: A typical Free Induction Decay (FID) in the time domain for $\delta = 0$

2.1.4 Spin Manipulation

The bulk magnetization can be oriented to any direction by the application of an appropriate rf pulse along a certain direction, while its magnitude can be controlled via magnetization relaxation with the appropriate timing of rf pulses.

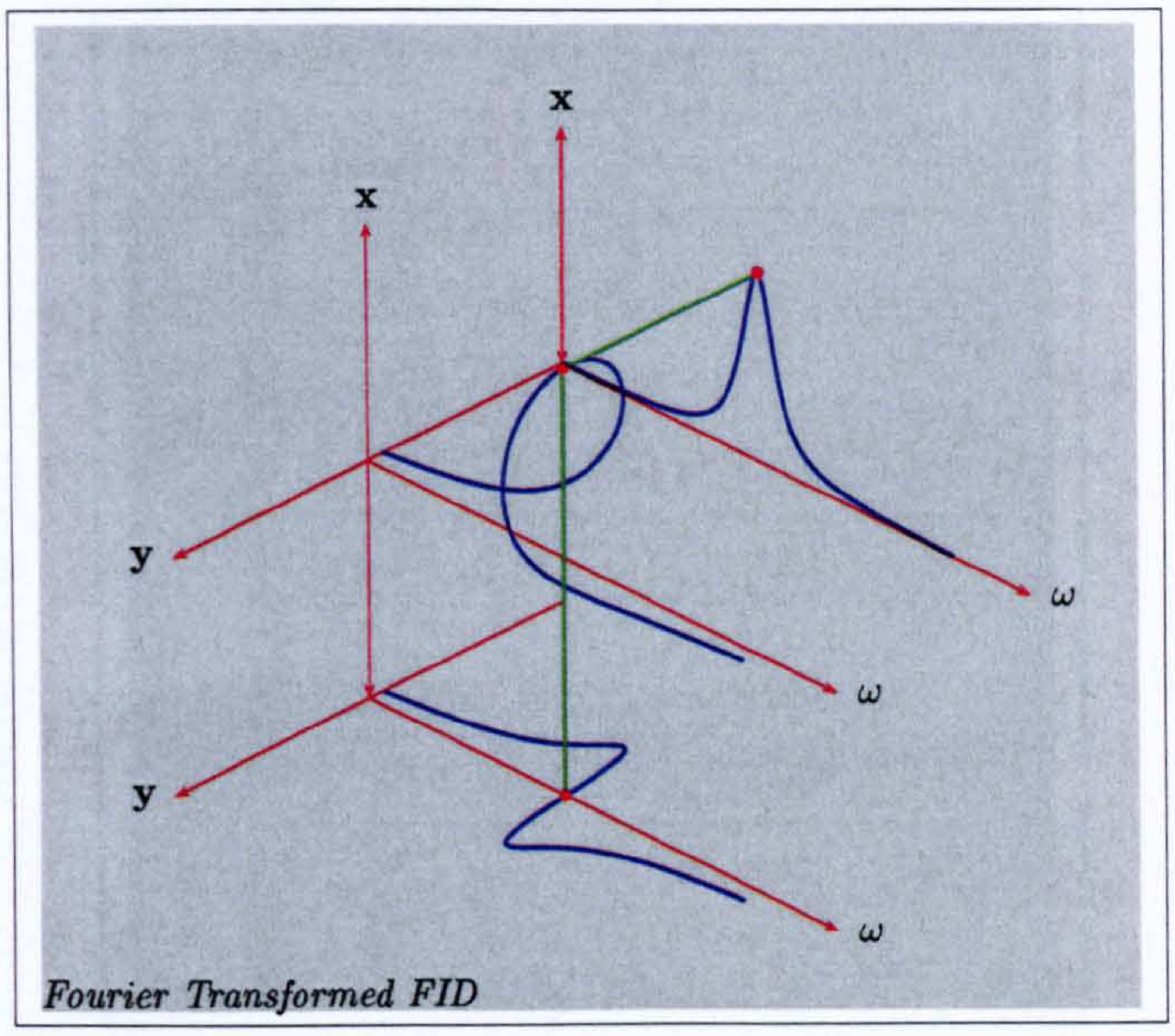

Figure 2.6: A typical Free Induction Decay (FID) in the frequency domain

An *inversion recovery* (IR) pulse sequence (Fig 2.7) is composed of a 180° pulse and a 90° pulse separated by the inversion time TI. The magnetization is aligned along the $-z$-axis following the 180° pulse, after which T_1 recovery begins. At time TI, the partially recovered magnetization is flipped into the $x-y$ plane by the 90° pulse where it can be measured. Experiments with different TI can be used to fit a recovery curve, which in turn yields a value of T_1. With a knowledge of T_1 for a specific sample, certain spin signals can be suppressed by the application of a 180° pulse exactly at $TI = T_1 \ln 2$ before the actual acquisition pulse sequence.

A *spin echo* (SE) pulse sequence (Fig 2.8) consists of a 90°_x pulse followed, after a time τ by a 180°_y pulse. The magnetization is aligned along the $-y$-axis by the 90°_x pulse, and subsequently undertakes free precession. In reality, the inhomogeneity of the static B_0 field is inevitable, causing spins at different locations to possess different Larmor frequencies. With a field difference ΔB_0 yielding a Larmor frequency shift $\Delta\omega_0 = -\gamma\Delta B_0$, the net phase shift after time τ is $\Delta\omega_0\tau$. This process, called dephasing, causes the extra decay of transverse magnetization, where individual spins contribute less to the bulk magnetization with time. After the 180°_y pulse, the spin magnetic momentum rotates 180°

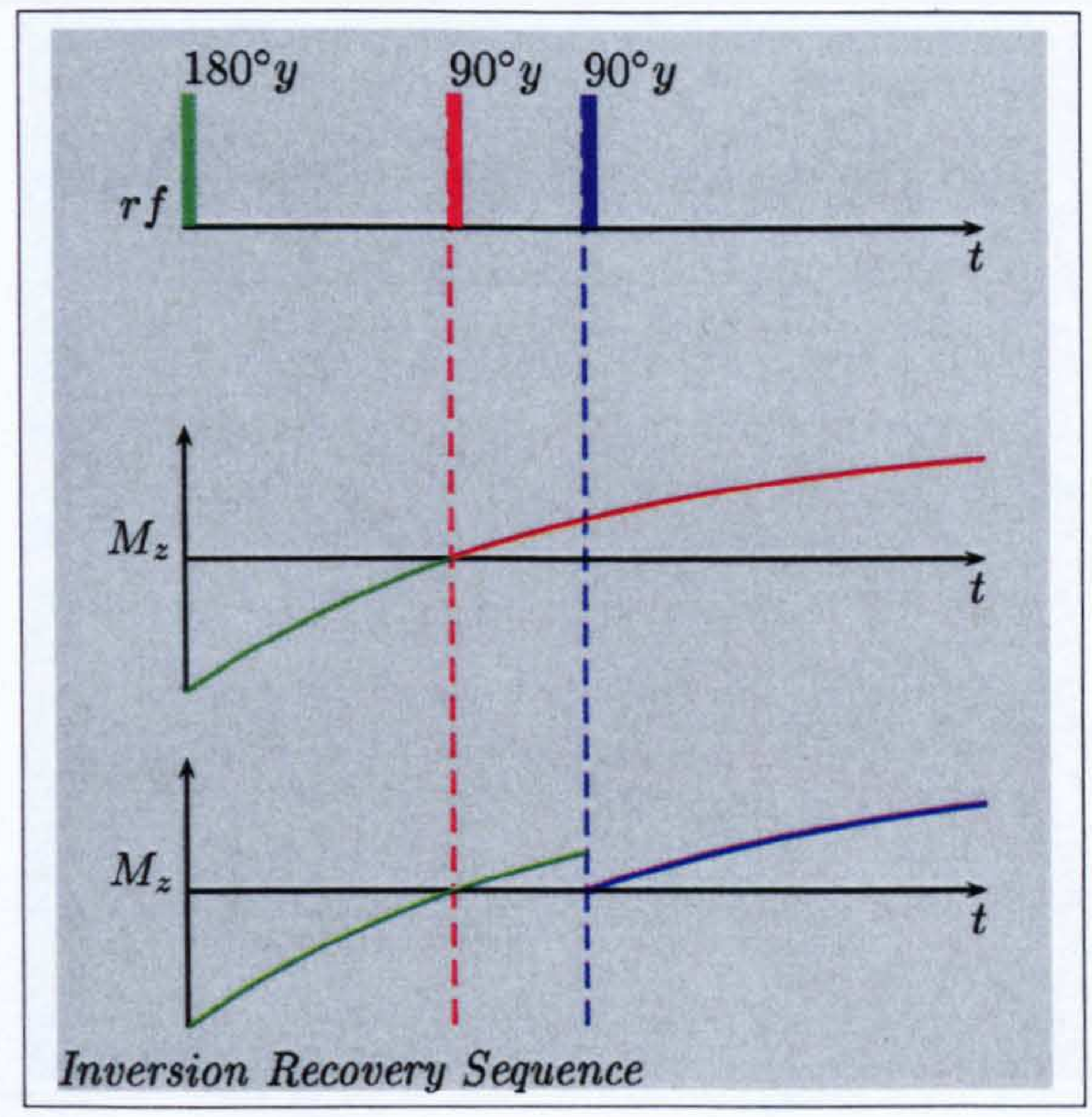

Figure 2.7: Inversion recovery sequences with (top) and without (bottom) signal suppression feature

around the y-axis, transforming the transverse magnetization into one with the same amplitude but a phase delay of $\Delta\omega_0\tau$. Due to the same field inhomogeneities that caused the initial dephasing after time τ, dephased spins come back into phase, producing a refocused magnetization at echo time $TE = 2\tau$. With different TE, pure T_2 relaxation can often be examined, yielding a value for T_2, as far as the approximation of transverse relaxation to a constant dependent exponential decay is still valid.

2.2 MRI Theory

2.2.1 Magnetic Field Gradient and Reciprocal Space

A single spin under an additional magnetic field δB oriented parallel to the external static field, exhibits precessional movement at an angular speed $\delta\omega = -\gamma\delta B$ in the rotating frame, resulting in a net phase shift $\delta\omega t$ after a time t. For a macro system under a linear field gradient $\mathbf{G} = \nabla B = \mathbf{c}$, for time t, the

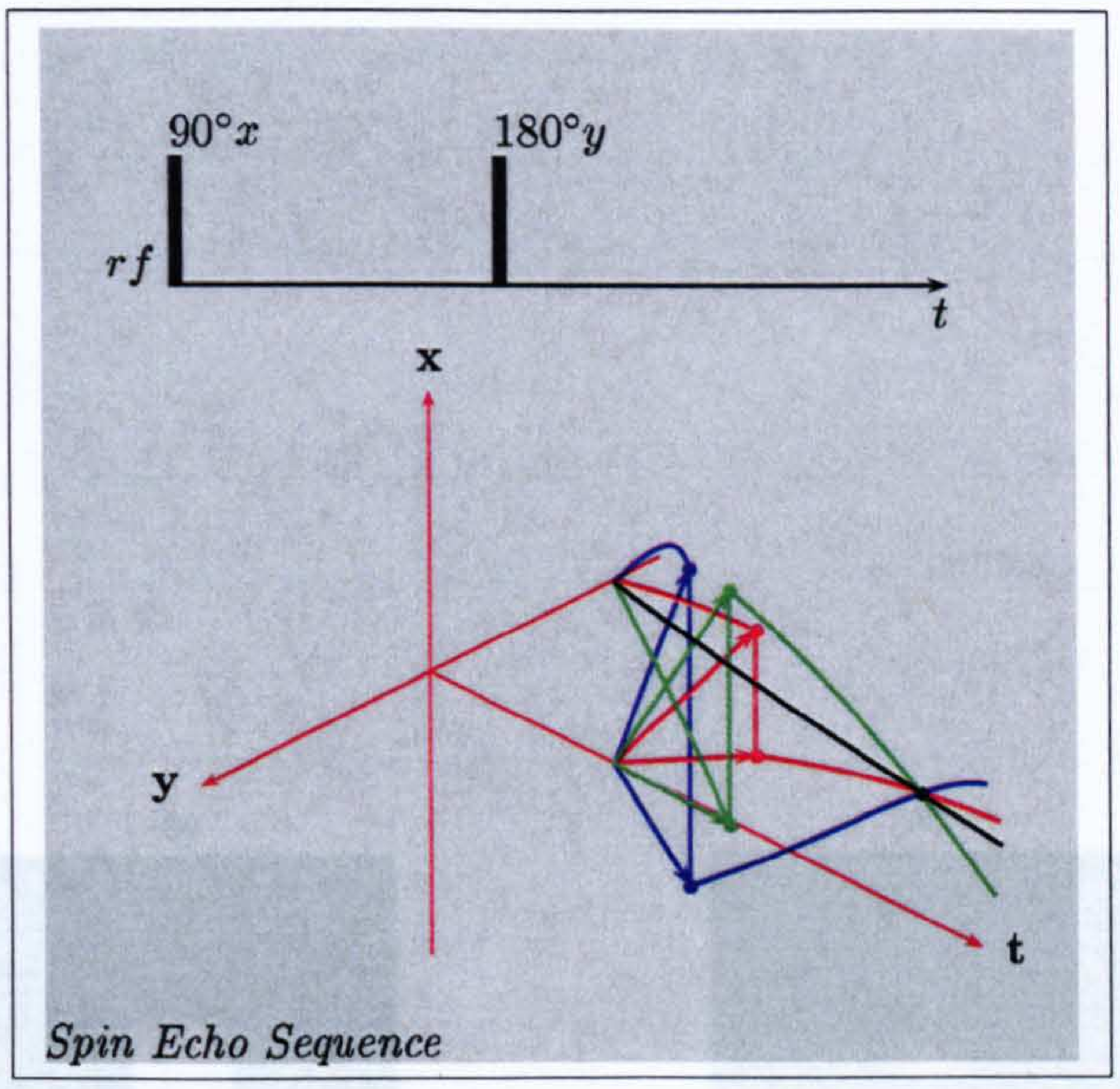

Figure 2.8: Spin echo sequence demonstrated by spins under different local field inhomogeneity

detected transverse magnetization, $\mathbf{M}_{x,y}$, is given by

$$\mathbf{M}_{x,y} = \int \rho(\mathbf{r}) e^{-\imath\gamma\mathbf{G}\cdot\mathbf{r}t} d\mathbf{r} \tag{2.2.1}$$

$$= \int \rho(\mathbf{r}) e^{-\imath\mathbf{k}\cdot\mathbf{r}} d\mathbf{r} \tag{2.2.2}$$

$$= \rho(\mathbf{k}) \tag{2.2.3}$$

where $\rho(\mathbf{r})$ and $\rho(\mathbf{k})$ are the spin density at location $\mathbf{r}$ in real space and $\mathbf{k}$ in imaging space (reciprocal space) respectively, while $\mathbf{k}$ is defined as $\gamma\mathbf{G}t$. The relationship between real and reciprocal space is given by the *Fourier Transform* (FT). Acquiring MRI spin density images can thus be considered as sampling the reciprocal space (Fig 2.9), accessible by varying $\mathbf{k}$.

The Fourier transform and inverse Fourier transform are defined as

$$\mathbf{H}(\omega) = \int_{-\infty}^{\infty} \mathbf{h}(t)\, e^{-\imath\omega t} dt \tag{2.2.4}$$

$$\mathbf{h}(t) = \frac{1}{2\pi} \int_{-\infty}^{\infty} \mathbf{H}(\omega)\, e^{\imath\omega t} d\omega, \tag{2.2.5}$$

where t, $\mathbf{h}(t)$ and ω, $\mathbf{H}(\omega)$ are the coordinate bases and the complex signals in real and reciprocal spaces respectively. $\mathbf{h}(t)$ and $\mathbf{H}(\omega)$ are called a FT pair

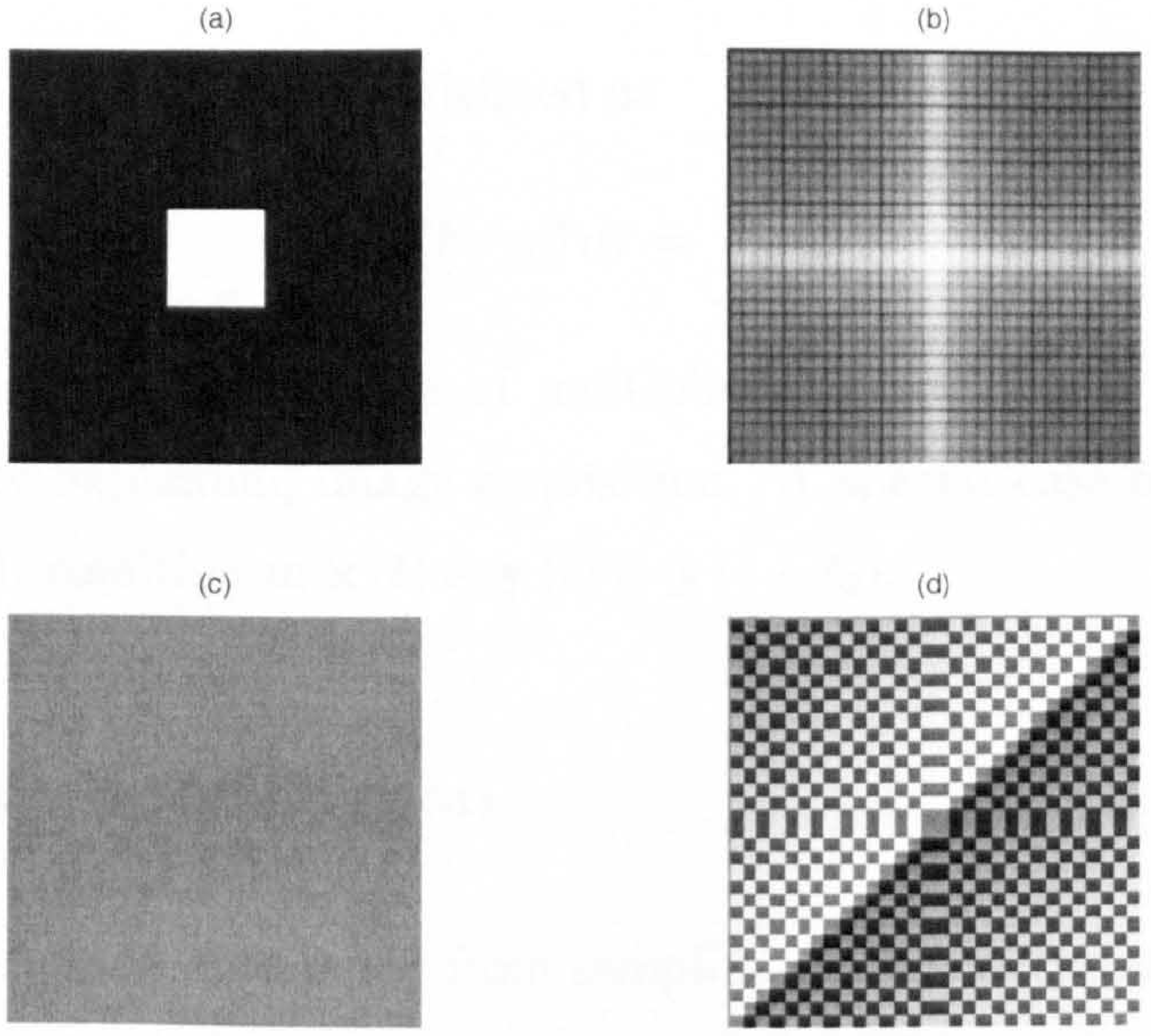

Figure 2.9: A simulation displayed in grey scale with black indicating minimal value and white the maximal value, showing the relationship between real and reciprocal spaces: (a) real magnitude image, (c) real phase image and (b) reciprocal magnitude image (in logarithmic scale), (d) reciprocal phase image.

$\mathbf{h}(t) \Leftrightarrow \mathbf{H}(\omega)$, with the symbol $\Leftrightarrow$ denoting the FT operation. FT conforms to the superposition principle, providing the definition of the FT summation operation that $\mathbf{x}(t)+\mathbf{y}(t) \Leftrightarrow \mathbf{X}(\omega)+\mathbf{Y}(\omega)$, where $\mathbf{x}(t) \Leftrightarrow \mathbf{X}(\omega)$ and $\mathbf{y}(t) \Leftrightarrow \mathbf{Y}(\omega)$.

Reciprocal space has a conceptual inverse relationship with real space, expressed by the fact that $\mathbf{h}(kt) \Leftrightarrow \left|\frac{1}{k}\right| \mathbf{H}\left(\frac{\omega}{k}\right)$, where $\mathbf{h}(t) \Leftrightarrow \mathbf{H}(\omega)$ and k is a non-zero constant. The FT decomposes a signal into oscillatory functions indicated by frequency and phase, while any shift in one space is transformed into the phase shift in the other space $\mathbf{h}(t-t_0) \Leftrightarrow \mathbf{H}(\omega)\, e^{-\jmath\omega t_0}$, where t_0 is a constant.

The convolution operation is defined as

$$\mathbf{x}(t) \otimes \mathbf{y}(t) = \int_{-\infty}^{\infty} \mathbf{x}(\tau)\, \mathbf{y}(t-\tau)\, d\tau = \int_{-\infty}^{\infty} \mathbf{x}(t-\tau)\, \mathbf{y}(\tau)\, d\tau, \tag{2.2.6}$$

which is the reciprocal operation of multiplication and has a crucial position in quantitatively explaining image acquisition. A special case of convolution is $\mathbf{x}(t) = \delta(t-t_0)$, resulting in $\mathbf{x}(t) \otimes \mathbf{y}(t) = \mathbf{y}(t-t_0)$.

2.2.2 Image Specification

MRI images are reconstructed from sampling reciprocal space via FT, so that the features of reciprocal sampling directly influence the acquired images.

The fact that only a portion of the reciprocal space can be sampled, weights the reciprocal space by a truncation function. A truncation function (Fig 2.10), or *boxcar* function, is defined as

$$\mathbf{h}(t) = \begin{array}{ll} A & |t| < T \qquad (2.2.7) \\ \frac{A}{2} & |t| = T, \qquad (2.2.8) \\ 0 & |t| > T \qquad (2.2.9) \end{array}$$

whose FT counterpart, a *sinc* function (Fig 2.10), is given by

$$\mathbf{H}(\omega) = 2AT\frac{\sin \omega T}{\omega T}. \tag{2.2.10}$$

The width of the *sinc* function $\left(\frac{2\pi}{T}\right)$ has an inverse relationship with the width of the *boxcar* function $(2T)$. Since a convolution is the reciprocal operation of multiplication, the acquired images are blurred by a *sinc* function with the width of $\frac{2\pi}{k}$, where k is the extent of sampled reciprocal space. The width of the *sinc* function can be viewed as an effective resolution, and becomes worse when smaller portions of reciprocal space are sampled. Although in most cases the physical image resolution is the same as the effective resolution, the expansion of sampled reciprocal space achieved by zero filling can enhance the physical image resolution but leaves the effective resolution unchanged. This filling procedure may be needed for computational reasons, since fast Fourier transforms can only operate on 2^n data points, where n is an integer.

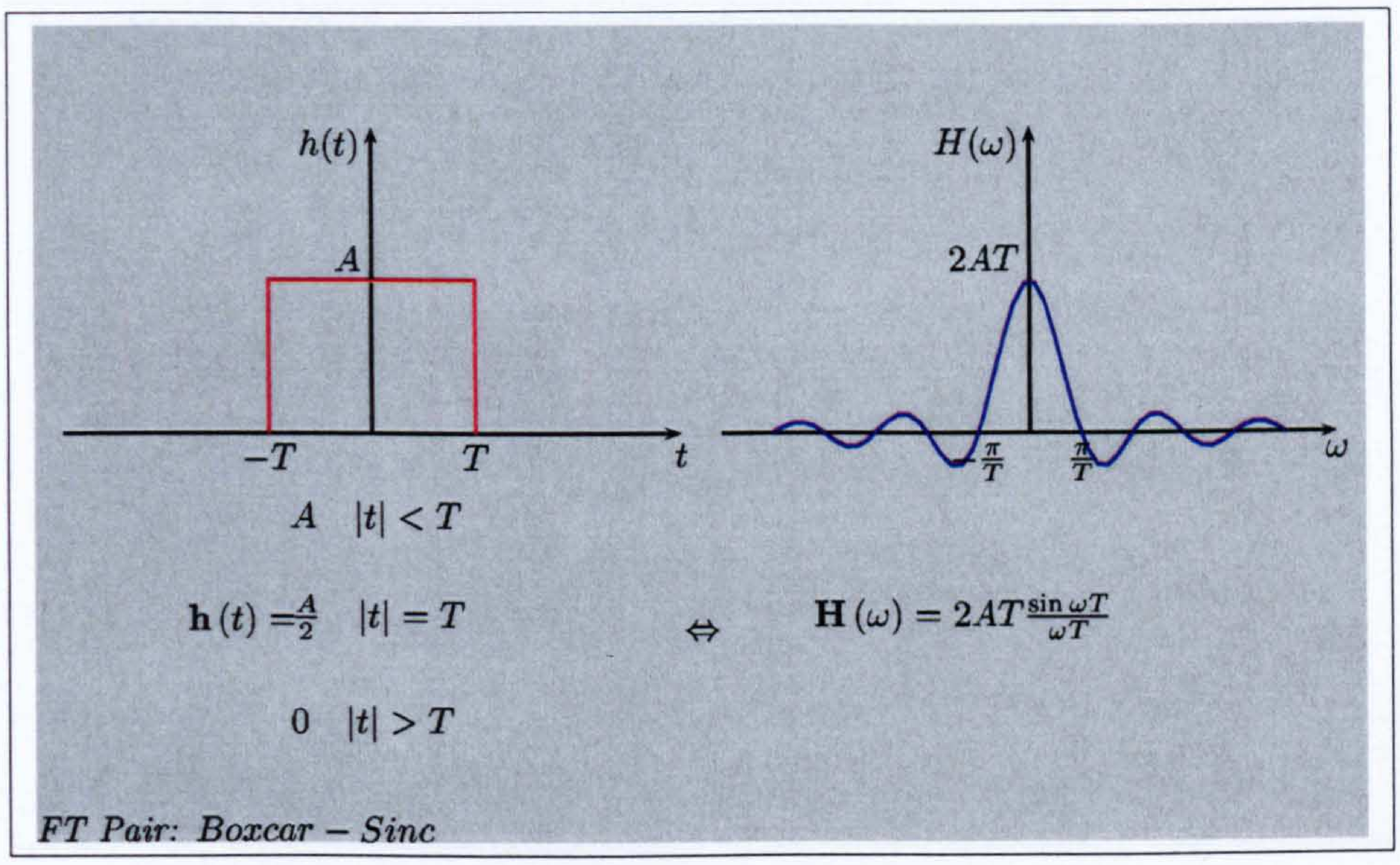

Figure 2.10: The truncation function and its FT counterpart.

Reciprocal space is sampled in a discrete fashion, equivalent to weighting by a δ function train. A δ function train (Fig 2.11) is composed of δ functions separated at regular intervals T

$$\mathbf{h}(t) = \sum_{n=-\infty}^{\infty} \delta(t - nT), \tag{2.2.11}$$

whose FT counterpart, another δ function train (Fig 2.11) with interval $\frac{2\pi}{T}$, is given by

$$\mathbf{H}(\omega) = \frac{1}{T} \sum_{n=-\infty}^{\infty} \delta\left(\omega - \frac{2\pi n}{T}\right). \tag{2.2.12}$$

The relationship between the interval size of these δ function trains again shows the inverse relationship present in FT. The multiplication of the reciprocal space with a δ function train with an interval of Δk is equivalent to the convolution between the actual object and another δ function train with an interval of $\frac{2\pi}{\Delta k}$. The *Field Of View* (FOV) is thus $\frac{2\pi}{\Delta k}$, representing the range in the real space that a non-repetitive image can be observed. Any area out of this range is basically a reproduction of some portion of the image. Since this convolution is the same as the reproduction of an object at an interval of $\frac{2\pi}{\Delta k}$, objects larger than the FOV can cause image wrapping due to nearby δ functions.

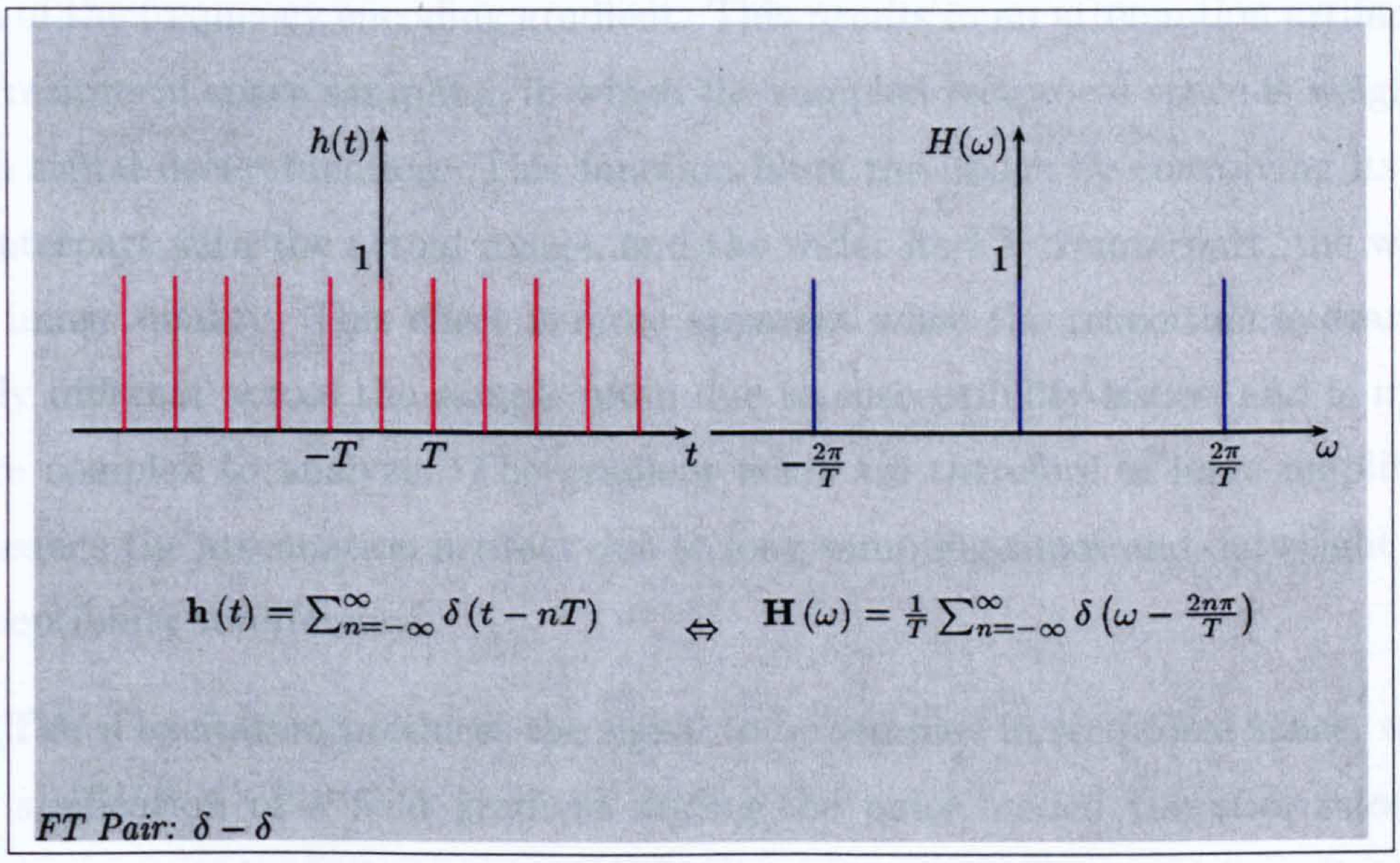

Figure 2.11: A FT pair involved in the explanation of signal sampling.

2.2.3 Reciprocal Space Sampling

The sampling of reciprocal space is achieved by manipulating the field gradients based on FT theory. The field gradient applied during the spin evolution period is called the *phase encoding* gradient, while the field gradient applied during the acquisition period is called the *frequency encoding* gradient. From the perspective of reciprocal space, the application of a gradient field moves the sampling point in reciprocal space accordingly, since the reciprocal space is defined by $\mathbf{k} = \gamma \mathbf{G} t$. From the perspective of spin dynamics, the field gradient changes the Larmor frequencies of spin procession and a phase distribution results after evolution time τ. This effect adds an extra factor $e^{-i\gamma \mathbf{G}\cdot\mathbf{r}\tau}$ onto the evolution of the spins. Here, the effect of the gradient depends on both the strength of the gradient and its duration. A line of reciprocal space is sampled during one application of the frequency encoding gradient, while only one point is sampled during the application of the phase encoding gradient. Consequently, the use of the phase encoding gradient significantly lengthens the duration of an experiment to an extent dependent upon the number of points required. However, transverse magnetization relaxation takes place during sampling via the application of the frequency encoding gradient. This results in an attenuation artifact in the reciprocal space sampling, in which the sampled reciprocal space is weighted by a signal decay function. This function blurs the image by convolving its FT counterpart with the actual image, and the wider its FT counterpart, the worse the image quality. This effect is more apparent when the relaxation is dramatically different across the sample often due to susceptibility issues, and is much more complex to analyze. The gradient fields are therefore of large amplitude to reduce the attenuation artifact due to long sampling times and outweight any susceptibility interference.

The rf excitation produces the signal to be sampled in reciprocal space, while the application of a field gradient during the pulse, called the *slice selection* gradient, can selectively excite spins in the sample. Under a field gradient $\mathbf{G}$, the distribution of Larmor frequencies exhibits a similar distribution across the sample $\omega(\mathbf{r}) = \omega_0 - \gamma\mathbf{G}\cdot\mathbf{r}$, showing that spins within the same plane orthogonal to the field gradient have the same Larmor frequency. An rf excitation pulse of frequency $\omega(\mathbf{r}) = \omega_0 - \gamma\mathbf{G}\cdot\mathbf{r}$ can excite only spins within that plane, while multiple planes can be excited by an rf excitation consisting of the corresponding frequency components. Subsequently a slice of the sample, thickness d, can be excited by an rf pulse of frequency bandwidth $\delta\omega = \gamma G d$. Normally, spins throughout the slice are expected to have the same flip angle in the same direction, implying the same amplitude and phase over the bandwidth, thereby forming a *boxcar* profile. The strength of the rf pulse against time is the FT of this *boxcar* function, which is a *sin* function oscillating at the central frequency of the bandwidth modulated by a *sinc* function with a width of $\frac{2\pi}{\gamma G d}$. The centre of the *sinc* function determines the centre of the reciprocal space, where all the excited spins are in phase. The applied slice selection gradient after the centre of reciprocal space produces an offset displacement in reciprocal sampling and causes spin dephasing. A negative gradient lobe is applied to cancel this displacement and dephasing. However, the selected slice suffers from signal loss, because of the imperfect bandwidth profile caused by the truncation of the *sinc* function. A high gradient strength reduces the width of the rf pulse and may put too much load onto the rf generator, while a low strength increases the width of the rf pulse and may cause signal loss due to relaxation effects. Optimized gradient strength can be attained from the targeted slice thickness based on the consideration of these problems. A broad band rf pulse excites all the spins in the sample, whose profile in time is extremely narrow causing large amounts of energy to be delivered in a short time.

2.2.4 Imaging Sequences and Contrasts

The *spin warp imaging* sequence (Fig 2.12) is a typical two dimensional imaging acquisition sequence widely used in many clinical configurations. A line in reciprocal space is sampled after the slice is selected, whose position is varied by the phase encoding gradient. A two dimensional image can be constructed by sampling all the points in the reciprocal space of the slice, while a three dimensional volume can be acquired slice by slice. A modified version upgrades this sequence to three dimensional, in which an extra phase encoding gradient is used rather than a slice selection gradient. In this pulse sequence, a single line in reciprocal space is taken during one rf excitation.

The *Echo Planar Imaging* (EPI) sequence (Fig 2.13) is particularly suitable for functional research, due to its short acquisition time. The reciprocal space of the selected slice is sampled line by line in opposite directions alternately. The speed of this technique is ensured by the sampling of a full reciprocal slice following a single rf excitation, although this puts a huge demand on the hardware capability.

The relationship between the intensity of each pixel in the image and an

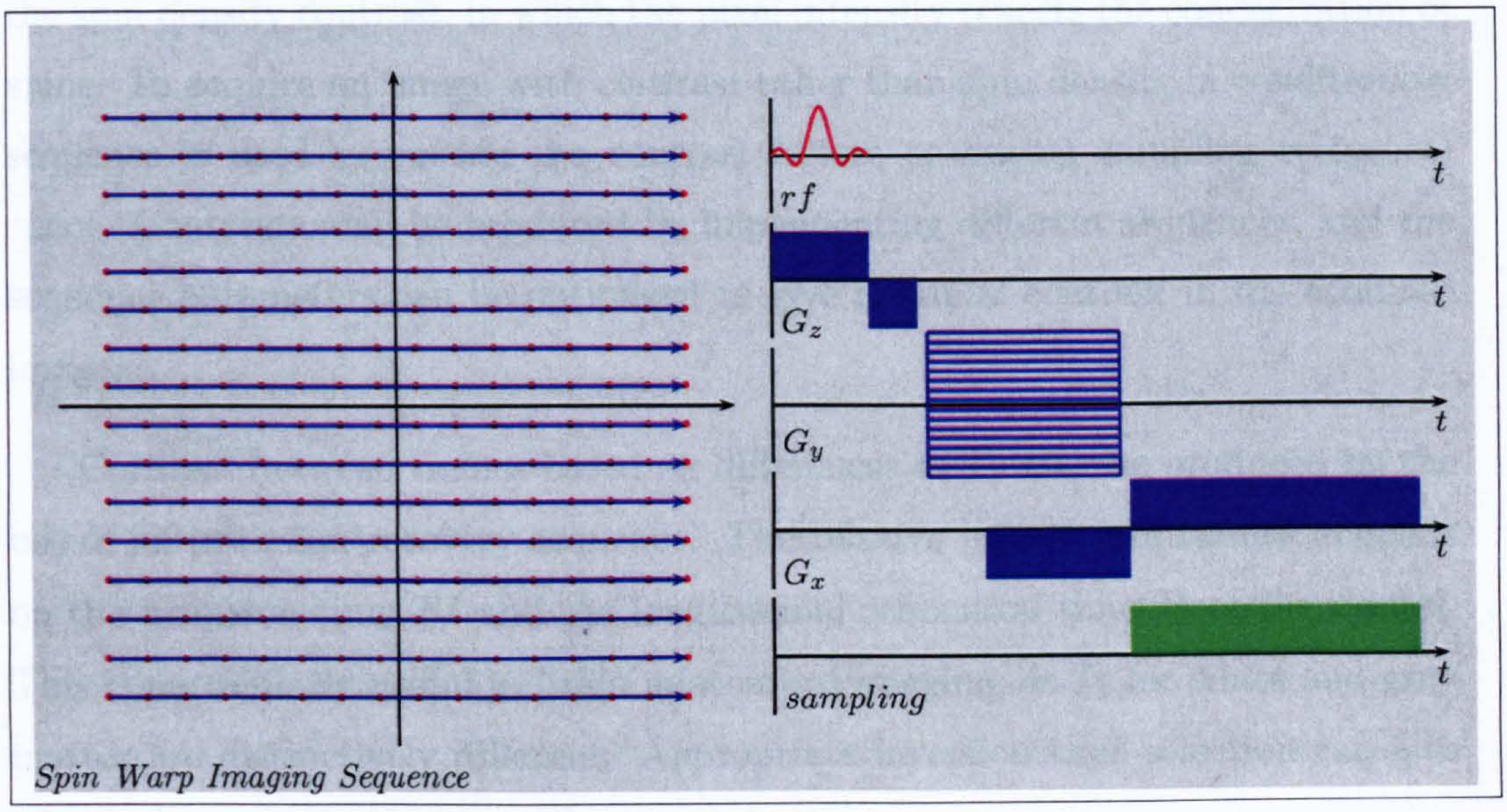

Figure 2.12: A typical spin warp sequence.

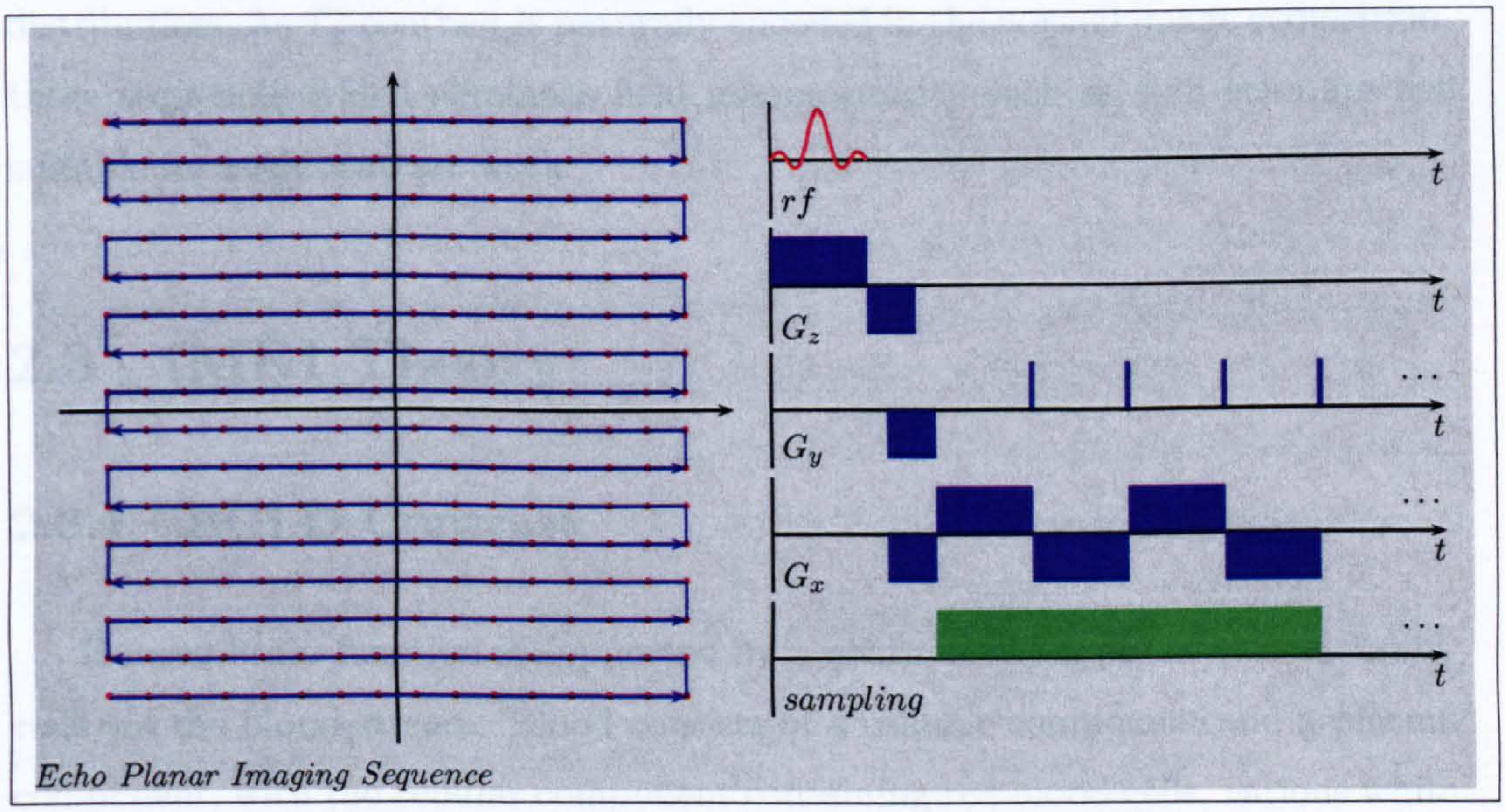

Figure 2.13: A typical echo planar imaging sequence.

underlying physical property is called image contrast. The intrinsic contrast is the spin density contrast, in which the pixel intensity reflects the concentration of spins. To acquire an image with contrast other than spin density, a conditioning sequence is used to encode the contrast before or during sampling reciprocal space. Contrasts may be produced by implementing different sequences, and the sequence parameters can be optimized to give maximal contrast in the acquired image.

Contrast between tissues based on differences in T_1 may be produced by the use of an inversion recovery sequence. The relative intensity of tissues depends on the inversion time TI and the longitudinal relaxation time T_1 of the tissues. This is particularly useful in brain anatomical imaging, as T_1 for white and gray matter are distinctively different. Appropriate inversion time selection can also effectively suppress the signal from certain tissues.

Contrast agents with large susceptibility values can be extremely useful for functional research, via the production of local field inhomogeneities. Such field inhomogeneities cause dephasing of the spins and subsequently the decay of the magnetization indicated by T_2^*. Thus the image intensities will reflect chemical distribution. As T_2^* contrast is naturally encoded in the normal image acquisition, those sequences which eliminate field inhomogeneity such as spin echo are not suitable for such contrast work.

2.3 fMRI Theory

2.3.1 BOLD Contrast

Human brain function is supported by a continuous supply of various materials via the blood stream. Blood consists of a cellular component and a plasma component, with the cellular component containing red blood cells, various white blood cells and platelets, whereas plasma contains a large number of dissolved substances. Red blood cells occupy, volume-wise, around 45 percent of the blood, and mainly contain haemoglobin which has the capability to combine with oxygen to give oxyhaemoglobin or to give deoxyhaemoglobin in the absence of oxygen.

The primary supply of blood to the brain is via two carotid and two vertebral arteries, with the internal carotid artery being the main source of *cerebral blood flow* (CBF). The arterial system smooths out the pulsatility of cardiac output via elastic walls, so that the blood flow is relatively steady at the capillaries. The smaller arteries and arterioles act as the resistance vessels of the system, whose cross-sectional diameter dynamically varies according to varying local demands. Capillaries are constructed with thin walls, have a large combined area and densely populate the brain tissue, allowing efficient exchange of substances with the tissue. The diameter of capillaries at $4\mu m$ is smaller than the $8\mu m$ size of red blood cells, indicating that a deformation of red blood cells takes place within the capillaries. Two systems of veins drain the brain, with veins on the surface of the brain draining the blood from the cerebral cortex and deep veins draining the blood from the basal area. Venules and small veins have distensible walls and act as a blood reservoir.

The major exchange process is via diffusion, which is the random spatial drift of molecules due to their kinetic motions. Diffusion represents simple Gaussian random movement governed by Stochastic calculus, with the net flux of molecules being proportional to the concentration gradient and the mobility of the molecule. The exchange of chemicals between functional cells and the capillaries is via the *blood brain barrier* formed by a virtually continuous layer of cells. This separates the blood from the brain parenchyma, effectively limiting the transport of protein and polar substances into the cerebral extravascular fluid, and reducing any corresponding movement of water. However, active transport facilitates the effective uptake of sugars, amino acids, and other specific metabolites.

Neuronal activity is associated with an increase in metabolic activity and blood flow. Since metabolic activity is directly linked with consumption of oxygen, increased neuronal activity results in an increased conversion of oxyhaemoglobin into deoxyhaemoglobin, leading to an increase in the local concentration of deoxyhaemoglobin in the tissue. Subsequently an increase in blood flow takes place, delivering a high concentration of oxyhaemoglobin to the functioning site. The increased blood flow leads to the over compensation of the increased production of deoxyhaemoglobin, and thus to an overall decrease in the concentration of deoxyhaemoglobin. The mechanism of increased blood flow coupling with increased neuronal activity is still unknown, although it has been proposed that vasodilator substance, or vasoconstrictor released by neurons during activity may be responsible for the blood flow regulatory mechanism. Despite this, there is little doubt of the close relationship between blood flow and neuronal activity. However, it is inappropriate to assume that blood flow regulatory mechanisms are geared entirely to satisfying tissue nutritional requirements.

Materials can be classified as being either paramagnetic or diamagnetic, according to their reaction in a magnetic field. Paramagnetic materials possess an intrinsic magnetic momentum without the presence of an external magnetic field. These magnetic momentums are normally distributed isotropically, but align together under the presence of an external field. Diamagnetic materials do not have an intrinsic magnetic momentum and react to an external field by generating an opposing field. The diamagnetic effect in paramagnetic materials is significantly smaller than the paramagnetic effect and can be ignored. Generally, the reaction of a material towards an external field is linear, $\mathbf{M} = \chi \mathbf{B}_0$, where $\mathbf{M}$ is the magnetic field induced by the external field $\mathbf{B}_0$, and χ is the magnetic susceptibility, being positive for paramagnetic materials and negative for diamagnetic materials.

In the human brain, oxyhaemoglobin is diamagnetic but deoxyhaemoglobin is paramagnetic, providing large susceptibility changes with small changes in concentration. Thus increased neuronal activity is coupled with a decrease in susceptibility in nearby capillaries due to the increased proportion of oxyhaemoglobin. This susceptibility change is due to the local oxygen level change and indirectly reflects the neuronal activity, leading to *Blood Oxygen Level Dependent* (BOLD) contrast.

2.3.2 fMRI Acquisition

The susceptibility change, resulting in the fluctuation in BOLD contrast, induces a change in the local field inhomogeneity in surrounding tissues. The large amount of water in the surrounding area provides the primary signal to indicate this fluctuation via the change in T_2^* decay.

A plain EPI sequence is suitable for the acquisition of fMRI images, due to its imaging speed and sensitivity to T_2^*. An EPI sequence samples the reciprocal space of a slice in one rf excitation, which can be achieved within a few tens of milliseconds and is sufficiently fast to provide a snapshot of haemodynamic change. This inevitably causes signal attenuation artefacts (Fig 2.14), compromising the image quality compared to anatomical sequences (Fig 2.15). The acquired image from a plain EPI sequence is T_2^* weighted, since no field inhomogeneity refocusing steps are taken. Consequently the static field inhomogeneity is also present in the acquired image. The *echo time* (TE), the interval between the rf excitation and the sampling of the centre of the reciprocal space, can be optimized based on the T_2^* of the tissue. The decayed signal $S(TE)$ at TE due to T_2^* relaxation is $S(TE) = S(0)e^{-\frac{TE}{T_2^*}}$, whose differentiation $\frac{dS(TE)}{dT_2^*}$ against T_2^* is maximized to give largest contrast with a change in T_2^*. By solving $\frac{d^2S(TE)}{dTEdT_2^*} = 0$, the optimized TE is T_2^*. However, T_2^* varies significantly in different cortical areas, which, together with static field inhomogeneity, gives an inevitable difficulty in TE optimization.

The haemodynamic process is monitored by repeatedly imaging a slice. The time between two consecutive acquisitions of the same slice is called the *repetition time* (TR), which dictates the temporal resolution of the attained haemodynamic response. Any residual transverse magnetization present during the rf excitation can corrupt the acquired image, so that the full decay of transverse magnetization imposes a lower limit of TR. Generally, $5T_2^*$ is regarded as the time for sufficient transverse magnetization decay under no application of crushing gradient, and most fMRI experiments are performed with TR larger than $1s$. However, different slices can be imaged sequentially with no exclusion due to transverse magnetization decay issues present. A volume is constructed from all the slices that are imaged repeatedly in a determined order. The interval between two consecutive volumes is basically TR, and the time between two consecutive acquisitions of different slices is called *time of repetition* (TOR).

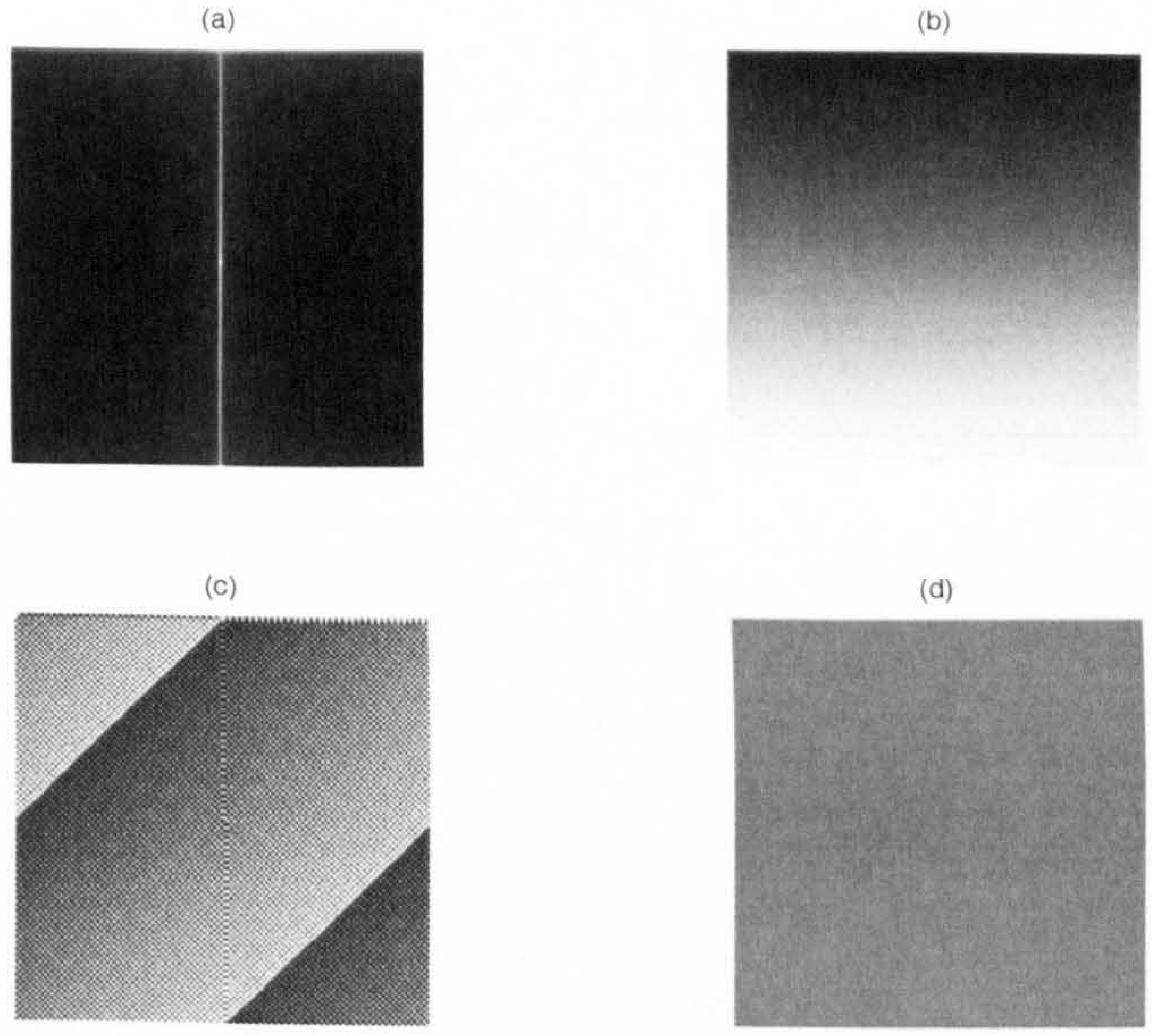

Figure 2.14: A simulation, displayed in gray scale with black representing the minimal value and white for the maximal value, showing the signal attenuation artefact of EPI sequence: (a) real magnitude convolution function (in logarithmic scale), (c) real phase convolution function and (b) reciprocal magnitude weight function, (d) reciprocal phase weight function.

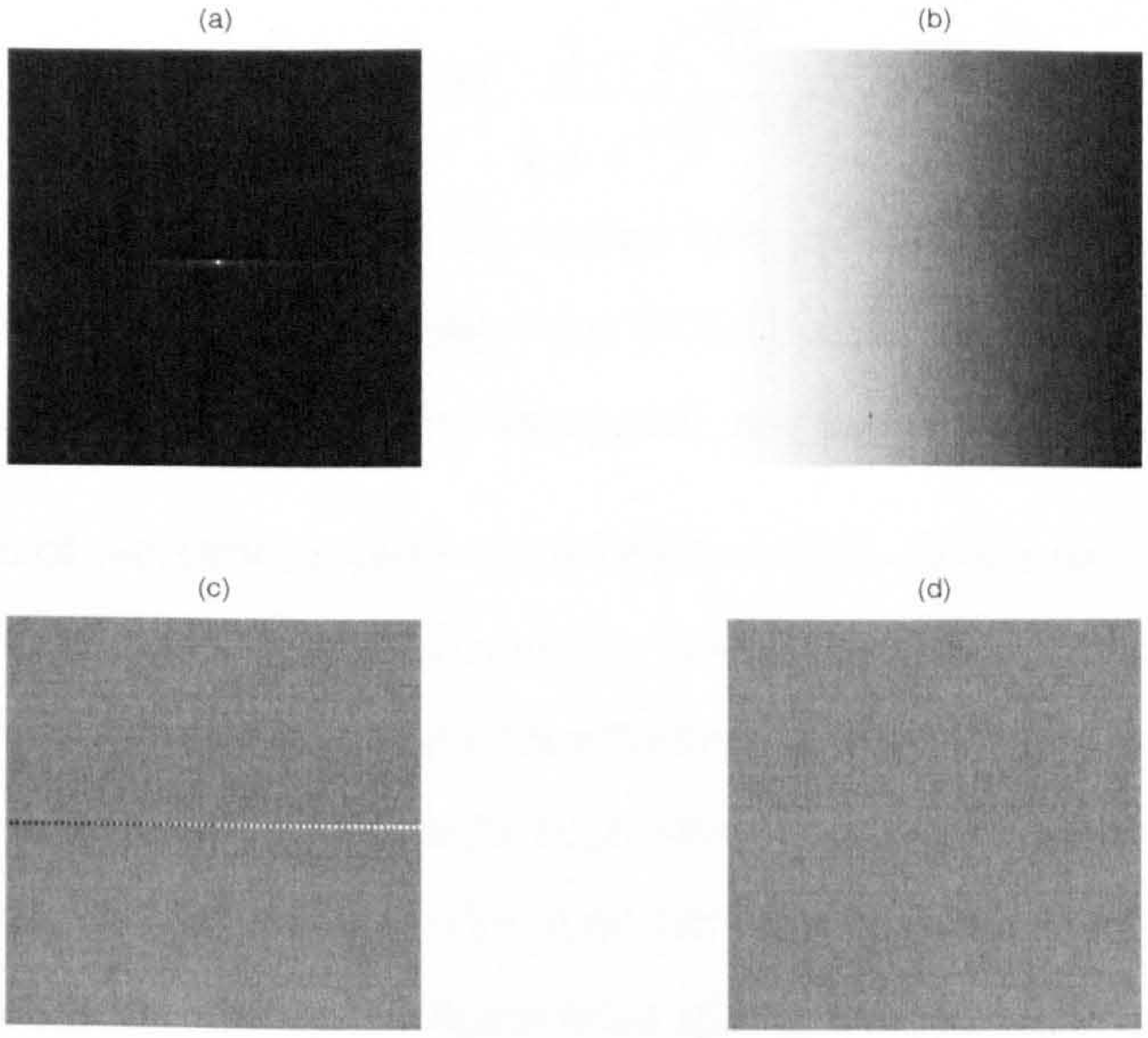

Figure 2.15: A simulation, displayed in gray scale with black representing the minimal value and white for the maximal value, showing the signal attenuation artefact of a spin warp sequence: (a) real magnitude convolution function (in logarithmic scale), (c) real phase image and (b) reciprocal magnitude weight function, (d) reciprocal phase weight function.

2.3.3 fMRI Study Optimization and Design

In general, the BOLD contrast induces less than 10 percent signal change in the acquired image, implying a careful parameter selection and experiment design is crucial to a successful fMRI study.

The TR of fMRI studies is well below $5T_1$, indicating that the full recovery of longitudinal magnetization does not take place. The steady state magnetization is given by

$$M = M_0 \frac{1 - e^{-\frac{TR}{T_1}}}{1 + e^{-\frac{TR}{T_1} - \frac{TR}{T_2^*}}}, \tag{2.3.1}$$

which represents the signal source for image acquisition. [43] A shorter TR provides less available signal, and impairs the BOLD contrast available. Therefore a balance between signal strength and temporal resolution has to be made.

The duration of reciprocal space sampling $t = n\tau$ is determined by the number of points, n, needed to be sampled and the sampling time, τ, for a single point. A large number of sampling points lengthens the acquisition and worsens the signal attenuation artefact. Although high sampling rate equipment can reduce the sampling time, the strength of the gradient increases proportionally with the sampling rate and may become impractical given the already high load on the gradients.

The signal from a pixel in the acquired image is proportional to the spin population in that voxel. A small voxel contains fewer spins, thus generates less absolute signal change with the same change of the BOLD contrast. The proportion of the signal change due to the BOLD contrast change relative to the noise signal is called the *Contrast to Noise Ratio* (CNR), indicating the ease of measuring any underlying physiological change. Large voxel size provides better CNR, however the spatial resolution is then compromised.

Although brain activities may be widely distributed around the brain, it is impractical to monitor the BOLD contrast throughout the brain in a single slice. Therefore, a large number of slices have to be used to cover the whole brain, which inevitably lengthens the TR, leading to a decreased temporal resolution of BOLD contrast. To minimize this effect, a *region of interest* (ROI) may be defined, and the slice selection gradient direction is selected to cover the ROI in the minimal amount of slices.

The level of the BOLD contrast signal is of the same order as the variation in signal due to noise, thereby implying that repeated tracking of BOLD contrast induced by the same brain activity followed by signal averaging is needed. A set of volumes in a complete single task is called a cycle, which exhibits the evolution of the BOLD contrast during the cycle length. The full evolution of the BOLD contrast can take as long as $30s$, and a cycle length may be much shorter. Since in most fMRI studies, cycles are sampled consecutively, the BOLD contrast may overlap with the one taken in the next cycle. While an extremely short cycle length saturates the BOLD contrast and reduces the CNR, a long cycle length results in a lengthy experiment.

The design of an fMRI study consists of an imaging specification configuration and a stimulus paradigm design. The imaging specification configuration determines the parameters for data acquisition such as TR, number of slices, slice orientation , voxel size, matrix size and so on. The stimulus paradigm design determines the way of presenting the stimulus or triggers for self initiated tasks, including number of cycles, cycle length and so on. Since TR is the temporal resolution of signal tracking, most timing parameters are expressed in units of TR. A design matrix (Fig 2.16) is often used to visualize the paradigm, in which the matrix members represent the intensity of the stimulus throughout the paradigm. The design of the study depends on its aim, so that the interesting features can be maximally exhibited by the result.

2.3.4 fMRI Noise and Data Correction

FMRI images are amplitude images constructed from the data points sampled in reciprocal space. Any inaccurate sampling of reciprocal space will therefore introduce distortion into the acquired images. A common artefact due to the characteristics of the EPI sequence is a displacement of sampling points in reciprocal space resulting in a pattern of alternate lines, due to mismatching of the positive and negative lobes in the frequency encoding direction. This kind

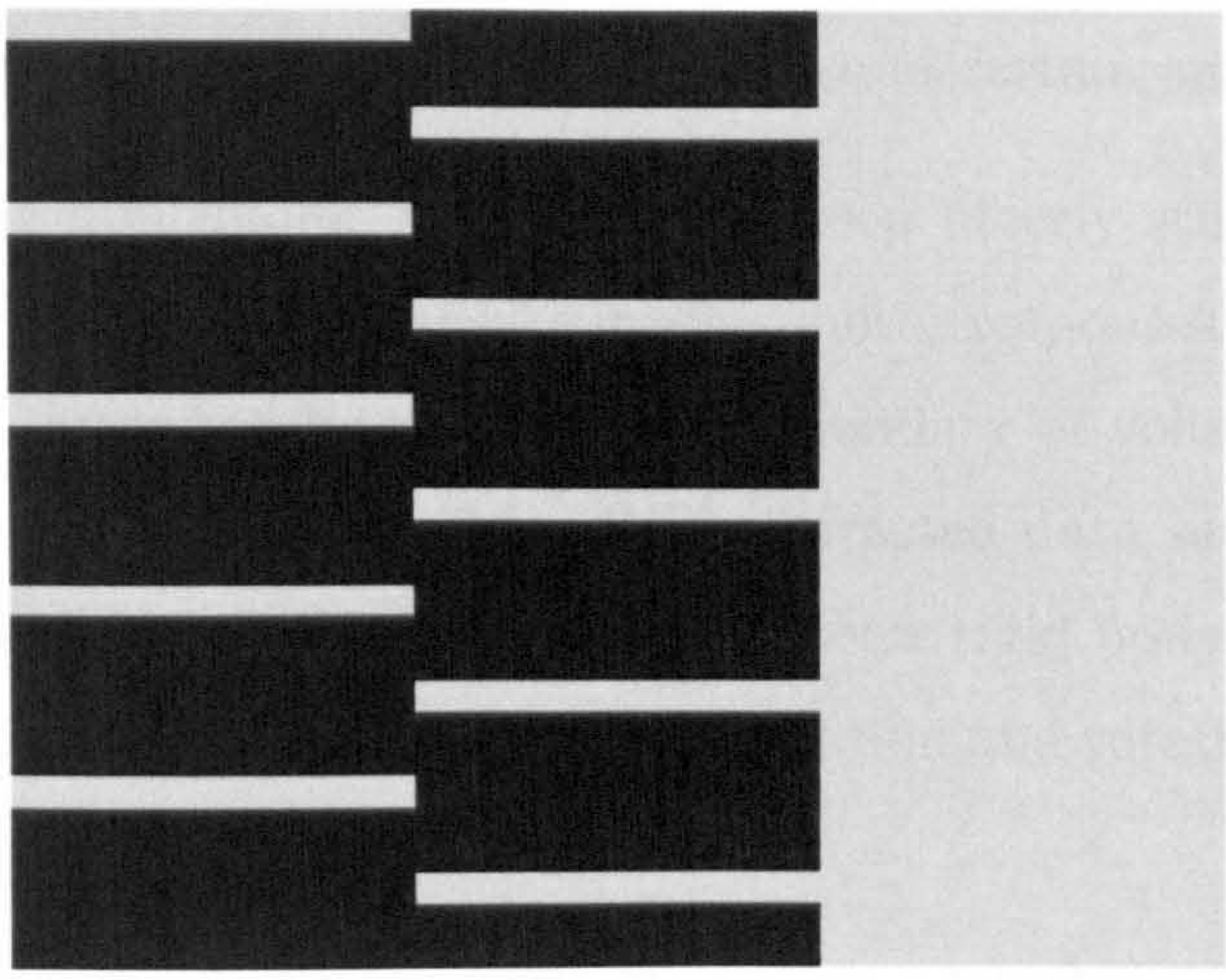

Figure 2.16: A design matrix with three columns, where the first two columns represents two conditions appearing in sequence for five cycles and the last column as a baseline with no relation to the conditions.

of displacement introduces ghost images of the real object at a displacement at half of the FOV along the phase encoding direction. Although the position of the ghost is fixed, the intensity of the ghost and object image depends on the actual position of the reciprocal space sampling. The existence of ghosts affects the intensity of the observed object, so that valid results cannot be attained by merely removing the ghost. However, ghost images can be corrected to a certain degree by introducing a phase shift between alternate sampling lines. The images constructed from this correction may exhibit high intensity at the centre of the image due to a DC offset in the signal carrier's circuit. This can be easily corrected by assigning the central pixel the intensity of the average intensity of surrounding pixels.

Since at the initial phase of a study the steady state magnetization is not achieved in a few acquisition volumes, the first few volumes of the collected data set cannot represent the normal brain response towards presented stimulus or performed tasks. In this case, the first few volumes have to be extracted from the data set to prevent them from contaminating the data analysis. Graphical wise segmentation of the image is often carried out to allow efficient processing and reduce the interference from background noise in certain analysis steps.

It is reasonably difficult for the subject to keep utterly still throughout an fMRI experiment, especially if the tasks involve motor responses. Small and slow movements can be corrected by matching the boundary of volumes to that of a reference volume randomly selected from the extracted data set. A fitting procedure is performed typically based on a 6 parameter rigid body transformation, where the transformation depends on both translation and rotation operations in 3 orthogonal directions.

The total blood supply to the brain fluctuates with time during an experiment, causing the spin density to fluctuate accordingly. Since the BOLD contrast image is simply a T_2^* weighted spin density image, the effect of local susceptibility change due to neuronal activity cannot be properly examined due to the fluctuation in spin density. The BOLD contrast can be correctly investigated by eliminating the effect of the change in blood supply from the acquired image pixel intensity, where an intensity normalization scales the total intensity of the whole volume to a fixed value. This operation is often carried out with the application of an image mask to eliminate the influence of background noise.

Since fMRI images are taken slice by slice consecutively, the timing of each slice in the same volume is slightly different. A timing error can occur when a time sensitive analysis is carried out. This timing mismatch can be corrected by interpolating the time course of a pixel to derive the volumes at a specified time.

Random noise is distributed spatially in the acquired image, and usually shows no correlation between nearby pixels. Spatial smoothing can thus be carried out to reduce the noise, although spatial resolution of the image and independency of pixels are compromised. Because of this drawback, many studies emphasizing spatial resolution do not carry out spatial smoothing. Different algorithms of spatial smoothing are available. A Gaussian kernel is the most popular choice, which is expressed as $G = e^{-\frac{x^2}{2\sigma^2}}$, where the shape is governed by *Full Width at Half Maximun* (FWHM) $\delta x = 2.35\sigma$.

Random noise also presents temporally in the acquired data set at either low frequency as system drift or high frequency as thermal noise. Consequently a bandpass filter is often adopted to reduce such noise. Although many types of filters are available, Gaussian kernel smoothing is the most widely used filtering method. A Gaussian kernel smoothing method convolves the Gaussian kernel indicated by the FWHM with the pixel time course, which can be performed either by numerical convolution or inverse FT and multiplication of their Fourier conjugates. While smoothing the time course, the degree of independency of different points in the pixel time course and the effective temporal resolution are reduced. Consequently a study specifically designed for high temporal resolution monitoring of the BOLD contrast may not utilize temporal filtering.

Other sources of noise, such as the field homogeneity change due to breathing, cannot be simply corrected by computational methods. The impact of these artifacts on the attained results is being investigated, and is viewed insignificant in present fMRI experiments.

2.3.5 fMRI Data Statistical Analysis

Since the signal changes that arise from BOLD contrast are of the same order as those due to noise, a statistical analysis approach is necessary to discriminate between the signal change due to the BOLD contrast and that due to the noise. Most statistical analysis methods are parametric tests, assuming that the pixel intensity is Gaussian distributed or purely randomly distributed. A statistical analysis can be either response model free or response model based, depending on the aim of the analysis. A response model free analysis makes no assumption about the acquired result, while a model based analysis assumes the expected result and tests the matching between the collected data and the assumption. Response model free analysis is often used to explore the data, since any suitable pattern of intensity change is retained. Response model based analysis is used to derive the detailed analysis of specific aspects of the BOLD response, since secondary responses can be excluded by assuming the expected response.

Analysis of variance (ANOVA) does not assume the shape of response. Inter and intra cycle variances are compared to give an indication of the response strength of each pixel to the stimulus or the task. A pixel with strong response will exhibit large intra cycle variance due to the dramatic intensity change between the active and rest periods, while its inter cycle variance will be reasonably small with the majority of the pixel intensity change being due to noise. The response strength is indicated by an f score which expresses the agreement between the time course and the activity condition assuming a Gaussian distribution.

Student t test assumes that either a full or zero response will result depending upon whether the stimulus is present, such that data sets can be classified into either ON or OFF states. A t score is attained by comparing the intensity difference between ON and OFF states to the standard deviation, and can subsequently be transformed into an f score.

Correlation analysis assumes an expected response time course and fits the actual time course onto this predictor to derive an r score. An expected time course is appropriately selected to represent the BOLD contrast change, with Gaussian and Gamma functions being typical choices. *Regression* analysis is an extension of correlation analysis, in which the expected response time course is governed by an underlying parameter. The regression analysis fits the expected time course to the acquired time course by least square error fitting. Parameters describing the expected time course and degree of matching can be derived from this procedure.

The above analysis techniques are based on a *general linear model* (GLM), in which the response is assumed to have a linear relationship with the strength of the stimulus or task performance. The GLM is given by

$$\mathbf{S} = \mathbf{C}\mathbf{A} + \epsilon, \tag{2.3.2}$$

where $\mathbf{S}$ is a time serial vector consisting of all the pixel intensities of the data, $\mathbf{C}$ is the design matrix consisting of the expected responses to the presented stimulus or performed tasks, $\mathbf{A}$ is a coefficient vector representing the strength of the corresponding response strength to the stimuli and ϵ is the noise based on a Gaussian distribution. The response strength $\mathbf{A}$ is an indication of the activity of the pixel, and can be derived as $\mathbf{A} = (\mathbf{C}^T\mathbf{C})^{-1}\mathbf{C}^T\mathbf{S}$ by least square error minimization. The desired aspect of the analysis can be attained by constructing a contrast matrix and by applying it to the underlying coefficient matrix. Statistical scores can subsequently be attained by calculating the means and variances of contrasts. Although different kinds of statistical scores can be produced by different statistical analysis methods, any type of score can be transformed into an f score based on Gaussian distributions.

2.3.6 Statistical Inference

The statistical score indicates the degree of matching between the pixel intensity time course and the assumed response or hypothesis. A large statistical score indicates a strong correlation between the hypothesis and the measured time course.

A measure of this matching can be achieved by testing the hypothesis against the null hypothesis. A null hypothesis is defined as there being zero relationship present between the pixel intensity time course and the presence of the stimuli or performed task. The test of the hypothesis is to derive the probability of obtaining the experimental result by pure chance or from sampling error alone. This probability is a conditional probability, in which the condition is the null hypothesis. Since this probability gives the reliability of the conclusion, it is defined as the statistical significance and denoted by p. The p value is calculated based on the statistical score and sample population, while the reduced independence between samples due to the operation of temporal filtering needs to be taken into account. A small p value indicates high reliability and gives high credibility to the attained result.

Since statistical score and significance exhibit the strength and reliability of a relationship, both need to be quoted in a completed conclusion. Active pixels are considered as those in which both statistical score and significance are above given thresholds. However, there may be some debate as to the choice of thresholds selected.

The idea of statistical significance is extended to include spatial dimensions to exclude false active pixels, via cluster detection methods. Cluster detection is based on Gaussian random field theory, in which individual pixels are assumed to be purely independent. Consequently, cluster detection has to take the effect of spatial smoothing into account to indicate effective resolution. The null hypothesis stipulates that a cluster of k pixels are active purely due to sampling error. The threshold p value can be justified according to the expected number of pixels in an active cluster, k, and further depending on the expected number of active pixels and the expected number of clusters based on smoothness. If the probability is greater than the given threshold, the cluster is considered as not representing real activation.

The idea of statistical significance can be further extended to consider inter subject comparisons. However, several issues concerning the validity of such results are unresolved. Since subjects' brains are of different shape, a transformation from an individual brain to a standard brain is required. This transformation often involves stretching and shearing operations, causing complexity in terms of pixel independence and the validity of the subsequent statistical operations carried out. Such group analysis is conducted via fixed effect analysis or random effect analysis, which imposes different definitions of groups according to the analysis method used. The fixed effect analysis does not take inter subject variability into account, causing the possibility of biased result resulting from strong activation within only a small number of subjects. The random effect analysis takes both inter and intra subject variability into account, providing a generally more robust result. The random analysis is suitable for providing inferences of the general population, while the fixed effect analysis is mainly used for case reporting.

The time course of a cluster can be obtained by averaging the time course of individual pixels within the cluster, which may be directly linked with the haemodynamic response. This time course can subsequently be used to direct further studies with similar tasks, to assess response patterns.

The activation map can be transformed onto anatomical images to give an indication of the position of functional sites. Anatomical images are usually T_1 weighted high resolution images acquired with spin warp sequences. A least square operation based on 12 parameter image manipulation is used to bridge the averaged fMRI images and anatomical images. Although the transformation is not physically strict, the results match reasonably well, those expected from intuition and the conclusions from other modalities. The activation site is usually referred to by the centre of mass, the centre of weighted mean. However, the way it is expressed may lead to the appearance that fMRI can achieve a higher resolution than it can in reality, since the number of significant figures can show an accuracy better than the image resolution.

2.3.7 Interpretation of Results

The obtained activation map simply shows those points that meet the hypothesis above a defined strength and reliability threshold. For an ANOVA test, the activation map depicts those pixels whose intensity changes dramatically in a cycle and follows a similar pattern in each cycle. Although this gives an ANOVA test the ability to detect such activations, false activations such as those arising from susceptibility changes in large veins may also be present in the results. This arises due to limitations on the latency of the response patterns, as secondary effects such as those associate with veins often appear with a longer latency than primary activations with a similar rhythm. For a correlation test, activated pixels must possess a good match for both the expected time course and latency. A data set can be processed under different configurations of expected response time course, giving results for different purposes. This technique is useful when sequential processing takes place within a task, where different results can represent various processing regions at different steps. Consequently, statistical analysis methods and hypotheses have to be carefully selected to derive valid conclusions.

The time course of the BOLD response, *haemodynamic response* (HR) varies with different paradigms and among different cortical regions according to many underlying factors of the tissue. The discrete time course is often least squared fitted to a proposed function, *haemodynamic response function* (HRF), based on experience. The most popular HRF is the *Gamma Variate* function, $G_v(t)$, defined as

$$G_v(t) = t^{\alpha} e^{-\beta t}, \tag{2.3.3}$$

where α and β are the configuration parameters to be fitted, and t is the time from the start of stimulus or performed task. The time to peak t_p can be obtained by solving $\frac{dG_v(t)}{dt} = 0$, and has the result $t_p = \frac{\alpha}{\beta}$. Since the *Gamma Variate* function involves a high order and an exponential component, the fitting procedure can easily result in local minima and can heavily depend on the initial choice of α and β. Although multiple resolution fitting is often used to conquer the local minima problem, it has very limited effect on the *Gamma Variate* function fitting due to serious instability of the error space.

Although the detailed shape of the HR varies and is difficult to quantify, the general HRF (Fig 2.17) has several distinct features which may be related to underlying physiological activity. The initial stage of the HR usually has a negative aspect, referred to as the *initial dip*. The initial dip has been shown to be more localized than the positive lobe of the HRF from fMRI and optical imaging studies. Although it is not always observed especially at low field, it is thought to be due to uncoupling of oxygen consumption and CBF. The uncoupling theory states that the initial dip is the result of a latency of CBF to compensate the increased consumption of oxyhaemoglobin. Subsequently, the dilated vessel increases the blood flow, causing oxygenation level over compensation leading to the positive lobe of the HRF. This trend often lasts for around $6s$ after the termination of the stimulus or performed task. The BOLD contrast subsequently decreases at a slower rate than its initial rising edge, signalling the restoring of the regular circulation. The HR comes back to the baseline after approximately twice the time to peak t_p from the start of the stimulus or performed task. An undershoot afterwards is generally believed to be related to a latency mismatch between blood flow recovery and blood volume recovery. The strong coupling theory postulates a balloon model, in which the change in *cerebral blood volume* (CBV) is the cause of the undershoot.

Although capillaries are densely distributed in brain tissues, the BOLD contrast generally arises from the small veins responsible for draining the tissue blood. This raises the question of whether the active pixels actually represent

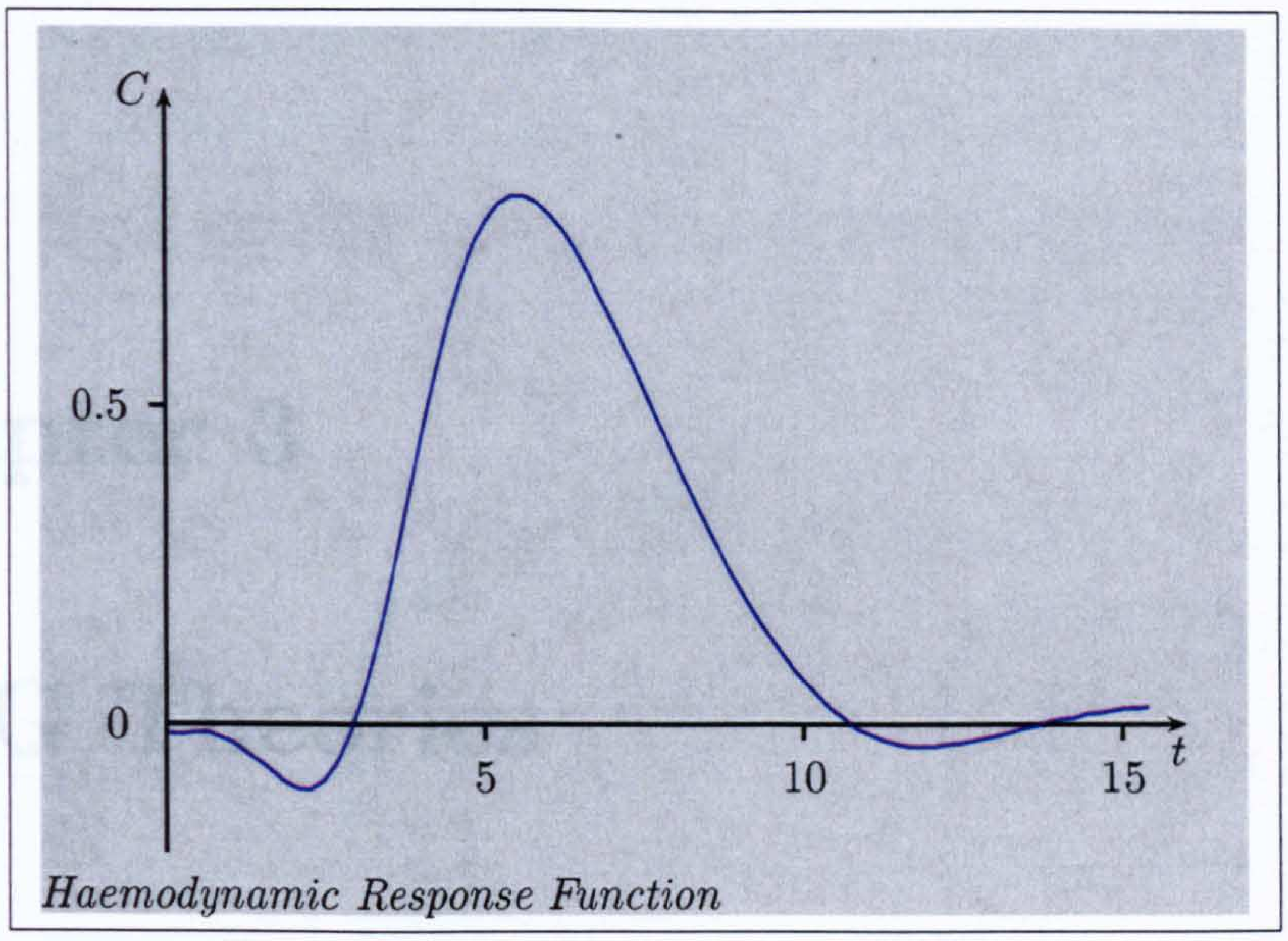

Figure 2.17: A schematic plot of a general haemodynamic response function.

the location of brain activity, with a fundamental resolution of 2-3mm. The BOLD contrast is the result of the balance between several underlying factors, implying an intrinsic difficulty in quantitatively relating the attained HR to the characteristics of brain activity such as amplitude and duration. Due to this factor, the difference between latencies cannot be viewed as an absolute indicator of the path of brain information processes, and the amplitude of the HR does not necessarily represent the strength of brain activity, especially due to its nonlinearity characteristic.

Chapter 3

MEG Theories

3.1 Brain Electrophysiology

3.1.1 Neuronal Structure and Function

Nerve cells are specialized in structure, providing the physical foundation for their distinct physiological properties and, in turn, complex neuronal functions. A nerve cell (Fig 3.1) can be divided on the basis of its structure and function into three main parts: soma, dendrites and axon. The soma is the cell body, structurally similar to that of all other cells, providing infrastructure support to neuron functions. The axon is the long nerve fiber, transferring the signal from the soma to other cells via dendrite processes. The axon may be covered with an insulating myelin sheath divided at regular intervals by the nodes of Ranvier into small sections. Dendrites are the short processes of the cell body and axon in charge of the direct communication with other nerve cells. The dendrites on axon terminals send impulses to other cells, while those on the main cell body receive impulses from other cells and transfer them to the soma. The communication between two cells takes place at the synapses, which are unidirectional junctions formed by outputting dendrites on axon terminals and inputting dendrites on nervous cells. In the human brain, most synapses are chemical synapses, based on the release of neurotransmitters from axon terminals and their binding at receptors on dendrites. A synapse can be either excitatory or inhibitory depending on the type of channels it influences and its action on those channels.

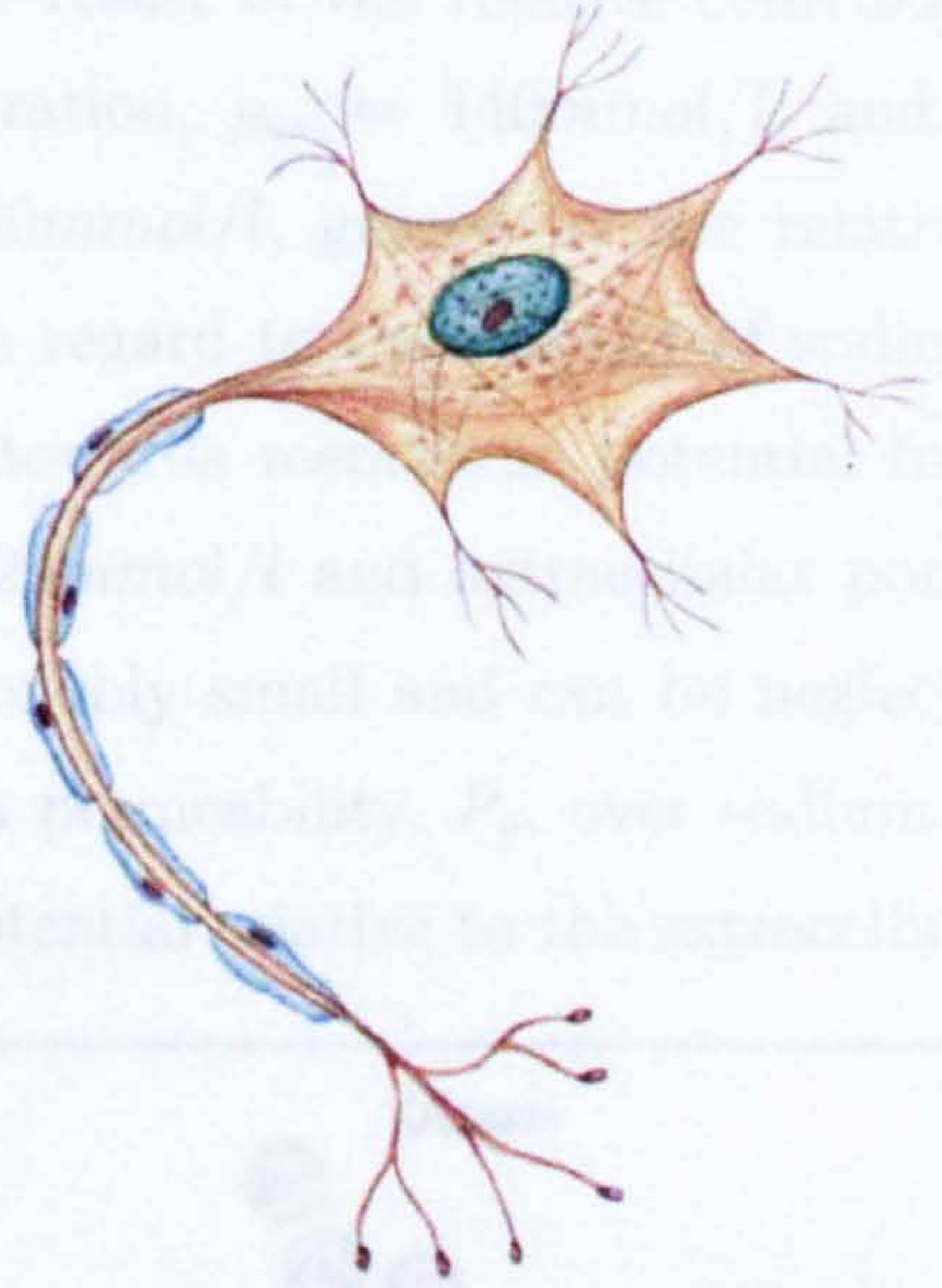

Figure 3.1: A diagram of a typical central nervous cell in human brain.

The unique properties of nerve cell membrane (Fig 3.2) are of great importance in neuronal electro-activities. The chemical composition of the membrane is mainly phospholipid molecules that consist of a hydrophilic head and two hydrophobic tails. The membrane structure is a bilayer of phospholipid molecules, naturally formed by the biochemical properties of the phospholipids. Proteins are embedded into this bilayer structure to form ionic channels, through which specific types of ions can diffuse or be actively transported through the membrane depending on the channel type. The mechanism of selective permeability and active transport of ions enables the existence of ionic concentration difference across the membrane, consequently inducing membrane potential. The resting membrane potential is determined by the balance between thermal diffusion due to chemical density gradients and electric forces, and is described by Goldman's equation [65]

$$V = \frac{k_B T}{|e|} \ln \left(\frac{P_p \rho_{ip} + P_s \rho_{is}}{P_p \rho_{ep} + P_s \rho_{es}} \right), \tag{3.1.1}$$

where the intracellular and extracellular properties are denoted by subscription

i and e respectively. ρ and P represent the concentration and permeability of sodium subscripted by s, and potassium subscripted by p. k_B is the Boltzman constant and e represents the electron charge. The potential formed across the membrane is mainly the result of the relative contribution between the extracellular sodium concentration, $\rho_{es} = 140mmol/l$, and intracellular potassium concentration, $\rho_{ip} = 140mmol/l$, geared by the relatively large population of potassium channels with regard to the amount of sodium channels. In the rest state, the contribution towards membrane potential from intracellular sodium concentration of $\rho_{is} = 20mmol/l$ and extracellular potassium concentration of $\rho_{ep} = 5mmol/l$, is reasonably small and can be neglected. This results in the dominance of potassium permeability, P_p, over sodium permeability, P_s, and a negative intracellular potential relative to the extracellular potential.

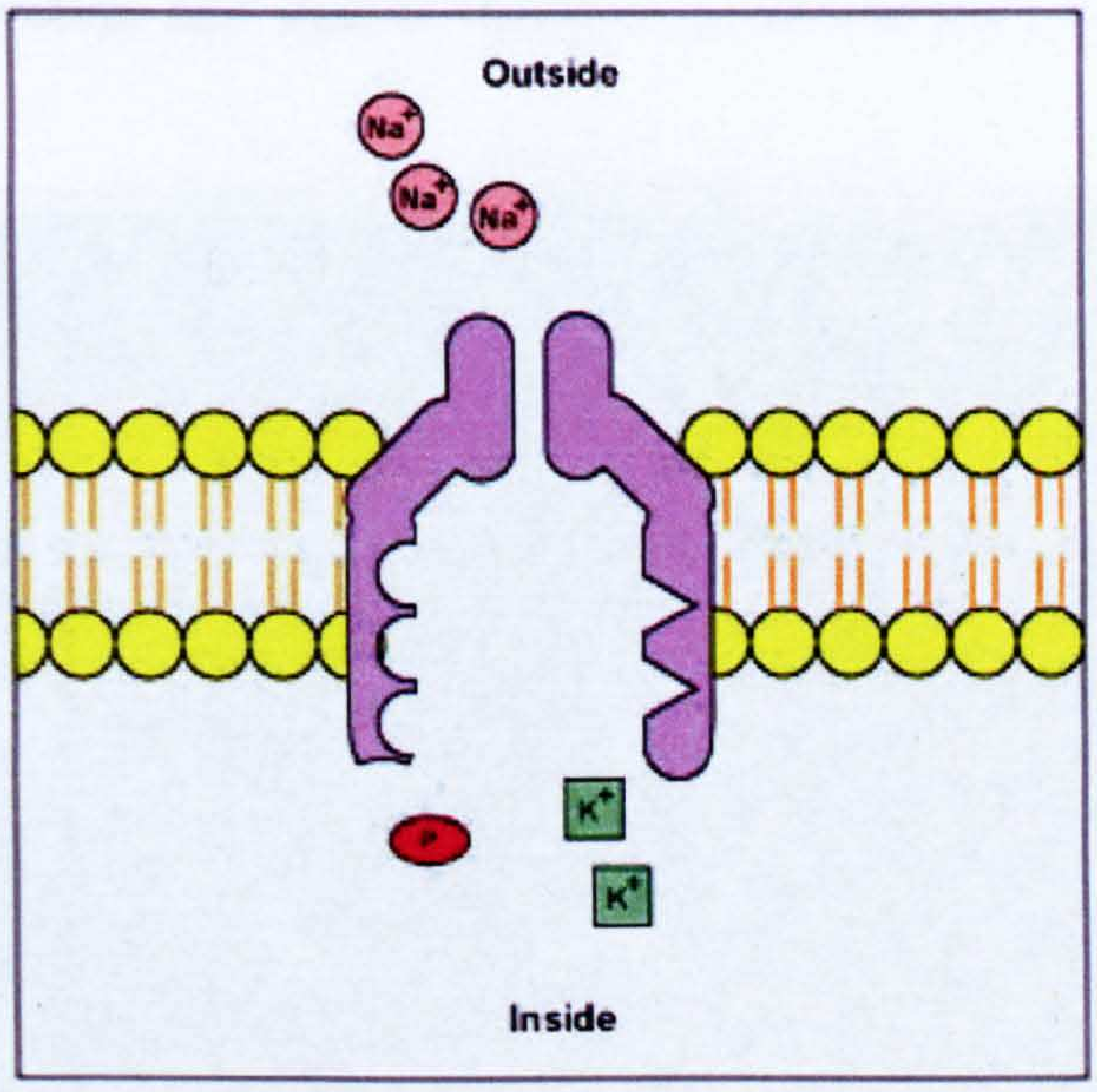

Figure 3.2: A diagram showing the active transport of sodium and potassium ions by the proteins embedded in the membrane.

A type of sodium channel embedded in the membrane is voltage sensitive, and can be opened at a certain membrane potential threshold. The electric inputs from surrounding nervous cells through a single synapse is generally subthreshold and decays with time and distance, while an appropriate temporal spatial combination of synaptic inputs may generate a stimulus above this threshold.

An action potential (Fig 3.3) is produced when a stimulus reaches this threshold, during which the sodium inflow is greater than potassium outflow, triggering voltage-sensitive sodium channels to open and forming a positive feedback loop. The potassium voltage sensitive channels respond to this potential change with a fixed latency, which has the opposite effect to the opening of the sodium channels and brings the membrane potential back to the baseline. The change in the relative population of the ionic channels is so significant that a minor net ionic flow is sufficient to produce the action potential, although the ions still need to be actively transported back to maintain the ionic concentration gradient. The conformation of voltage sensitive ionic channels is restored during the refactory period, when no action potential can be triggered. Since the action potential is based on the properties of the membrane, its form is constant and independent of the source activation and thus is therefore no attenuation during information transmission.

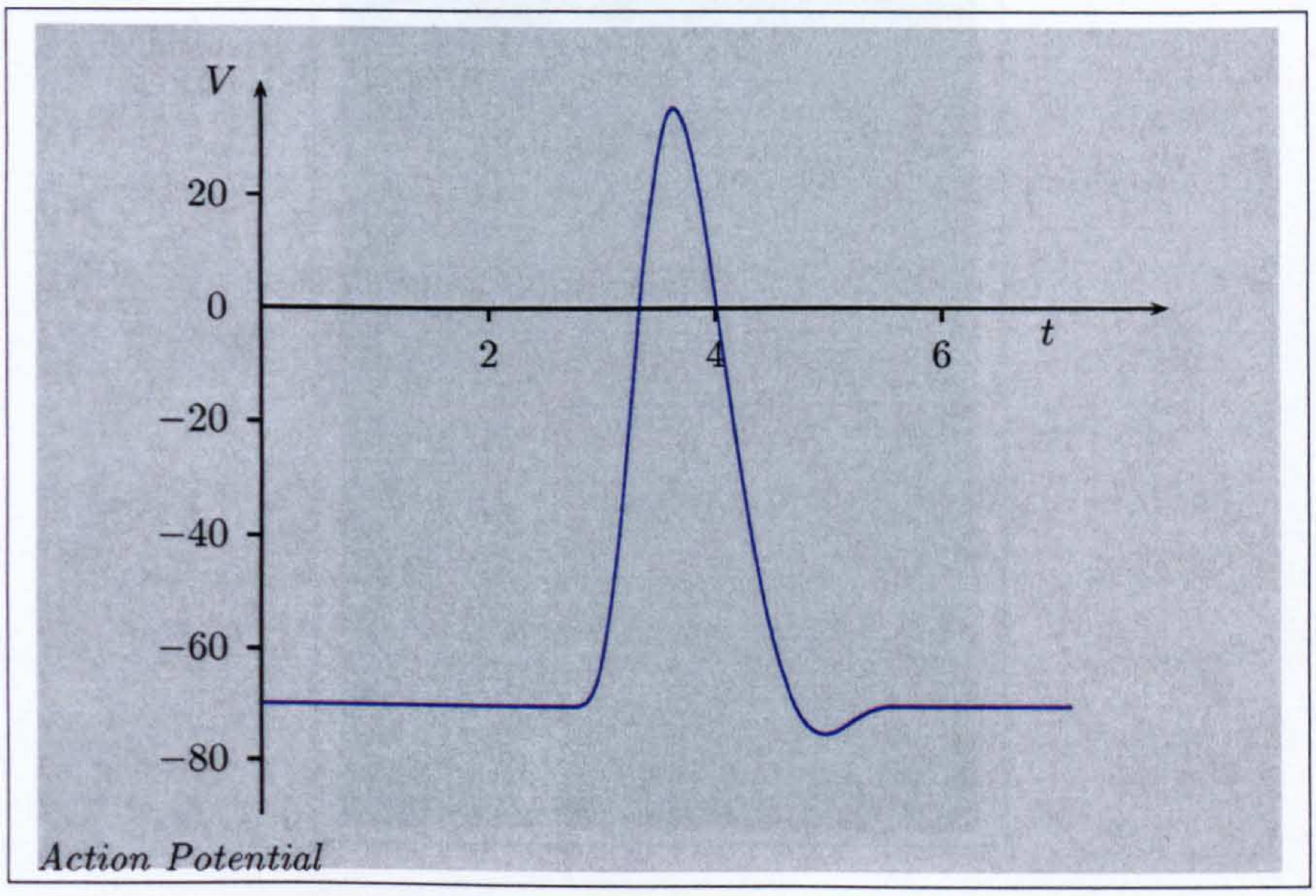

Figure 3.3: Action potential with characteristics independent of input signal.

An action potential at a point site on the membrane is strong enough to trigger action potentials nearby. Due to the refactory period, the action potential is conducted away from the source. A thicker axon conducts action potentials faster due to less signal impendence, while a myelinated axon propagates signals at nodes of Ranvier, accelerating the signal conduction and saving energy.

3.1.2 Sources of MEG Signals

The change in membrane potential due to neuronal activity involves the net displacement of ions. The movement of ions is directly related to the generation of electrical currents. Consequently the neuronal activity can be represented by current densities due to ionic movement. Because of its active role in the electrophysiology, ionic currents are entitled primary current. Since the human head is a conductive medium, the electromagnetic fields caused by primary currents influence ions in the medium and induce passive ohmic currents. The ohmic currents, also called volume currents, complete the ionic flow loop to ensure no buildup of charges.

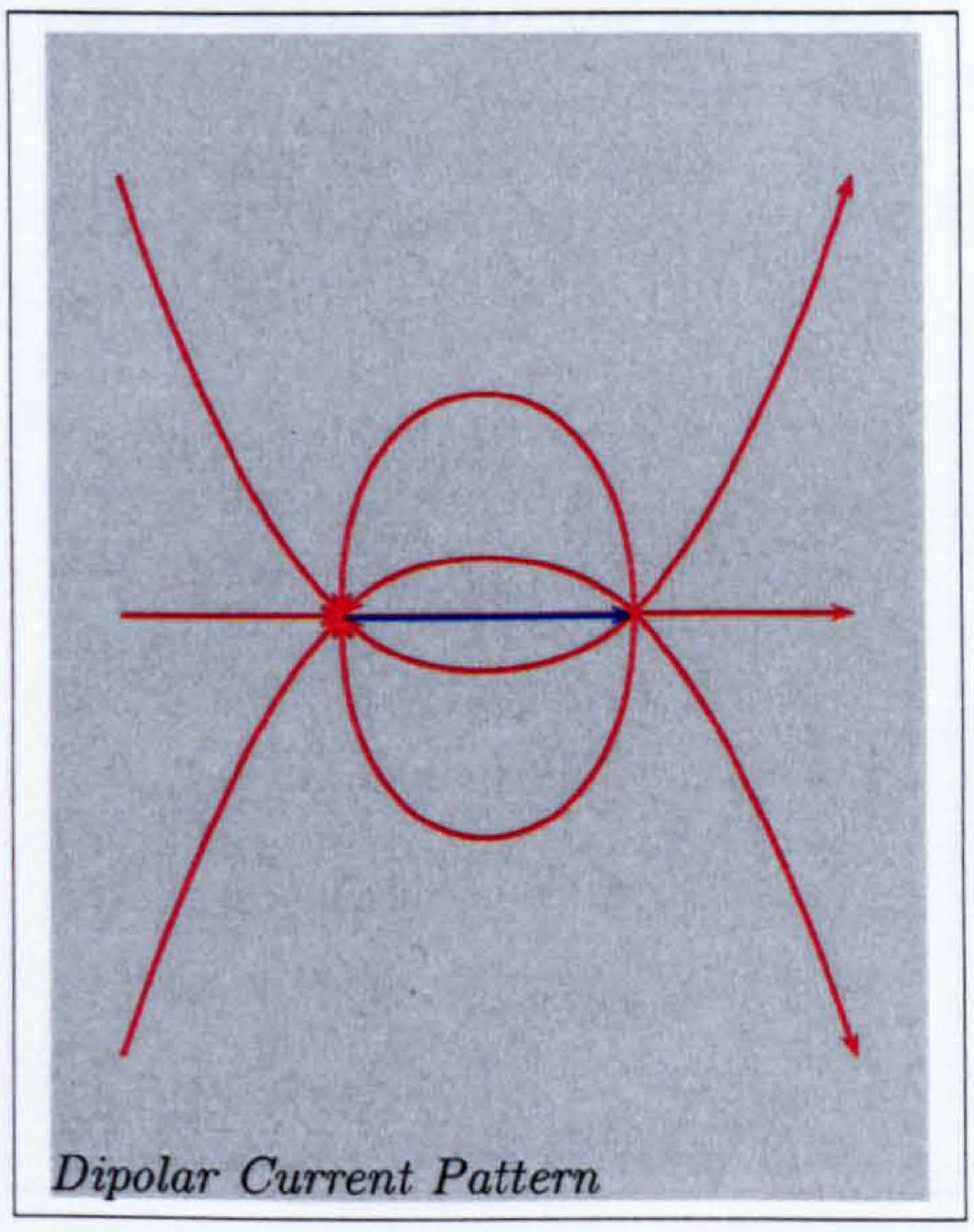

Figure 3.4: A current dipole and its return currents.

A current dipole is developed as the basic mathematical approximation to represent the electromagnetic field source. A current dipole (Fig 3.4) is composed of positive and negative charges with a primary current flowing in a straight line between them and the return currents flowing in a dipolar pattern through the conductive medium. The typical strength of detectable current dipoles is $10nAm$

formed by the synchronous activities of tens of thousands of neurons. The configuration of two current dipoles of the same amplitude but opposite orientation separated by a small space is called a current quadrupole (Fig 3.5). Magnetic fields from quadrupoles decrease rapidly with distance, contributing insignificantly to extracranial magnetic fields. Compared to current dipoles, the first order approximation to the current density distribution, quadrupole are the second order estimation and can be ignored in most cases. The electrical currents (Fig 3.6) induced by neuronal activities are spatially categorized into intracellular currents, transmembrane currents and extracellular currents. The transmembrane currents are distributed in a spatial radially symmetric manner, providing little contribution to the extracranial magnetic field. In this case, the intracellular and extracellular currents match the roles of currents involved in the current dipole model, thus the current dipole model is physically meaningful and valid to use.

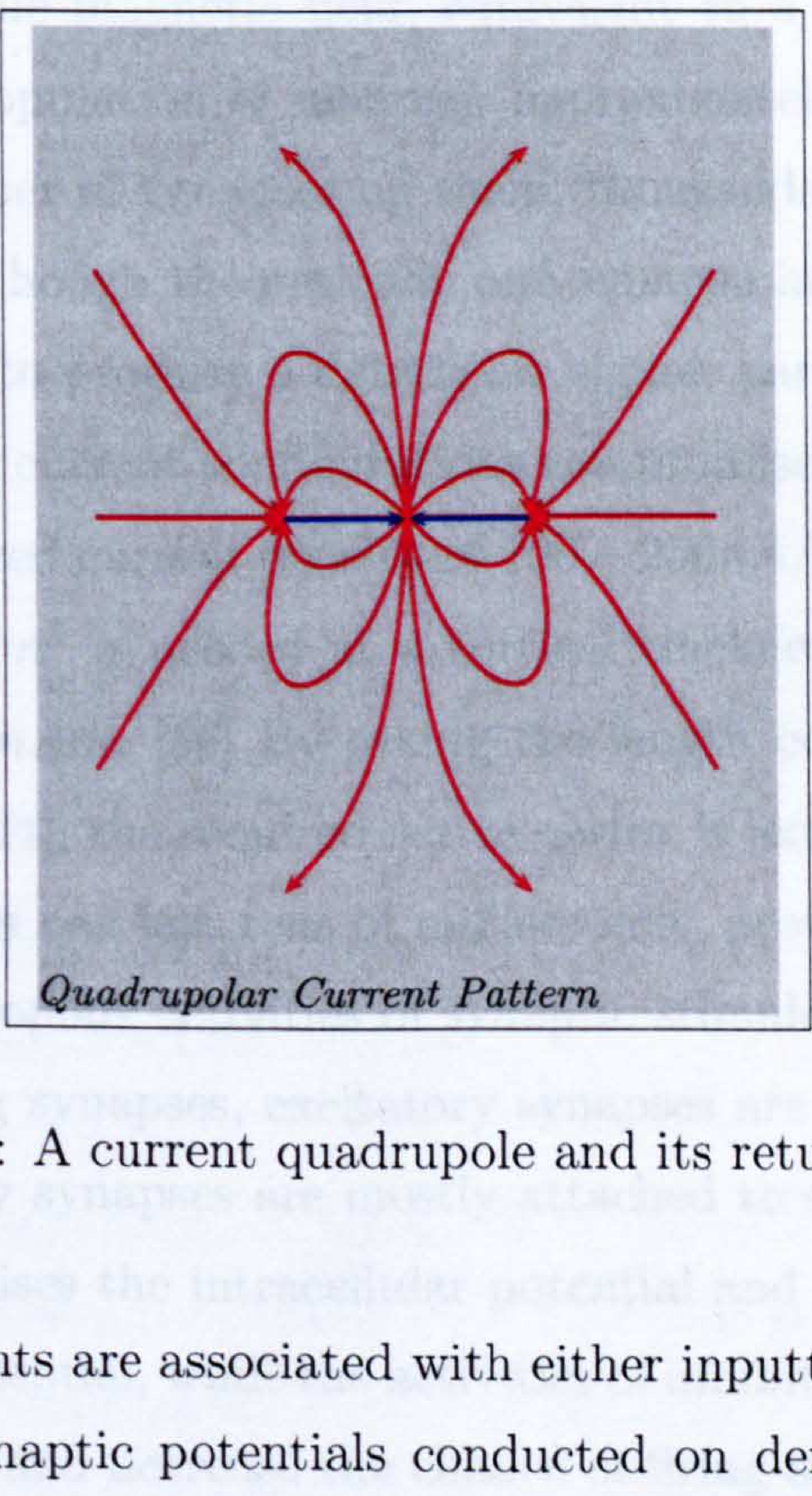

Figure 3.5: A current quadrupole and its return currents.

Intracellular currents are associated with either inputting or outputting electrical signals. Postsynaptic potentials conducted on dendrites and action potentials propagating on the axons form the inputting and outputting signals respectively. Postsynaptic potentials stimulated in the middle of the dendrite are conducted both towards and away from the soma, producing a negligible current quadrupole. However, a distal postsynaptic potential input can produce a current dipole with its orientation depending on the nature of synapses. The strength of its corresponding current dipole is $Q = I\lambda$, where λ is the characteristic length constant and I is the current through the synapse. The length constant based on exponential decay is given by $\lambda = \frac{1}{\sqrt{g_m r_s}}$, where g_m and r_S are the conductance of the membrane and the resistance of the intracellular fluid per unit length respectively, giving the typical length as $\lambda = 0.1 - 0.2mm$ in a cortical neuron. [58] The current I can be calculated from the voltage change ΔV during the postsynaptic potential and is given by $I = \frac{\Delta V}{\lambda r_s}$ and $r_s = \frac{4}{\pi d^2 \sigma_i}$, where d is the diameter of the dendrite and σ_i is the intracellular conductivity. Based on typical values $d = 1\mu m$, $\sigma_i = 1\Omega^{-1}m^{-1}$ and $\Delta V = 25mV$, the typical current dipole strength is $Q = \frac{\pi d^2 \sigma_i \Delta V}{4} \simeq 20fAm$. The postsynaptic potential is so small that more than one million synchronously active synapses are needed to generate a detectable magnetic field, equivalent to a dipole of the order of $10nAm$. The dense population of neurons, approximately 10^5 per mm^2 at the cortex, and huge number of synapses on them, thousands per neuron, make the detection possible. Although theoretically one synapse in one thousand over an area of $1mm^2$ suffices to produce a detectable signal, partial cancellation of the signal due to opposing current configurations compromises the signal detectability. Based on a measured current density of $100 - 250nA/mm^2$ [53,55], an active cortical region of $40mm^2$ is needed at a cortical thickness of $1mm$ to generate a current dipole of $10nAm$. [56] By taking the length constant $\lambda = 0.2mm$ as the relevant distance [41], the required active cortex is extended to $200mm^2$ [42]. Postsynaptic potentials can last tens of milliseconds, providing a large temporal window for the synchronous activities of synaptic stimulation. Among typically thousands of inputting synapses, excitatory synapses are often attached to dendrites, while inhibitory synapses are mostly attached to soma. The activities of excitatory synapses raises the intracellular potential and increase the possibility of triggering action potential, while the activities of inhibitory synapses lowers the intracellular potential and decrease the chance of firing action potential. An action potential is triggered when the intracellular potential at a membrane region reaches the threshold potential. An action potential has depolarizing rising and repolarizing falling phases, modelled by two current dipoles of opposite directions and consequently forming a current quadrupole. The quadrupole is constructed by two current dipoles, each of $100fAm$ in strength due to the large amplitude of potential change, whose spatial separation depending on the velocity of conduction v is about $1mm$ in an unmyelinated cortical axon where $v \simeq 1m/s$. The short temporal window of $1ms$ and restricted spatial extent of induced fields due to the current quadrupole configuration limit the possibility of its detection. Therefore currents caused by postsynaptic potential stimulation conducted on dendrites are the dominant sources of extracranial magnetic field. However, action potentials have been detected both electrically and magnetically in peripheral nerves [39], and also theories on contribution of action potentials towards high frequency extracranial electromagnetic fields have been proposed.

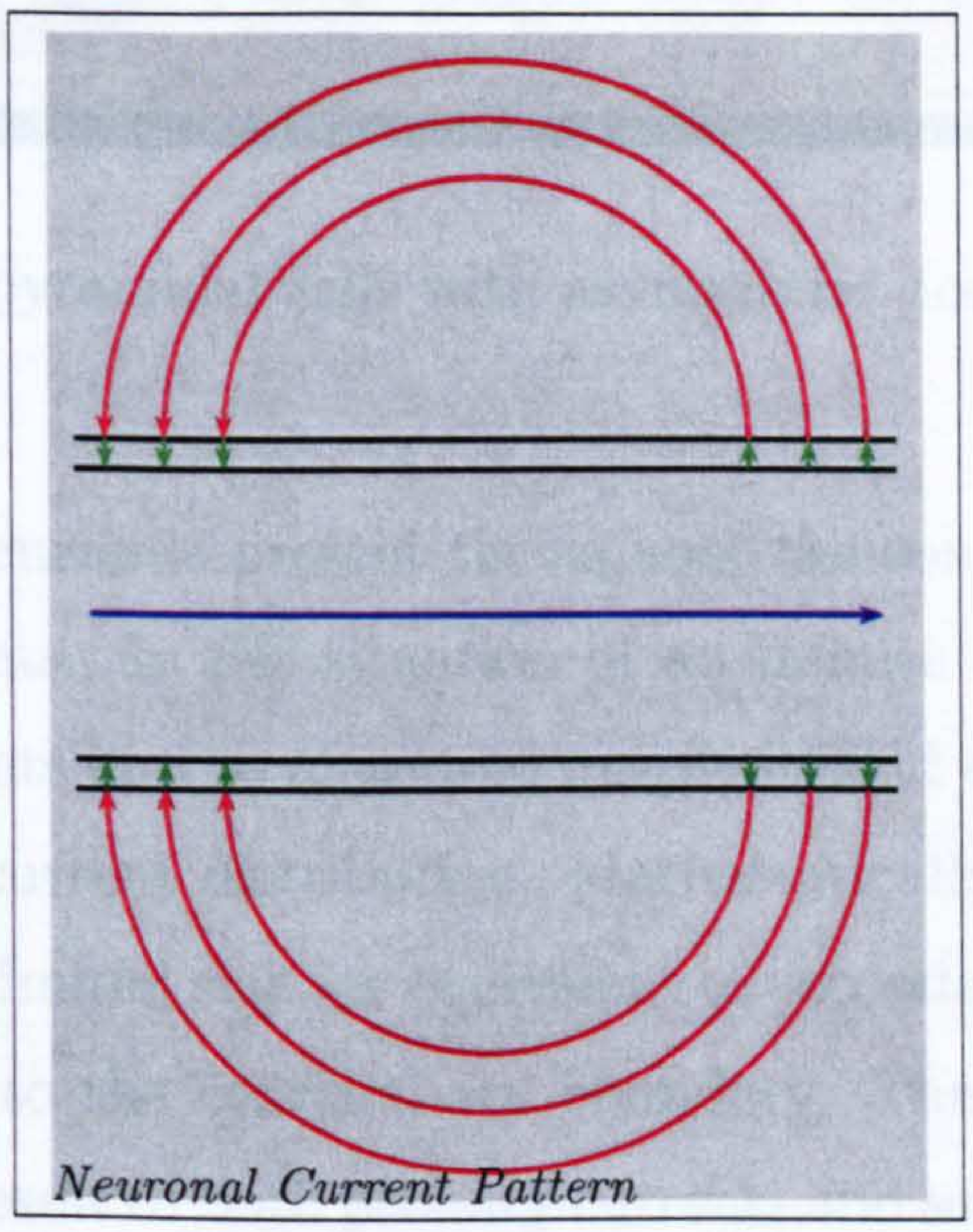

Figure 3.6: The neuronal current distribution pattern divided into intracellular, extracellular and transmembrane currents

The strength of extracranial magnetic field depends on not only the population of postsynaptic dendritic currents but also their geometric characteristics. Symmetric dendritic configurations, such as the case in stellate cells (Fig 3.8), restrict the electrical potential variations within the region of the dendritic field, producing no significant effect at distance. By contrast, pyramidal cells (Fig 3.7) have highly asymmetric dendritic tree configurations, capable of generating large net current dipoles and inducing significant extracranial magnetic fields at distance.

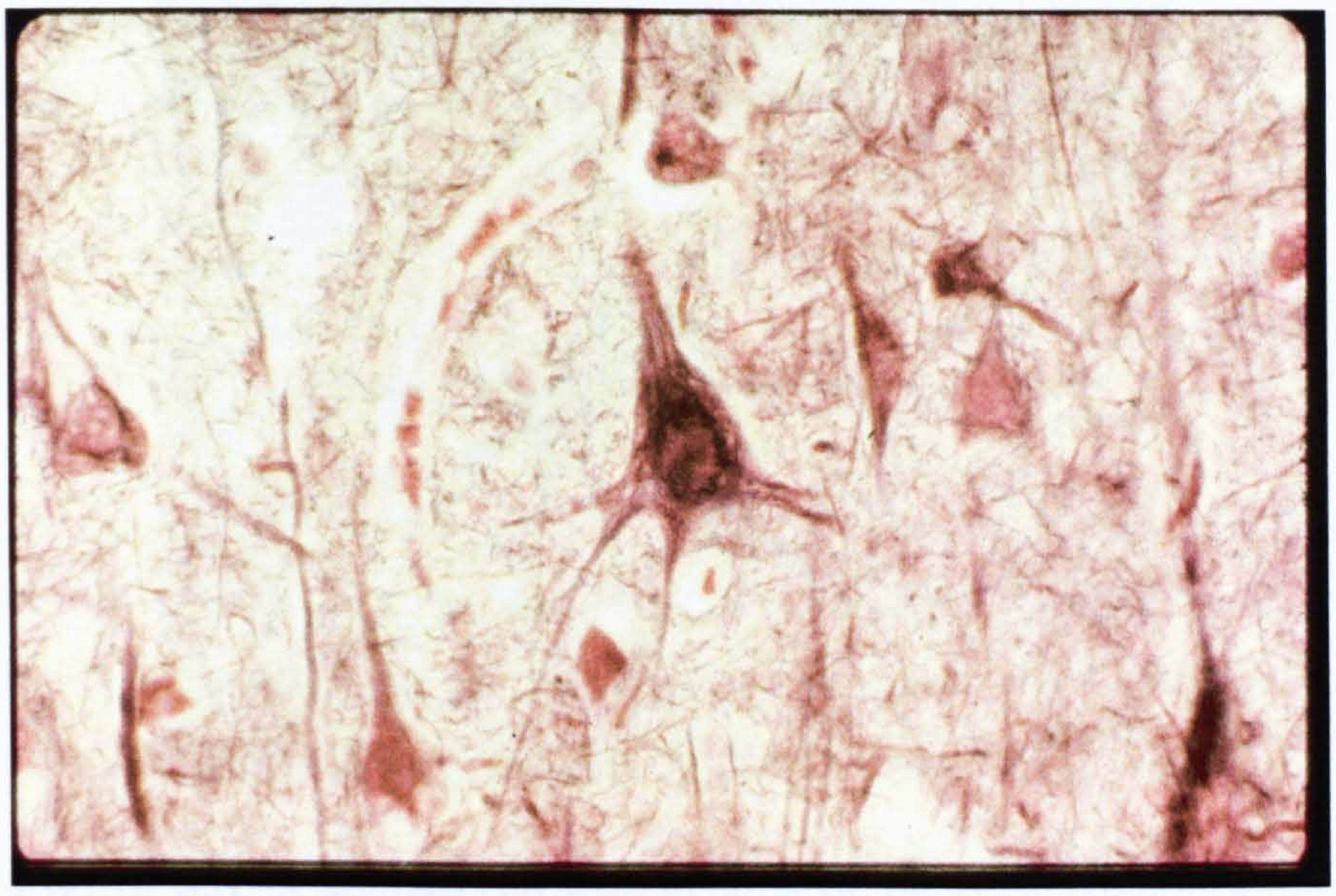

Figure 3.7: The pyramidal cells with asymmetric dentritic distribution.

The extracellular currents present throughout the conductive medium in the form of volume currents. In the situation of an infinite uniform conductor, no effect of volume currents on the measured magnetic field can be observed due to the symmetry of the current distribution. Mathematically, volume currents in a uniform conductor of limited size are equivalent to secondary currents distributed at and perpendicular to the conductivity boundary. The extracranial magnetic field is the combined result of both primary currents and secondary currents based on superposition theory.

The human brain can be divided into two parts referred to as gray matter and white matter. Gray matter mainly contains neuronal cell bodies and dendrites, forming the top layer of human brains. White matter, named after its white appearance from myelinated axons, mostly consists of nerve fibers, providing neuronal connections between different cortex. Since pyramidal neurons constitute nearly 70 percent of cortical neurons and are organized into cortical columns and orthogonal laminae, it is believed that postsynaptic activities in pyramidal cells in cortex are the dominant source of detected extracranial magnetic field.

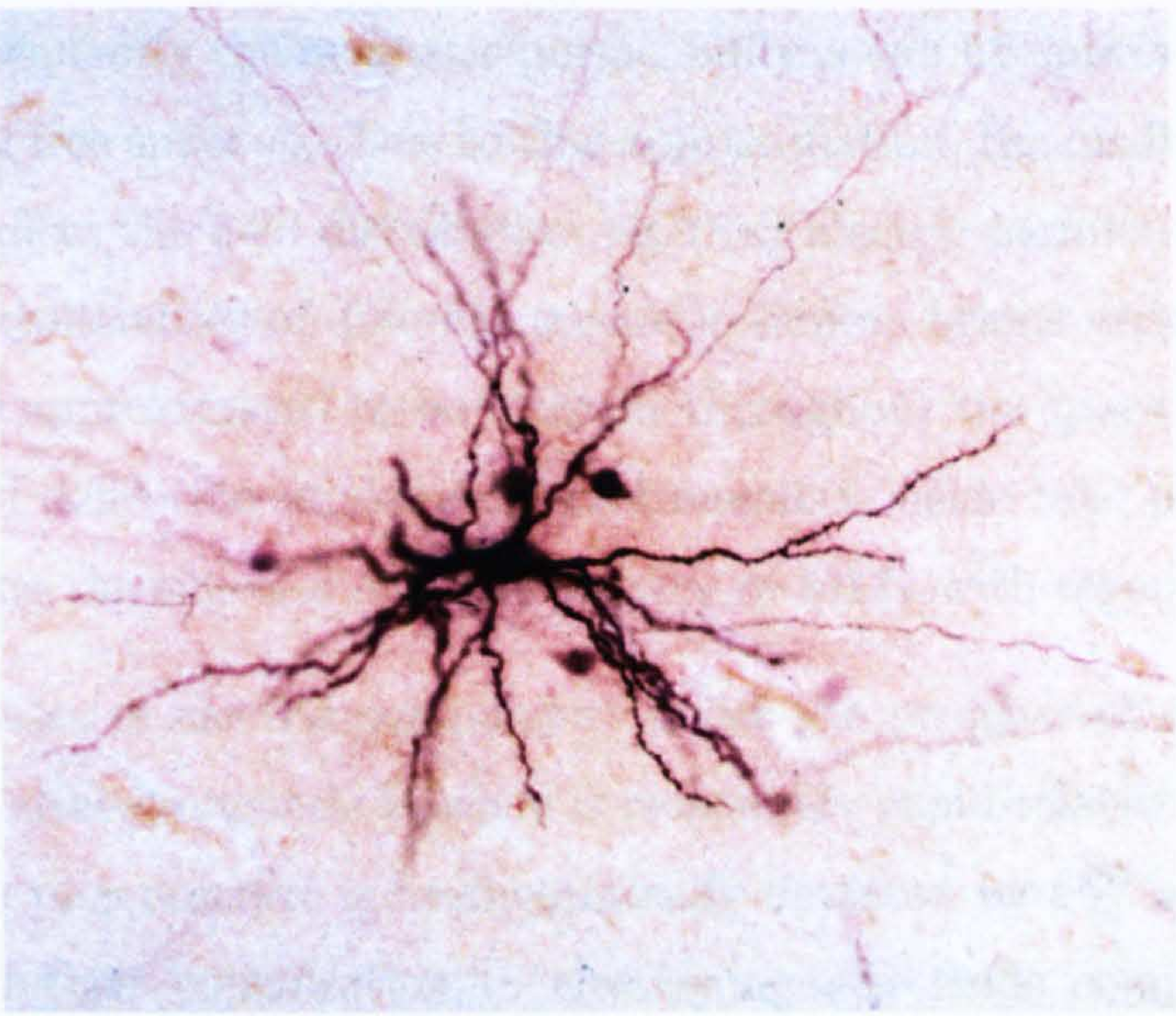

Figure 3.8: A stellate cell with symmetric dentritic configuration.

3.2 Physical Models

3.2.1 Forward Problem

Based on a full knowledge of the primary current sources and electromagnetic configuration, extracranial magnetic fields can be calculated according to Maxwell's equations [38]

$$\nabla \cdot \mathbf{E} = \frac{\rho}{\varepsilon} \tag{3.2.1}$$

$$\nabla \times \mathbf{E} = -\frac{\partial \mathbf{B}}{\partial t} \tag{3.2.2}$$

$$\nabla \cdot \mathbf{B} = 0 \tag{3.2.3}$$

$$\nabla \times \mathbf{B} = \mu\left(\mathbf{J} + \varepsilon\frac{\partial \mathbf{E}}{\partial t}\right) \tag{3.2.4}$$

where ε and μ are the permittivity and permeability of the material respectively, and ρ is the charge density. The current $\mathbf{J}$ stands for both primary currents and ohmic currents, and $\mathbf{E}$ and $\mathbf{B}$ are the electric field and magnetic induction in the space respectively. The process of deriving the extracranial magnetic field according to electromagnetic principles is termed the forward problem.

In organic structures such as human brains, the susceptibility is reasonably small and consequently the magnetic permeability μ can be approximated by the permeability of free space μ_0. Due to this approximation, the medium-dependent features only affect the field distribution via their electric permittivity. However, the electric permittivities of different tissues in human brains varies significantly and cannot be approximated to be uniform throughout the space. The different degrees of field deflection in electrical and magnetic fields take place in human brains, implying the superior spatial accuracy of MEG with regard to EEG.

The responses of electric components under the presence of electric field to reach internal electromagnetic balance is reasonably rapid relative to the change in fields. This phenomenon is mathematically depicted by $\varepsilon\frac{\partial \mathbf{E}}{\partial t} = 0$ and $\frac{\partial \mathbf{B}}{\partial t} \rightarrow 0$, in terms of their contribution to electromagnetic fields compared to other terms. Since Maxwell's equations are consequently simpified to a static scenario, this approximation is termed the quasistatic approximation. In the light of the quasistatic approximation, the scalar potential of V can be used to simplify the vector calculations of $\mathbf{E} = -\nabla V$, since $\nabla \times \mathbf{E} = 0$. Although in a typical human head the frequency of the fields needs to be over $100kHz$ to allow time variant terms reach same order as static terms and undoubtedly violate the quasistatic approximation, the degree of correctness of the quasistatic approximation has to be carefully evaluated for high frequency brain activity studies such as those focusing on the dynamics of action potentials.

Based on approximations, effective representation of scalar potential V to electric field $\mathbf{E}$ and discriminating primary currents and ohmic currents, the simplified Maxwell's equations are given by

$$\nabla^2 V = -\frac{\rho}{\varepsilon} \tag{3.2.5}$$

$$\nabla \cdot \mathbf{B} = 0 \tag{3.2.6}$$

$$\nabla \times \mathbf{B} = \mu_0 (\mathbf{J}^p + \mathbf{J}^v) \tag{3.2.7}$$

where $\mathbf{J}^p$ represents primary currents and $\mathbf{J}^v$ stands for ohmic currents. The ohmic currents are also called volume currents driven by electric fields as $\mathbf{J}^v = \sigma\mathbf{E} = -\sigma\nabla V$, where σ is the electric conductivity. In order to model the whole cortex as a continuous or homogenous and isotropic conductor, cellular level details are ignored and the conductivity is viewed at macroscopic level. However, since the membrane is a good electric insulator such that the conductivities along and perpendicular to the axon are significantly different, the use of this model may introduce a significant error into the result under certain circumstances. Primary currents originate from neuronal activity due to postsynaptic potentials, while volume currents are the passive current due to the influence of the macroscopic electric field on charge carriers in the conducting medium. The functional analysis of MEG is ultimately to monitor the location and amplitude of primary currents during neuronal activity.

Replacing the ohmic currents $\mathbf{J}^v$ with $-\sigma\nabla V$, it follows that $\nabla\cdot\mathbf{J} = \nabla\cdot\mathbf{J}^p - \nabla\cdot(\sigma\nabla V)$. Since $\nabla\cdot\mathbf{J} = \frac{1}{\mu_0}\nabla\cdot\nabla\times\mathbf{B} = 0$, it is apparent that $\nabla\cdot\mathbf{J}^p = \nabla\cdot(\sigma\nabla V)$. Consequently, the electric potential V and in turn the magnetic field $\mathbf{B}$ can be solved either analytically or numerically with finite element techniques, depending on the boundary conditions.

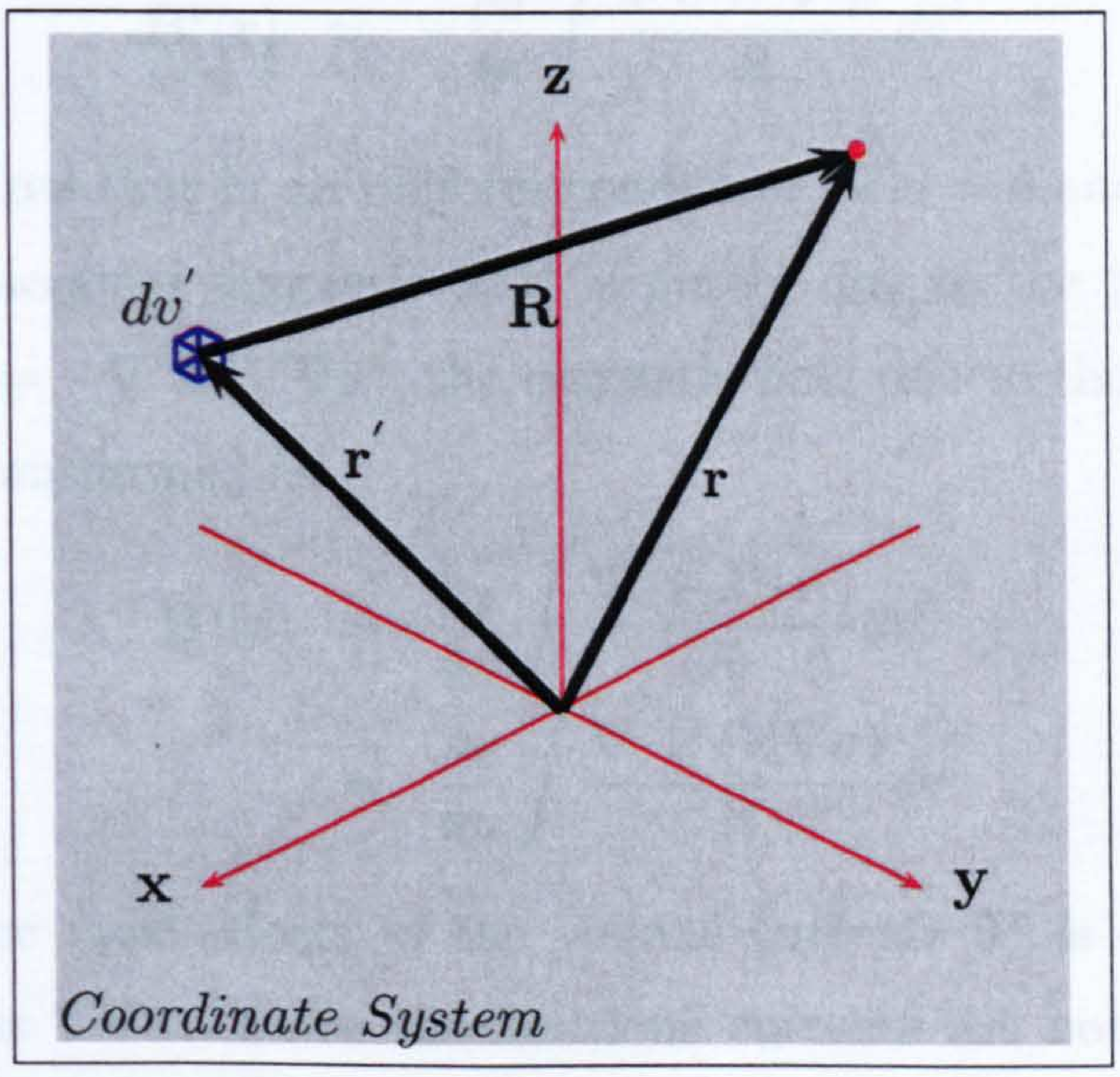

Figure 3.9: The coordinate system of the forward problem.

The direct relationship between magnetic field and electric currents is given by the Biot-Savart law [37] as

$$\mathbf{B}(\mathbf{r}) = \frac{\mu_0}{4\pi}\int\frac{\mathbf{J}(\mathbf{r}')\times\mathbf{R}}{R^3}dv', \tag{3.2.8}$$

where the current $\mathbf{J}(\mathbf{r}')$ is the the current distributed in volume element dv' at

$\mathbf{r}'$ (Fig 3.9). The vector $\mathbf{r}$ is the detection position and $\mathbf{R} = \mathbf{r} - \mathbf{r}'$ with R referring to its scalar value. Based on vector analysis of $\frac{\mathbf{R}}{R^3} = -\nabla\frac{1}{R} = \nabla'\frac{1}{R}$, and it can be shown that $\mathbf{J} \times \nabla'\frac{1}{R} = \frac{\nabla' \times \mathbf{J}}{R} - \nabla'\frac{\mathbf{J}}{R}$. The volume integral of $\nabla'\frac{\mathbf{J}}{R}$ can be transformed into a surface integral and has no contribution to the extracranial magnetic field due to the spatial restriction of $\mathbf{J}$ in biological systems. Taking the above factors into account, the extracranial magnetic field is given by

$$\mathbf{B}(\mathbf{r}) = \frac{\mu_0}{4\pi}\int \frac{\nabla' \times \mathbf{J}(\mathbf{r}')}{R} dv'. \tag{3.2.9}$$

This result can be further divided into terms of primary and ohmic currents as $\mathbf{B}(\mathbf{r}) = \mathbf{B}^p(\mathbf{r}) + \mathbf{B}^v(\mathbf{r})$, based on superposition theory. The extracranial magnetic field is thus given by

$$\mathbf{B}^p(\mathbf{r}) = \frac{\mu_0}{4\pi}\int \frac{\nabla' \times \mathbf{J}^p(\mathbf{r}')}{R} dv' \tag{3.2.10}$$

$$\mathbf{B}^v(\mathbf{r}) = -\frac{\mu_0}{4\pi}\int \frac{\nabla'\sigma \times \nabla' V}{R} dv'. \tag{3.2.11}$$

It can be recognized that in an uniform conductor, $\nabla'\sigma = 0$ and in turn $\mathbf{B}^v = 0$, so that the extracranial magnetic field is purely due to the primary currents. Since $\nabla\sigma \times \nabla V = -\nabla \times (V\nabla\sigma)$, the magnetic field due to the volume currents can be further transformed as

$$\mathbf{B}^v(\mathbf{r}) = \frac{\mu_0}{4\pi}\int \frac{\nabla' \times \mathbf{J}^v(\mathbf{r}')}{R} dv' \tag{3.2.12}$$

$$= \frac{\mu_0}{4\pi}\int \frac{\nabla' \times (V\nabla\sigma)}{R} dv', \tag{3.2.13}$$

implying that the total effects of the volume currents $\mathbf{J}^v$ is equivalent to the fictitious currents $V\nabla\sigma$. Since the fictitious currents are not present inside a homogenous conductor dictated by $\nabla\sigma = 0$, it is only distributed at the electric conductivity boundaries. Consequently, the contribution of the volume currents to the extracranial magnetic field can be described in a surface integral as

$$\mathbf{B}^v(\mathbf{r}) = \frac{\mu_0}{4\pi}\Delta\sigma \int V(\mathbf{r}')\frac{\mathbf{R}}{R^3} \times d\mathbf{S}, \tag{3.2.14}$$

where $\Delta\sigma$ is the difference between conductivities of the second and first medium, and $d\mathbf{S}$ is the surface element with its direction pointing from the first to the second medium and perpendicular to the surface. [36] Simple electric medium

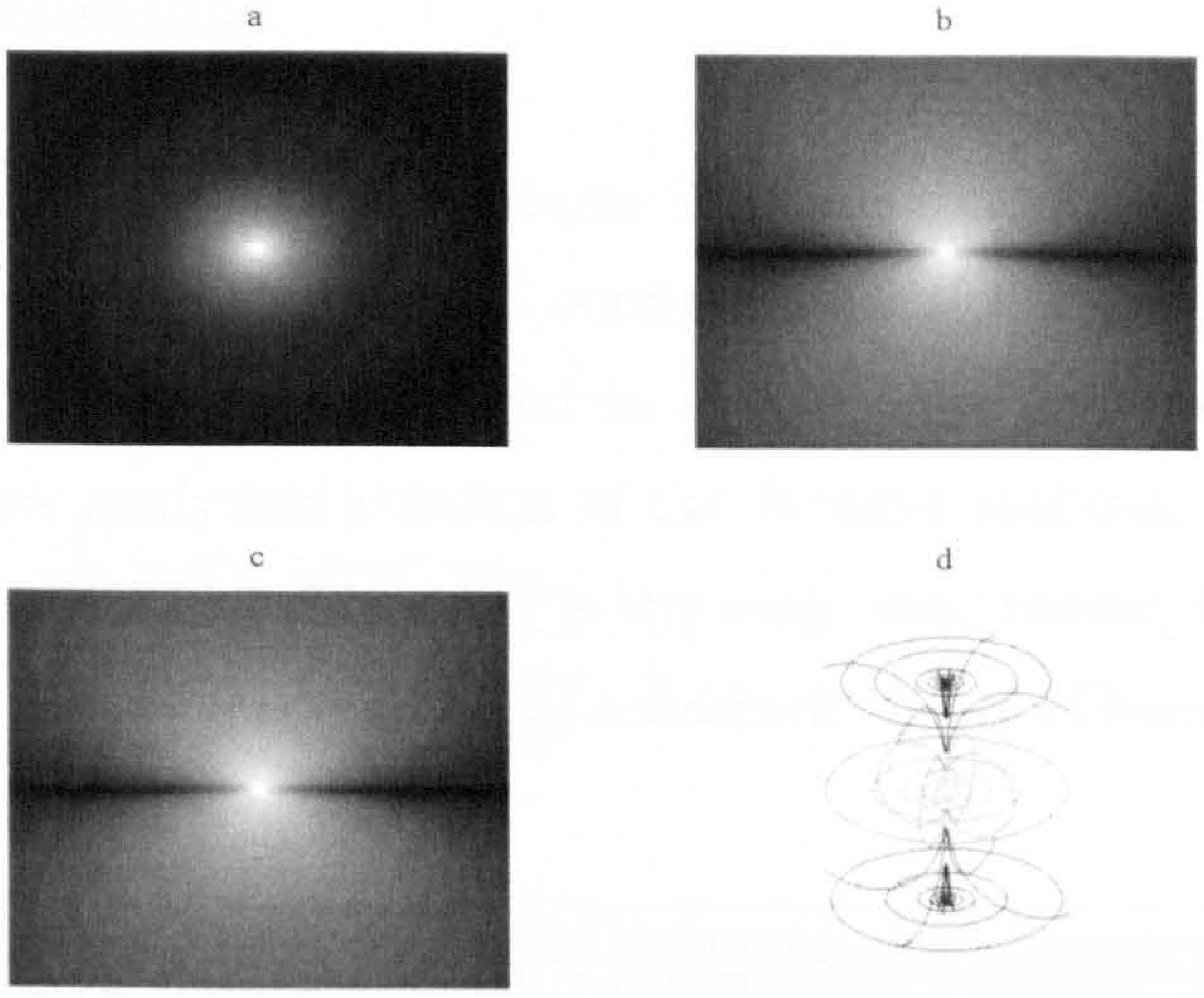

Figure 3.10: The amplitude of the magnetic field in logarithmic unit generated by a current dipole located at the centre of the space pointing along z-axis. (a) $z = 0$ plane (b) $x = 0$ plane (c) $y = 0$ plane (d) space contour.

configurations allow analytical solutions for the term of ohmic currents, while numerical methods have to be used otherwise.

The introduction of a current dipole (Fig 3.10) further simplifies the analysis of the physical scenario, and simplifies vector calculus into vector algebra. A current dipole with a momentum $\mathbf{Q}$ is a concentration of currents to a single point $\mathbf{r}_0$, as $\mathbf{J}^p(\mathbf{r}) = \delta(\mathbf{r} - \mathbf{r}_0)\mathbf{Q}$. The current dipole is conceptually the first order term of current multipole expansion with $\mathbf{Q} = \int \mathbf{J}^p(\mathbf{r})dv$. [34] Consequently, the magnetic field induced by primary currents is given by

$$\mathbf{B}^p(\mathbf{r}) = \frac{\mu_0}{4\pi}\mathbf{Q} \times \frac{\mathbf{R}}{R^3}. \tag{3.2.15}$$

For the case of a multidipole scenario, the total magnetic field is the summation of individual contributions following superposition theory.

3.2.2 Head Models

Since the distribution of ohmic currents and their contribution to extracranial magnetic field largely depends on the configuration of the conductive medium, many head models have been proposed to simplify the analysis of current distributions and allow analytical solution of the forward problem. The spherically symmetric conductor model (Fig 3.11) is the most used model, in which the human head is assumed to be composed of concentric layers of homogenous electric conductors.

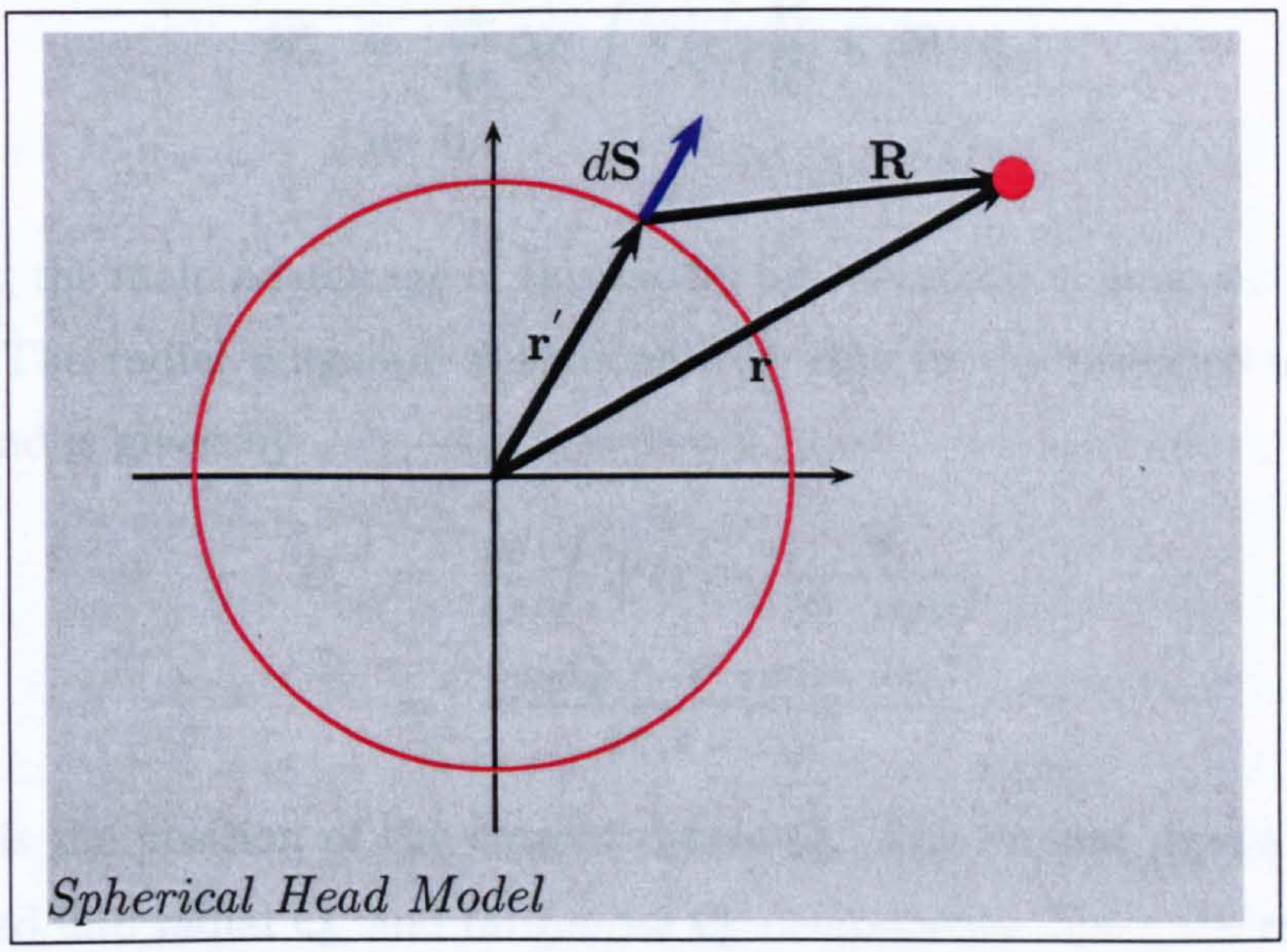

Figure 3.11: The coordinate system adopted in this section to demonstrate the spherically symmetric conductor model.

Based on its geometry, volume currents are distributed as surface currents oriented radially, because of the perpendicular orientation of surface currents to the electric boundaries as $\mathbf{J}^v = V\nabla\sigma$. The radial component of a magnetic field is given by

$$B_r = \mathbf{B}(\mathbf{r}) \cdot \mathbf{e}_r, \tag{3.2.16}$$

where the origin of the space is defined at the centre of the sphere, and the radial direction $\mathbf{e}_r$ at point $\mathbf{r}$ can be written as $\mathbf{e}_r = \frac{\mathbf{r}}{|\mathbf{r}|}$. Since

$$\begin{aligned} \mathbf{R} \times d\mathbf{S}(\mathbf{r}') \cdot \mathbf{e}_r &= dS\mathbf{R} \times \mathbf{n}(\mathbf{r}') \cdot \mathbf{e}_r && (3.2.17) \\ &= dS(\mathbf{r} - \mathbf{r}') \times \frac{\mathbf{r}'}{|\mathbf{r}'|} \cdot \frac{\mathbf{r}}{|\mathbf{r}|} && (3.2.18) \\ &= 0, && (3.2.19) \end{aligned}$$

where the direction $\mathbf{n}(r')$ of a boundary surface element $d\mathbf{S}$ at point $\mathbf{r}'$ is $\mathbf{n}(r') = \frac{\mathbf{r}'}{|\mathbf{r}'|}$, the contribution of volume currents towards extracranial radial magnetic fields is given by

$$\begin{aligned} B_r^v &= \frac{\mu_0}{4\pi}\Delta\sigma \int V(\mathbf{r}')\frac{\mathbf{R}}{R^3} \times d\mathbf{S} \cdot \mathbf{e}_r && (3.2.20) \\ &= 0, && (3.2.21) \end{aligned}$$

illustrating the main advantage of this model for excluding volume currents from analysis. The radial magnetic field is entirely due to the presence of primary currents and is given by

$$\begin{aligned} B_r &= \frac{\mu_0}{4\pi} \int \mathbf{J}^p(\mathbf{r}) \times \frac{\mathbf{R}}{R^3 \cdot \mathbf{e}_r dv'} && (3.2.22) \\ &= -\frac{\mu_0 \mathbf{Q} \times (\mathbf{r} - \mathbf{r}_Q) \cdot \mathbf{e}_r}{4\pi |\mathbf{r} - \mathbf{r}_Q|^3}, && (3.2.23) \end{aligned}$$

where $\mathbf{r}_Q$ is the position of the current dipole $\mathbf{Q}$. Any current dipole $\mathbf{Q}$ can be decomposed into radial $\mathbf{Q}_r$ and tangential $\mathbf{Q}_t$ components. Since the radial component results in a zero contribution to the extracranial radial magnetic field, only the tangential component needs to be taken into consideration. Consequently, neuronal activities only producing radial currents cannot be detected based on the spherically symmetric conductor model. Fortunately, most cortex functional areas are located in fissures, providing tangential primary currents for detection. However, an infinite number of possible primary current configurations are possible for a given radial field measurement due to the possible arbitrary orientation of primary currents, implying insufficient knowledge of the current dipole amplitude.

In spite of the simple form of the radial component of the magnetic field, the tangential component is still influenced by the volume currents. The calculation of the total magnetic field can be obtained from the magnetic scalar potential U

defined as $\mathbf{B} = -\mu_0 \nabla U$ due to the fact that no current is present outside of the brain $\nabla \times \mathbf{B} = 0$. Based on these conditions, the total magnetic field outside of the sphere is given by [29, 37]

$$\mathbf{B}(\mathbf{r}) = \frac{\mu_0}{4\pi F^2}(F\mathbf{Q} \times \mathbf{r}_Q - \mathbf{Q} \times \mathbf{r}_Q \cdot \mathbf{r}\nabla F) \tag{3.2.24}$$

where

$$F = a(ra + r^2 - \mathbf{r}_0 \cdot \mathbf{r}), \tag{3.2.25}$$

and

$$\nabla F = (r^{-1}a^2 + a^{-1}\mathbf{a} \cdot \mathbf{r} + 2a + 2r)\mathbf{r} - (a + 2r + a^{-1}\mathbf{a} \cdot \mathbf{r})\mathbf{r}_0, \tag{3.2.26}$$

with $\mathbf{a} = \mathbf{r} - \mathbf{r}_Q$, $a = |\mathbf{a}|$, and $r = |\mathbf{r}|$. This shows that even though the tangential field component is affected by volume currents, it can be computed without the knowledge of the conductivity profile $\sigma(\mathbf{r})$.

The electric scalar potential V on the surface of a spherically symmetric conductor is affected by the conductivity profile. In the case of the human head, the potential V is more attenuated and widespread at the scalp than a spherical uniform conductor, due to the presence of a poorly conductive skull layer between the highly conductive brain and scalp layers. However, both radial and deep sources contribute significantly to the potential V, in spite of its complex computation. [30, 31]

The horizontally layered conductor model (Fig 3.12) assumes that the current dipoles are embedded in a large conductor with a conductivity profile distributed horizontally in the half space of $z < 0$. The vertical component of the induced magnetic field can be easily derived by extending the spherically symmetric conductor model to the infinite radius limit. The vertical component of magnetic field in the space of $z > 0$ due to a current dipole $\mathbf{Q}$ is given by

$$B_z = \frac{\mu_0 \mathbf{Q} \times \mathbf{R} \cdot \mathbf{e}_z}{4\pi R^3}, \tag{3.2.27}$$

where $\mathbf{R}$ is the spatial separation between the current dipole $\mathbf{Q}$ and the measuring site with $R = |\mathbf{R}|$, and $\mathbf{e}_z$ is the unit vector of z direction. It is obvious that the horizontally layered conductor model follows all the conclusions derived from the spherically symmetric conductor model.

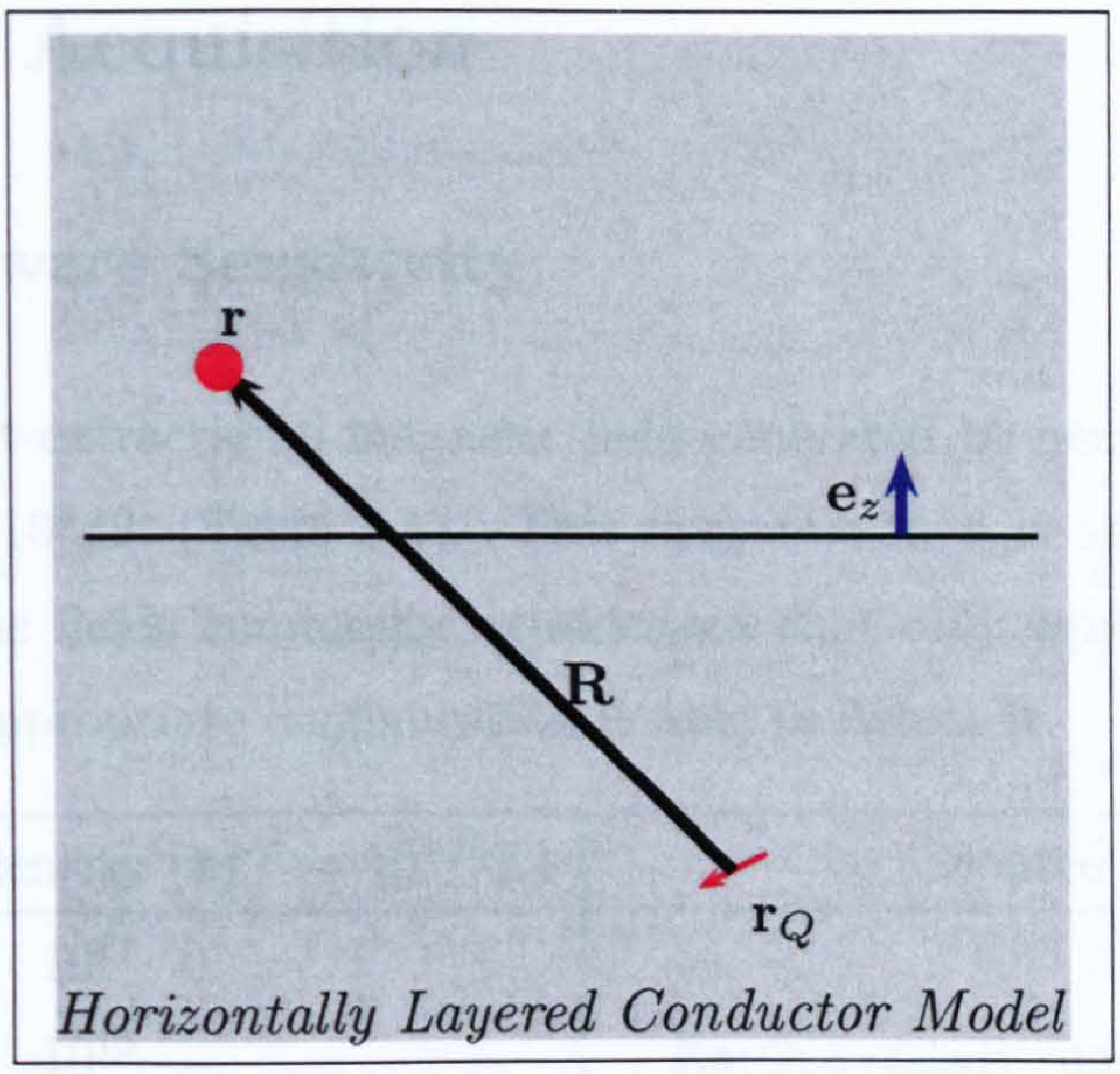

Figure 3.12: The coordinate system adopted in this section to demonstrate the horizontally layered conductor model.

If the homogenous conductor pieces are arbitrarily shaped, the magnetic field **B** must be calculated numerically based on the realistically shaped conductor model. The boundary element method is the dominant tool in analyzing the realistically shaped conductor model, in which each boundary surface between different conductivities is tessellated into a suitable number of triangles [26–28]. By assuming that the potential is constant on each triangle, the electric potential profile in the space can be calculated out. Subsequently the magnetic field can be derived from the knowledge of electric potential. The number of triangles has to be reasonably large to provide a sufficiently accurate description of the geometry and representation of the potential at high spatial resolution.

The complications of numerical methods in modelling the human brain have been reported, where excessive errors may be present in the electric potential due to the poor conductivity of skull compared to brain and scalp. [19] However, it has been shown that the currents in the skull and on the scalp contribute negligibly to the magnetic field, suggesting that a brain-shaped homogeneous conductor head model is sufficient for MEG in practice. [21]

3.3 Data Acquisition

3.3.1 Hardware Sensitivity

The strongest extracranial magnetic field generated by neuronal activities is on the order of $10^3 fT$ (Table 3.1). This magnetic field is so small compared to other magnetic fields commonly experienced that only equipment with high sensitivity and appropriate configuration is able to detect it.

Magnetic flux density ($1fT = 10^{-15}T$)	Source
10^{11}	
10^{10}	Earth's steady magnetic field
10^9	
10^8	urban noise
10^7	
10^6	magnetized lung contaminants
10^5	abdominal currents
10^4	cardiogram, oculogram
10^3	epileptic and spontaneous activity
10^2	cortical evoked activity
10	SQUID noise
1	brainstem evoked activity

Table 3.1: Comparison of characteristic magnetic field strength generated by different sources.

The change of magnetic field is the primary signal sensed by the detector. An induction loop is employed, so that an induced current in the loop is coupled with the change in magnetic field. The strength of the current corresponds to the net change in magnetic flux and the magnetic field perpendicular to the induction loop.

Apart from intrinsic sensitivity, the capability of the sensor also depends on the size of the loop, since the magnetic flux is proportional to the loop size. The basic means of extending the loop surface is by increasing the number of turns of the pickup coil, with the amplification proportional to the number of turns. However, the increased inductance coupled with large number of turns reduces the sensitivity of the device. Although at room temperature a multimillion turn coil is feasible to use to detect extracranial magnetic field [51], it suffers from its bulky physical size and low sensitivity, which makes it clinically impractical.

The development of low temperature and superconductor technology enables the use of induction loops with high intrinsic sensitivity. Maintained at superconducting state in a liquid helium bath, the superconducting coil provides signal detection with low intrinsic thermal noise and power dispersion. These characteristics allow fast and significant responses to small changes in magnetic flux.

The output signal from the pickup coil is not sufficiently large to be read out by electronics, where further amplification is needed. Conventional amplifiers possess large intrinsic noise, which sacrifices the signal sensitivity gained by the pickup coil and impairs the overall performance of the system. The invention of *superconducting quantum interference device* (SQUID) [74] provides a powerful detection method for weak magnetic fields [57]. Based on its extreme sensitivity at the critical condition and low intrinsic noise, the SQUID acts as an high gain current to voltage converter. The SQUID (Fig 3.13) is composed of a superconducting ring interrupted by nonsuperconducting materials forming Josephson junctions [63]. The interrupted ring still acts as a superconductor with currents smaller than a critical level, where electrons are able to cross the resistive segment without losing energy following the tunnel effect. However, excessive currents above the threshold transforms the ring into a nonsuperconducting state, causing fast dissipation of current and a voltage drop across the Josephson junction. The connection between the pickup coil and the SQUID takes the form of the pickup loop wiring around the ring, so that the currents due to the change in magnetic flux is directly fed into the SQUID. The SQUID is maintained at the critical condition at the rest state, while the current in the induction loop results in a change in the magnetic field inside SQUID, inducing a change in currents flowing in the ring. The increased current transforms the ring into nonsuperconducting state, causing a corresponding voltage output at the Josephson junction.

Following the advances in thin film fabricating techniques, the DC biased

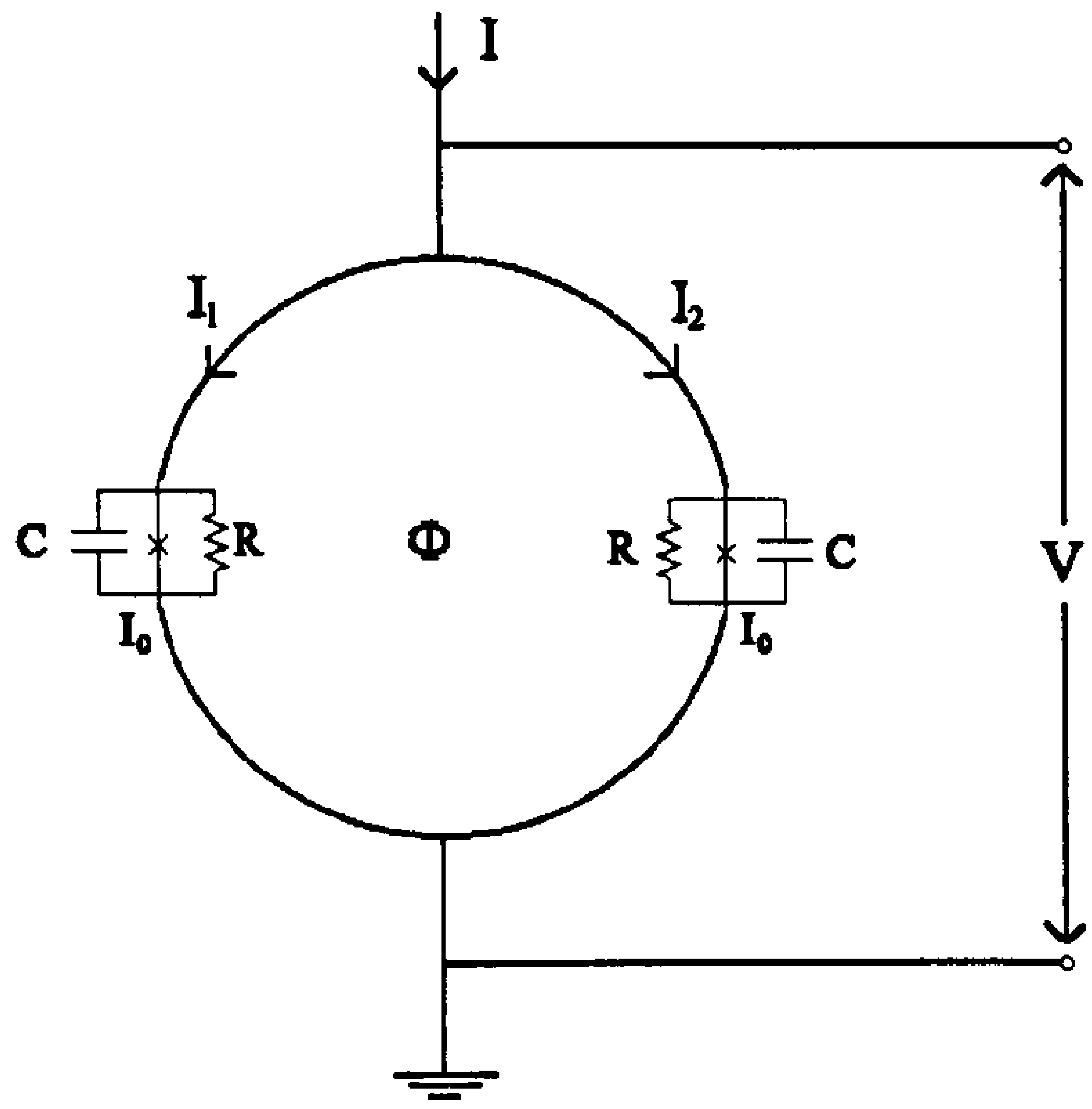

Figure 3.13: A schematic diagram of the SQUID.

SQUID [101] has secured its position in weak magnetic field detection. A DC biased SQUID contains two identical Josephson junctions instead of a traditional single interruption on the superconducting ring. The superconducting ring is connected directly with external control electronics. The currents inside the ring are driven at the critical level by the application of a small DC current from the control electronics. The voltage drop across the Josephson junctions due to excessive current is measured in the control electronics as the output signal.

Since the magnetic field generated by a current dipole drops rapidly with the distance, a close distance between the sensor and the neuronal activity source can significantly improve the sensitivity of the experiment. However, the SQUID can only work below a superconductivity threshold temperature, often maintained by liquid helium. Vapour-cooled coil-foil shield [102], a special design of thermal insulation, is employed to allow low thermal noise and close vicinity between sensors and the subject. Coil-foil is a foil formed by thin insulated wires glued together, so that electrical and thermal conductivities are only conducted along the direction of the wire only. The noise current can thus be greatly restricted. The thermal insulation is achieved by using vacuum space and thin plastics with aluminium film evaporated on one side to reduce radiation.

3.3.2 Noise Suppression

The other means of increasing the detectability of the extracranial magnetic field generated by neuronal activities is via noise suppression. Due to the susceptibility of MEG to noise, this issue has been well explored since the birth of MEG and has resulted in many solutions and concerns.

The immediate strategy of noise suppression is the employment of a magnetically shielded room. The common construction of shielding is based on one or a combination of ferromagnetic, eddy-current and active shielding. Ferromagnetic shielding relies on high permeability materials, which enables the unwanted magnetic field to be trapped in the shielding layer. Eddy-current shielding is based on high conductivity materials generating eddy-currents in reaction to a change in magnetic fields, and consequently counterbalancing the change in magnetic field. In contrast to these passive techniques, active shielding employs field sensors to feed currents to compensation coils according to the strength of environmental noise. The ferromagnetic shielding is mostly effective for low frequency noise attenuation, while the eddy-current shielding has its best performance at high frequency. Active shielding is not very often used due to the insignificance of its contribution towards noise attenuation. The common shielding room design typically results in a shielding factor of $50 - 100dB$, where low frequency noise of $1 - 10Hz$ is likely to have lower attenuation. Although the amplitude of environmental noise is likely to be greatly reduced, the post-shielding noise is still higher or comparable to the field induced by brain activities.

Apart from the residual environmental noise, physiological noise presents a significant problem. The source of the magnetic field can be modelled as an aggregation of current dipoles distributed in a pattern. The primary magnetic field induced by a current dipole is given by

$$\mathbf{B}^p = \frac{\mu_0}{4\pi}\mathbf{Q} \times \frac{\mathbf{R}}{R^3}, \tag{3.3.1}$$

where $\mathbf{Q}$ is the current dipole, $\mathbf{R}$ is the relative position between the dipole and the sensor. It is obvious that the strength of the magnetic field at the sensor induced by dipoles decreases rapidly with the distance between them. During MEG experiment, brain activity is spatially much closer to the sensors, and the application of gradiometers can further bias the signals based on their spatial locations. A gradiometer (Fig 3.14) is a type of pick-up coil typically consisting of two coils spatially separated and connected in opposite directions. An axial gradiometer has two coaxial coils with the separation along the axis, while a planar gradiometer is composed of two coaxial half turn coils connected in opposite direction with no axial separation. Mathematically, the application of gradiometer is equivalent to the gradient operation on the magnetic flux, which leads to a higher spatial bias and subsequently reduces the impact of external noise. Physically, the magnetic fields generated by distant noise sources presenting a more uniform pattern are likely to be picked up evenly by both coils and cancelled out, while nearby brain activities can induce different reactions between two coils and subsequently be detected. Complex and higher order gradiometers are also available by varying the connection configurations. The function of a gradiometer is purely based on spatial bias, so the impact of nearby noise cannot be attenuated by gradiometer, and the sensitivity towards deeper sources is restricted. The construction of a gradiometer also suffers from the imbalance between two coils due to inevitable imperfect manufacturing. Despite all these problems and limitations, gradiometers have obvious advantages over simple magnetometers constructed from single pick-up coil, since the noise reduction is the dominant issue in performing a successful MEG experiment.

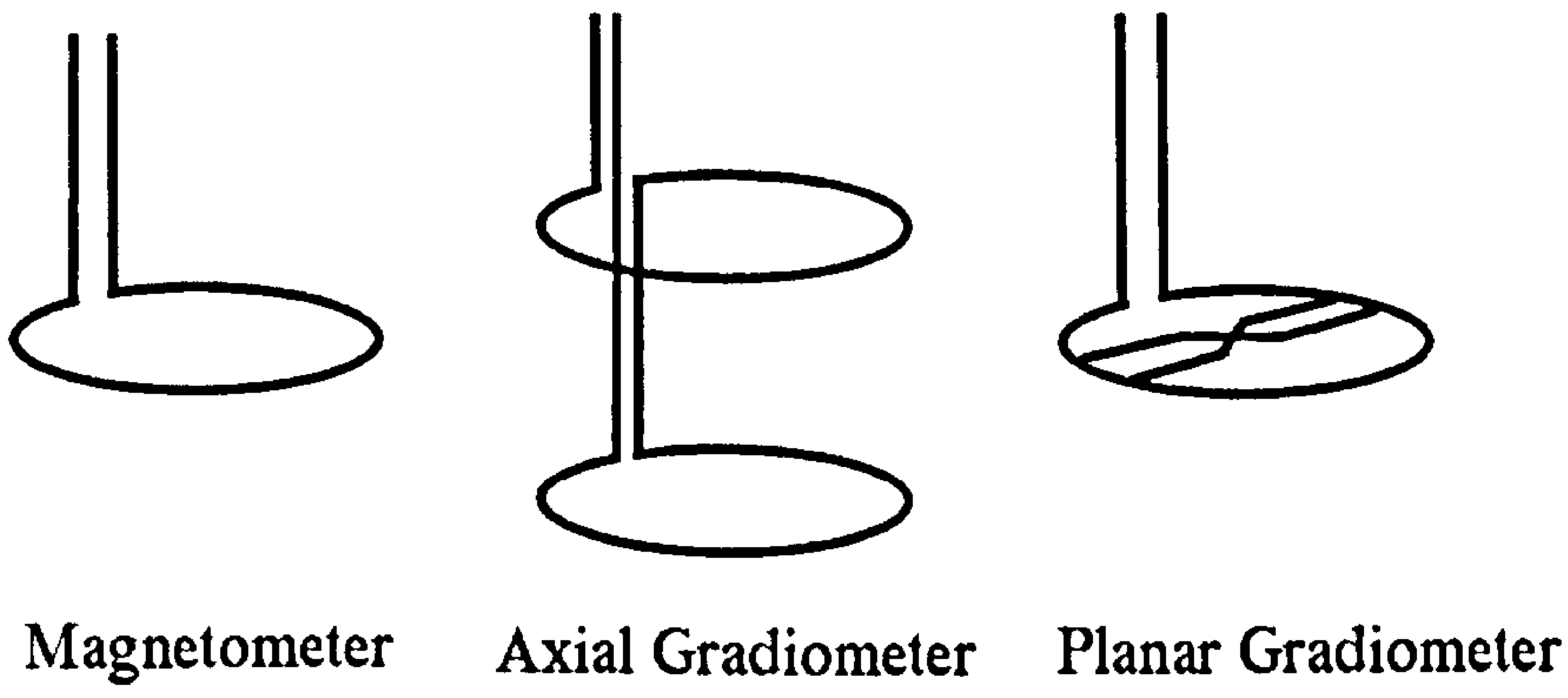

Figure 3.14: A diagram illustrating the construction of magnetometer, axial gradiometer and planar gradiometer.

Further developing the idea of gradiometers, electronic noise cancellation is introduced, in which reference sensors are employed to detect magnetic field and its gradients along three orthogonal directions. The reference channels are positioned far away from the subject, so that they are only sensitive to distant noise. The corrected outputs from the sensors are the linear combination of the sensor signal and reference channels. The linear weights of different channels are determined by characteristic of the noise field, and can be estimated through an adaptive statistical algorithm. Following the same logic, effective high order gradiometer can be formed electronically based on multiple sensors, as the final output can be viewed as the mathematical subtraction between the detection on two sites. Compared to the conventional gradiometer, the noise of an effective gradiometer is higher, since the two independent outputs increase the noise level.

Apart from attenuating noise, reducing the chance of introduction of noise is also crucial. Sufficient shielding of any leads in the experimental area, and proper grounding of electronic equipment within the measurement range is the key to prevent unnecessary noise and stimulus synchronized artifacts.

3.4 Data Analysis

3.4.1 Inverse Problem

The inverse problem is the reverse of the forward problem, in which the neuronal activity current sources are to be located based on a measured distribution of the magnetic field. However, it has been shown that a current distribution cannot be retrieved solely from the knowledge of the extracranial electromagnetic field. [18]

A radial dipole configuration in a spherically symmetric conductor is magnetically silent, $\mathbf{B} = 0$, but produces an electric field, while a current loop is electrically silent, $\mathbf{E} = 0$, but produces a magnetic field. It can be proven that primary currents $\mathbf{J}^p$, of constant amplitude over a closed surface S inside a homogenous subregion with its direction normal to the surface, produce no electromagnetic field, $\mathbf{E} = \mathbf{B} = 0$, outside of the head. This also implies that although a combination of MEG and EEG detection can be useful for revealing primary currents, the possibility of silent primary current cannot be eliminated.

As well as silent sources, limited sampling sites providing partial information of the field distribution in the space poses another challenge to the inverse problem. With a small array MEG system, the detector is moved around the subject's head to gather a more complete map of the field distribution over the cortex. However, this procedure leads to a lengthy experiment, according to the number of sites acquired and the repetitions needed to gain sufficient *signal to noise ratio* (SNR) . Although the availability of whole cortex multi-channel MEG system has shortened the studies significantly, the spatial resolution of the field map still remains at centimetre level.

The inverse problem is certainly affected by the head model used and the field component measured. It was shown that the sphere model provides good results, given that the sphere model is fitted to the local radius of curvature in the area of interest. [9] The radial magnetic field can be directly calculated for a spherically symmetric conductor from primary currents with Biot-Savart law and the tangential field components calculated analytically without reference to the conductivity profile. Based on no influence of volume currents on radial field components, it was proposed that the radial magnetic field should be preferred in practical measurements. [10] However, it is also shown that distortions due to nonidealities in the conductor shape are present in all three components of the magnetic field. [21] In reality, deviations from the perfect head model are inevitable, which certainly impacts on the inverse problem.

All these issues can be categorized as imperfect practice or intrinsic inadequacy of the forward problem. Instead of an equation of certainty, the forward problem is transformed into a statistical probability density function. The probability is a conditional probability $\theta(\mathbf{b}|\mathbf{x})$, denoting the probability of attaining a certain noise free field map $\mathbf{b}$ under the condition of a known primary source distribution $\mathbf{x}$.

Since the solution is nonunique, constraints and assumptions on source configurations are necessary to limit the possible solutions to the inverse problem. The primary constraint is often the number of sources, while the increased number of sources is coupled with an increased instability of the solution. Further constraints such as the location and the orientation of current dipoles can also be used. The location constraint is usually derived from other functional modalities with good spatial localization capability such as fMRI, while the orientation constraint is generally acquired from analyzing cortical folding patterns according to the anatomical images. With a higher level of constraints used, the inverse problem is more likely to be solved and the solution more likely to be stable. However, excessive constraints also impose a risk of misleading the analysis procedures and causing incorrect solutions. This *a priori* knowledge can be mathematically expressed as the prior distribution $\rho_x(\mathbf{x})$.

The detected signal is generated not only by the brain activities, but also by the noise. A stable noise has a certain distribution $\nu(\mathbf{b}_{obs}|\mathbf{b})$, indicating the probability of observing a field map $\mathbf{b}_{obs}$ with the actual field distribution as $\mathbf{b}$.

Based on the above analysis, the posterior distribution $\phi_x(\mathbf{x})$ can be used to reflect the detected source distribution under the impact of disturbing sources. The relationship between prior and posterior distribution density functions is given by

$$\phi_x(\mathbf{x}) = C_0\rho_x(\mathbf{x})\int \nu(\mathbf{b}_{obs}|\mathbf{b})\,\theta(\mathbf{b}|\mathbf{x})\,d\mathbf{b}, \tag{3.4.1}$$

where C_0 is the normalization constant. Under the assumption of independent noise or linear model, the observed field map $\mathbf{b}_{obs}$ can be written as $\mathbf{b}_{obs} = \mathbf{b} + \epsilon_b$, where ϵ_b is the noise. Subsequently, the distribution of the noisy signal $\nu(\mathbf{b}_{obs}|\mathbf{b})$ is equivalent to the distribution of the noise $f_b(\epsilon_b) = f_b(\mathbf{b}_{obs} - \mathbf{b})$. Further approximation of an accurate description $\mathbf{b} = g(\mathbf{x})$ of the forward problem, results in the forward problem distribution of Dirac delta function as $\theta(\mathbf{b}|\mathbf{x}) = \delta(\mathbf{b} - g(\mathbf{x}))$. The posterior distribution therefore takes the form of

$$\phi_x(\mathbf{x}) = C_0\rho_x(\mathbf{x})\,f_b(\mathbf{b}_{obs} - g(\mathbf{x})). \tag{3.4.2}$$

Under the assumption of a constant prior distribution in a confined region and the Gaussian distribution of noise, the maximum likelihood estimate can be achieved by least squares search. Based on the current dipole model, the result of the maximum likelihood estimate is termed the *equivalent current dipole* (ECD).

3.4.2 Lead Field and its Application

The reaction of a medium to an external electromagnetic field is generally indicated by its conductivity and receptivity, implying a linear relationship between medium response and external fields. Since individual field sources can invoke independent medium reactions, the total reaction of the medium is the linear summation of them. Based on this superposition theorem, the field sources can be treated separately, while the field generation can be viewed as a single operation. Therefore, the measured electric **E** and magnetic **B** fields are the linear transformation of primary currents $\mathbf{J}^p$. Consequently, a linear transformation vector function $\mathrm{L}_i(\mathbf{r})$ of the whole space can be found for a detector i whose output is ξ_i. Consequently the lead field $\mathrm{L}_i(\mathbf{r})$ can be defined as

$$\xi_i = \int \mathrm{L}_i(\mathbf{r}) \cdot \mathbf{J}^p(\mathbf{r}) dv, \tag{3.4.3}$$

describing the sensitivity distribution of the ith detector. [6, 16] The lead field $\mathrm{L}_i(\mathbf{r})$ depends on the conductivity profile $\sigma(\mathbf{r})$, the configuration of the detector and the electromagnetic property being measured.

In the case of magnetic lead field (Fig 3.15), the lead field for $\mathbf{r}'$ can be obtained by computing the magnetic field $\mathbf{B} = \mathbf{B}(\mathbf{Q}, \mathbf{r}')$ induced by current dipole $\mathbf{Q}$ at position $\mathbf{r}_Q$. Since the current dipole is defined such that $\mathbf{J}^p = \mathbf{Q}\delta(\mathbf{r} - \mathbf{r}_Q)$, the definition of lead field can be written as

$$\mathbf{B}_i(\mathbf{Q}, \mathbf{r}_Q) = \mathrm{L}_i(\mathbf{r}_Q) \cdot \mathbf{Q}, \tag{3.4.4}$$

where $\mathrm{L}_i(\mathbf{r})$ is the vector form of the lead field with three components corresponding to one $\mathbf{r}$ to derive the total field output at the ith detector. For the ith detector consisting of m planar coils, the output of the detector can be written as

$$\mathbf{B}_i(\mathbf{Q}, \mathbf{r}_Q) = \Sigma_{j=1}^{m} \int_{\mathbf{S}_j} \mathbf{B}(\mathbf{Q}, \mathbf{r}_Q) \cdot d\mathbf{S}_j, \tag{3.4.5}$$

where $\mathbf{S}_j$ is the area of coil j with its direction meeting the coil winding.

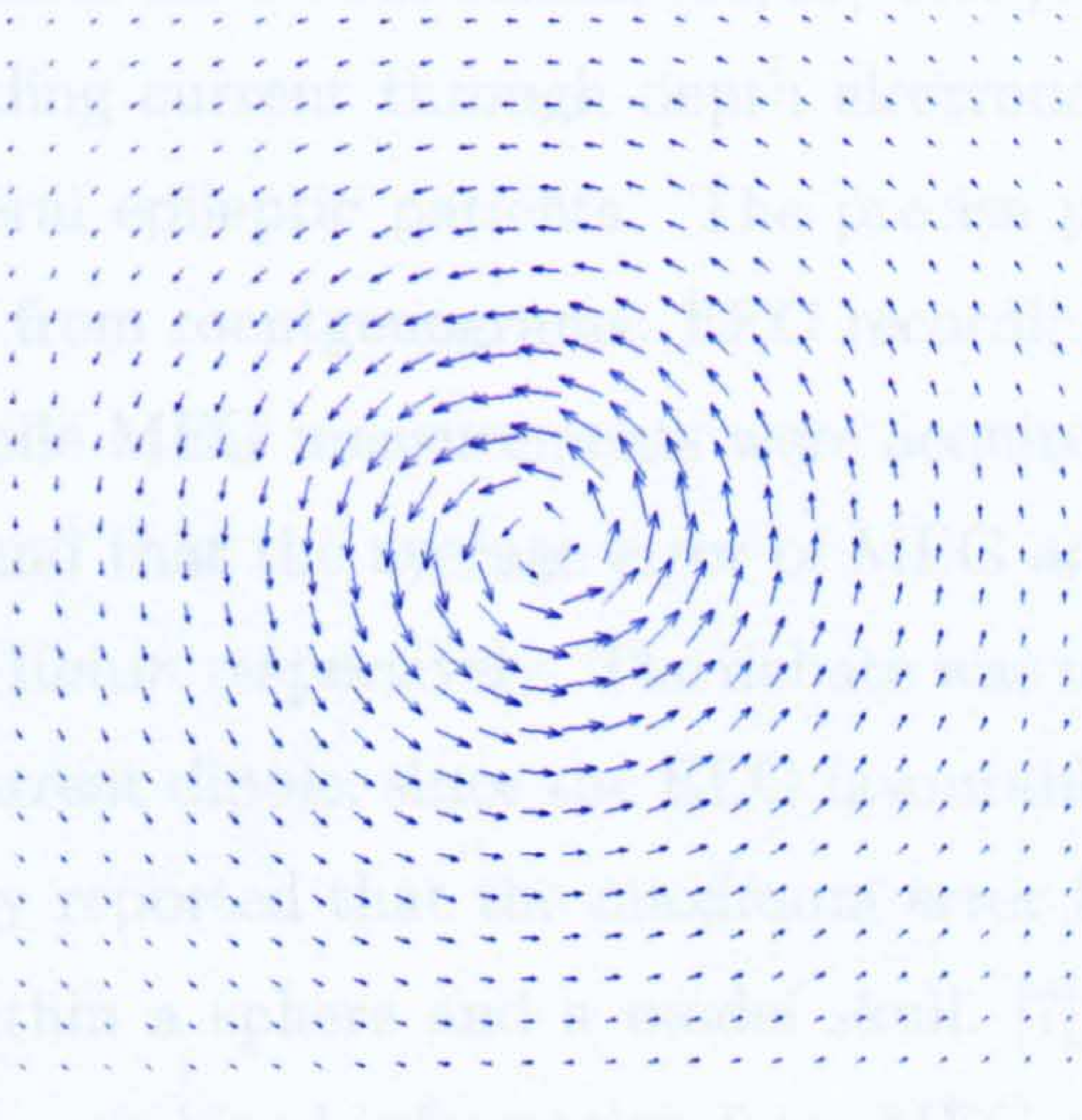

Figure 3.15: A simulation demonstrating the magnetic lead field of a magnetometer located directly above the centre of the plane with its sensitive axis perpendicular to the plane.

Since MEG and EEG project the primary current distribution on the respective lead fields, both techniques fundamentally measure the weighted integral of the primary current distribution. Although standing on the same ground, MEG and EEG have several different properties. Given the different lead fields based on the spherically symmetric conductor model, MEG is only sensitive to the tangential components of primary currents, while EEG senses all primary currents. In addition, MEG is much less sensitive to deep sources compared to EEG due to fast attenuation of the lead field with source depth. However, the electric lead field is more sensitive to conductivity profile than magnetic lead field, especially with the presence of skull and scalp. The concentric inhomogeneities do not affect the magnetic lead field but influence the electric field in the spherically symmetric conductor model. The absolute accuracy of MEG and EEG is still under investigation with controversial conclusions. The studies based on artificial introduction of primary currents show that MEG is only marginally more accurate than EEG in locating cerebral electrical activity [11], while conventionally it is believed that MEG provides a significantly better spatial resolution than EEG [14,15]. Debates on methodological grounds have been raised. [12,13] The primary current dipole was introduced by feeding current through depth electrodes invasively inserted into the brains of several epileptic patients. The precise position of each electrodes was determined from roentgenograms. EEG recording was measured with 16 scalp electrodes, while MEG measurements were acquired at 16 sites outside of the head. It was found that the average error of MEG and EEG source localization were $8mm$ and $10mm$ respectively. The debate was mainly focused on the characteristic of the current dipole, since the EEG favourable radial sources were used. It was previously reported that the maximum error for MEG localization is $3mm$ for dipoles within a sphere and a model skull. [7] Due to the complementary lead fields, the combined information from MEG and EEG can provide more complete view of neuronal activity. However, it is also the difference in lead fields that make it impossible to determine the superiority of either techniques in absolute sense.

3.4.3 Dipole Fitting

Based on the simple model of *equivalent current dipoles* (ECDs), the inverse problem is reduced to decoding the dipolar field patterns. In a conventional MEG configuration, the radial components of the magnetic field are measured based on a spherically symmetric head model, implying that only tangential components of current dipoles can be detected. A dipolar field map on a plane parallel to the source is composed of two maxima of opposite signs. The source dipole lies beneath the midpoint of field maxima and is perpendicular to the plane passing through maxima and the centre of the sphere. The field map (Fig 3.16) is simply given by

$$B_r = -\frac{\mu_0 \mathbf{Q} \times (\mathbf{r} - \mathbf{r}_Q) \cdot \mathbf{e}_r}{4\pi |\mathbf{r} - \mathbf{r}_Q|^3}, \tag{3.4.6}$$

where $\mathbf{r}_Q$ is the position of the source current dipole $\mathbf{Q}$, $\mathbf{e}_r$ is the unit radial vector, and $\mathbf{r}$ is the detector position. The position of the maxima can be calculated by pursuing the zero point of the derivative of the field map. Subsequently the depth of the source dipole d is related to the separation Δ between maxima by $d = \frac{\Delta}{\sqrt{2}}$. The orientation and position of the dipole can be therefore determined, while its amplitude can be attained from field map fitting.

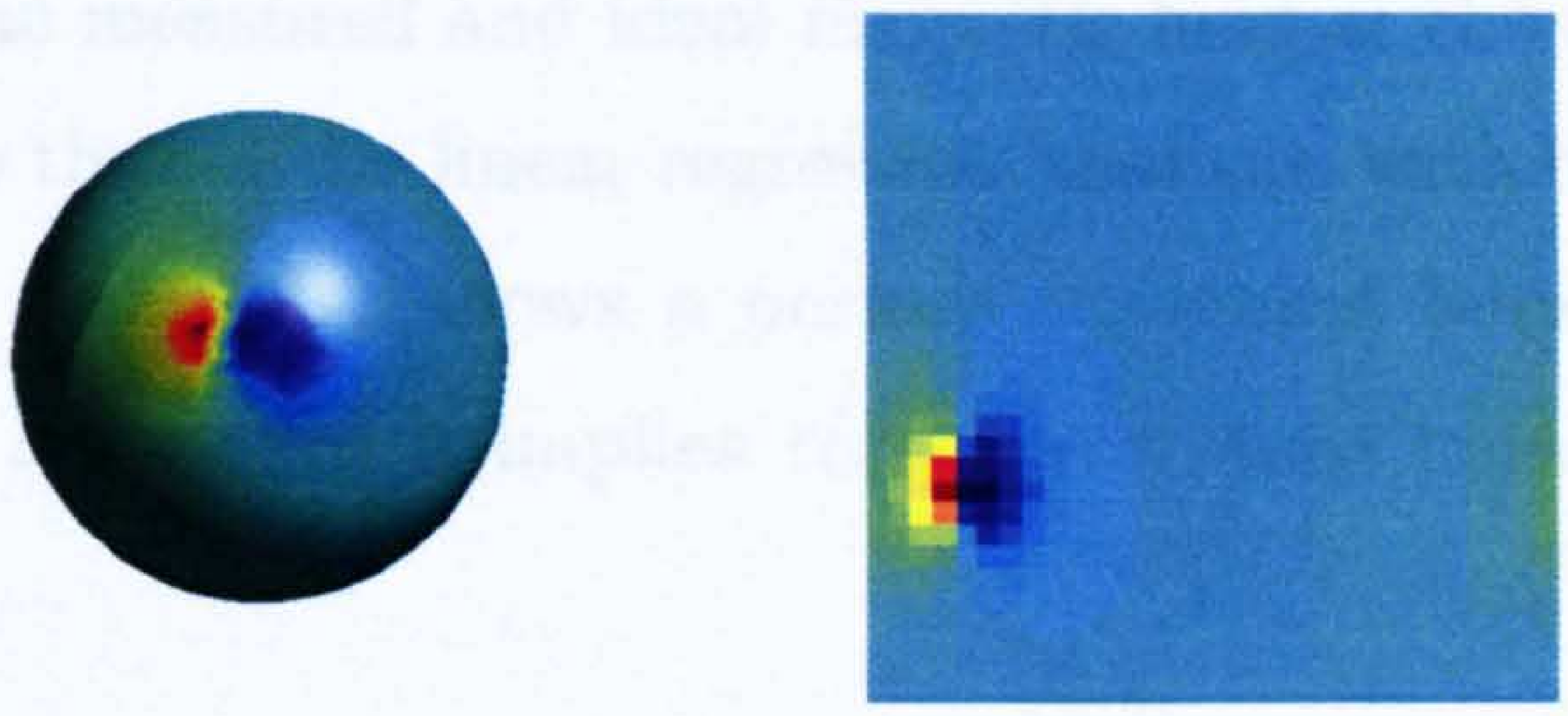

Figure 3.16: A simulation of radial magnetic field component based on spherically symmetric conductor model.

With several sources present during the measurement, the field map is the linear summation of the contribution from all the dipoles. Since the dipolar field strength drops rapidly with distance, sources distributed far away from each other can still be determined by analyzing each dipolar pattern separately. In reality, dipolar patterns are often merged together or embedded in the background brain activities, a least square fitting procedure is generally used to acquire the best possible results.

The details of dipole configurations are derived from an instant field map. Subsequently the dipole configuration time course can be derived by determining the configuration at each time point, while the temporal correlations between time points are ignored.

The solution quality of the inverse problem depends on the level of noise and the sufficiency of the model. An indication of the deviation of the model from actual brain activity is the *goodness-of-fit* (GOF) given by

$$g = 1 - \frac{\sum_{i=1}^{n} \left(b_i - \hat{b}_i\right)^2}{\sum_{i=1}^{n} b_i^2}, \tag{3.4.7}$$

where b_i and $\hat{b}_i$ are the measured and ideal magnetic field at the detector i. This indicator is similar to that of the linear regression analysis, with its value varying between 0 and 1. A score of 1 shows a perfect agreement between model and measurement, while a score of 0 implies total irrelevance between model and measurement.

The noise level σ_i of each channel i can be estimated via several approaches, where the simplest method is estimating the standard error. Subsequently the χ^2 value of the observation is given by

$$\chi^2_{obs} = \sum_{i=1}^{n} \frac{\left(b_i - \hat{b}_i\right)^2}{\sigma_i^2}. \tag{3.4.8}$$

Based on Gaussian errors in the measurement, the χ^2_{obs} is distributed as χ^2_{n-r}, where r is the number of model parameters. The probability $P_{obs} = P\left\{\chi^2_{n-r} < \chi^2_{obs}\right\}$ compares the residual field against noise level, and provides a quantitative measurement of the quality of the model. A high probability value indicates that the model is a good representation of the data, while a low value suggests the inadequacy of the model and the need of introducing more sources.

The stability of the model is marked by confidence limits, often determined by a Monte Carlo method. Since the sensitivity of MEG varies with depth, the confidence range is also not isotropic. However, the confidence limits of superficial current sources can be approximated linearly.

The results generated from the inverse problem can be aligned onto the anatomical images to allow the functional anatomy interpret and further allow the comparison against other modalities. [2–5]

Chapter 4

Instrumentation

4.1 fMRI Equipments

4.1.1 The Magnet

For this study a $3.0T$, $95cm$ diameter bore whole body magnet (Fig 4.1) made by Oxford Instruments was used, leading to proton precession at a Larmor frequency of $128MHz$. The magnetic field was generated by currents running in a superconducting coil, cooled by liquid helium, while liquid nitrogen was used to prevent fast vaporization of the helium. (Fig 4.2)

The homogeneity of the static field is given by δB, where δB is the deviation between the actual field and the required magnetic field B, and is written in terms of *parts per million* (ppm or 10^{-6}). A large index represents a high field inhomogeneity and often results in a poor quality image, depending on the acquisition sequence and thus it is important to minimize δB. This inhomogeneity is determined not only by the original design and implementation of the static field coil, but also the object present within the field. Generally, two approaches are used to enhance the homogeneity of the field, namely passive and active. The passive approach is to insert ferromagnetic materials into the magnetic field, which can adjust the magnetic field according to Maxwell's equations. The active approach is to install shimming coils into the magnetic field, which can generate compen-

Figure 4.1: The 3T MRI scanner for fMRI experiments.

sation fields. An initial fixed superconducting shimming set may be configured at the initialization of the magnet for crude field correction. A second interactive nonsuperconducting shimming set is used for fine shimming to compensate for time variable changes in the local field, for example due to the presence of objects to be scanned within the magnet bore. The shim coils are designed to produce fields of spherical harmonic patterns, whose configuration is usually determined by iteration and observation of the FID. [45] Auto shimming approaches are designed to decompose the field map acquired by the imaging sequence into the shim coil field patterns.

4.1.2 Transmitting and Receiving Equipment

Usually only one coil is used both for transmitting and receiving alternatively, one coil is used for transmitting and one for receiving. The transmitter circuit sends the rf coil high power rf pulses at the desired frequency and profile, while the receiver circuit amplifies the small signal detected by the rf coil. This implies in the event of only one coil being used that an inappropriate configuration of the rf coil impairs the performance on both transmitting and receiving sides. Both

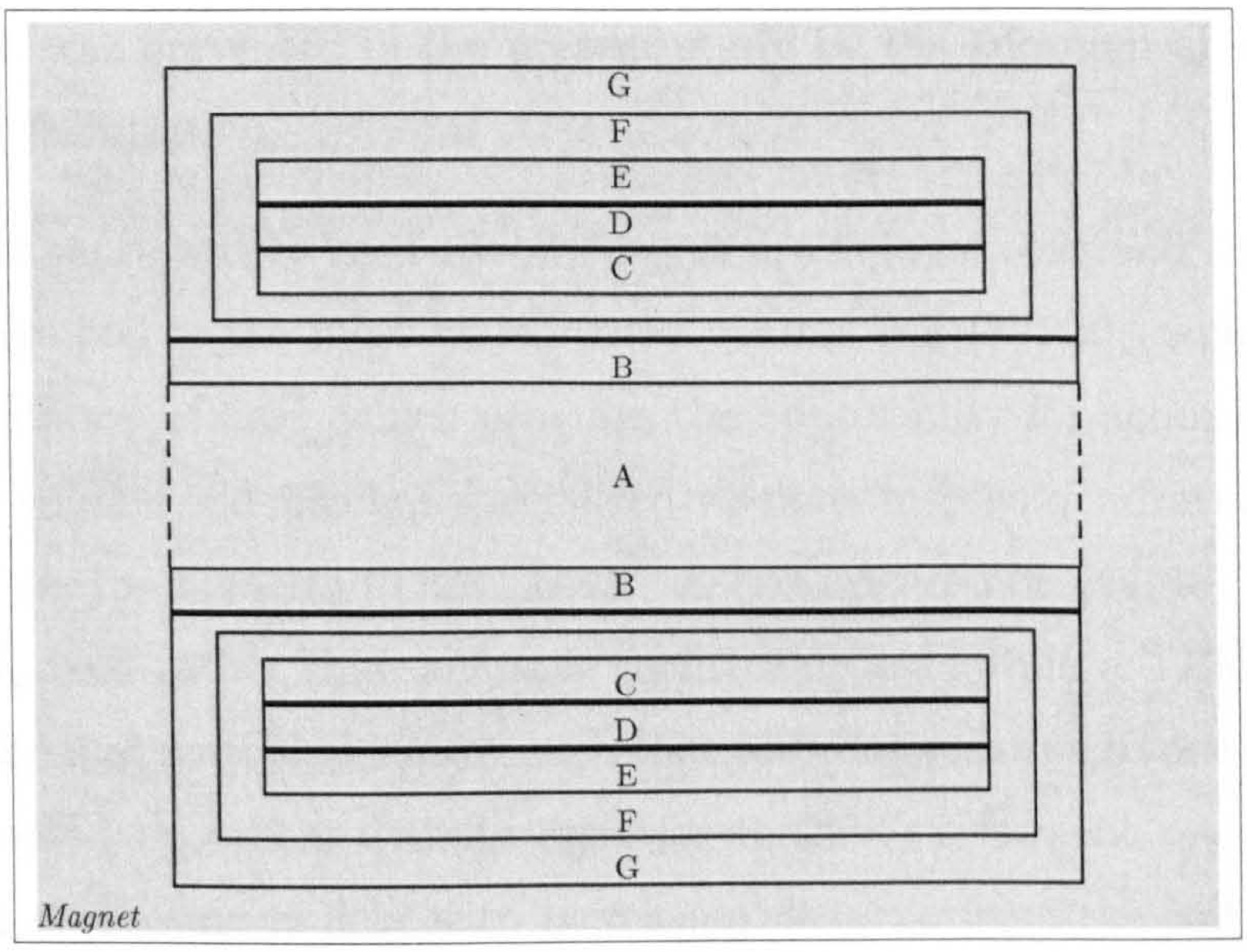

Figure 4.2: The cross section of a typical magnet, (A) Subject, (B) Former for the magnet (not available in this study), (C) Superconducting Wire, (D) Superconducting Shimming, (E) Helium Cryostat, (F) Nitrogen Cryostat, (G) Vacuum Space

the transmitting and receiving circuits were designed with the assumption of the rf coil transformed to an impedance of 50Ω at resonance. This design allows the full absorption of transmitter power by the rf coil without energy reflection, and a full propagation of signal within the receiver circuit. The rf coil was equipped with adjusting elements to change the amplitude and phase of the coil impedance, allowing tuning and matching to be carried out during different experiments, to compensate for changes in impedance due to coupling between the object and the coil. The tuning and matching procedure was usually achieved by analyzing the reflection coefficient curve or Smith Chart. [52]

Both the transmitter and receiver circuits must be of high stability. The flip angle is determined by the power provided by the transmitter circuit, leading to changes in the available transverse magnetization for detection and subsequently the intensity of the image. The image intensity also depends on the amplification of the receiver circuit.

Environmental rf interference such as radio stations can generate image artifacts, which was prevented in the present study by the adoption of appropriate rf shielding facilities.

The two most widely used rf coil designs are volume coils and surface coils. The birdcage coil is the most widely used volume coil [35, 49], capable of generating a uniform rf field, which provides the opportunity for acquiring a whole volume. A volume coil also has specialized versions such as quadrature coils and *transverse electromagnetic* (TEM) coils. A quadrature coil [44, 48] produces a rotating $\mathbf{B}_1$ field rather than a simple oscillation field, while a TEM coil has a broad tuning and matching feature such that the configuration of one experiment can be adopted by others without need for further adjustment. A surface coil produces a decreasing rf field with increasing distance from the coil, leading to higher sensitivity near the coil. The use of a surface coil provides a high signal to noise ratio within the region of interest, making it suitable for studies of known focal responses. Carefully decoupled TEM and surface coils can be used together to take advantage of both techniques. The coils used in this study were $9cm$ (Fig 4.4) and $14cm$ (Fig 4.5) diameter surface coils, a birdcage coil (Fig 4.3) of $26.5cm$ in diameter and $26.5cm$ in length and a TEM coil (Fig 4.6) of $26.5cm$ in diameter and $23cm$ in length.

4.1.3 Gradient System

Gradient coils are designed to be of low inductance L, generally smaller than $500\mu H$, to allow efficient switching. When using an EPI sequence in an fMRI study, the gradients and their circuits are organized into three groups, referred to as slice, broadening and switching. From the view of the subject during sagittal imaging, the slice gradient was along the left-right direction with the broadening gradient along the anterior-posterior direction, while the switching gradient was along the superior-inferior direction. The slice and broadening gradients were powered by 6 and 4 high power Techron 7700 series amplifiers respectively, while the switching gradient was powered by 8 amplifiers.

The efficiency of a gradient coil $\eta = \frac{G}{I}$ is defined as the magnetic field gradient G generated by unit current I. [61] The efficiencies of the slice and broadening

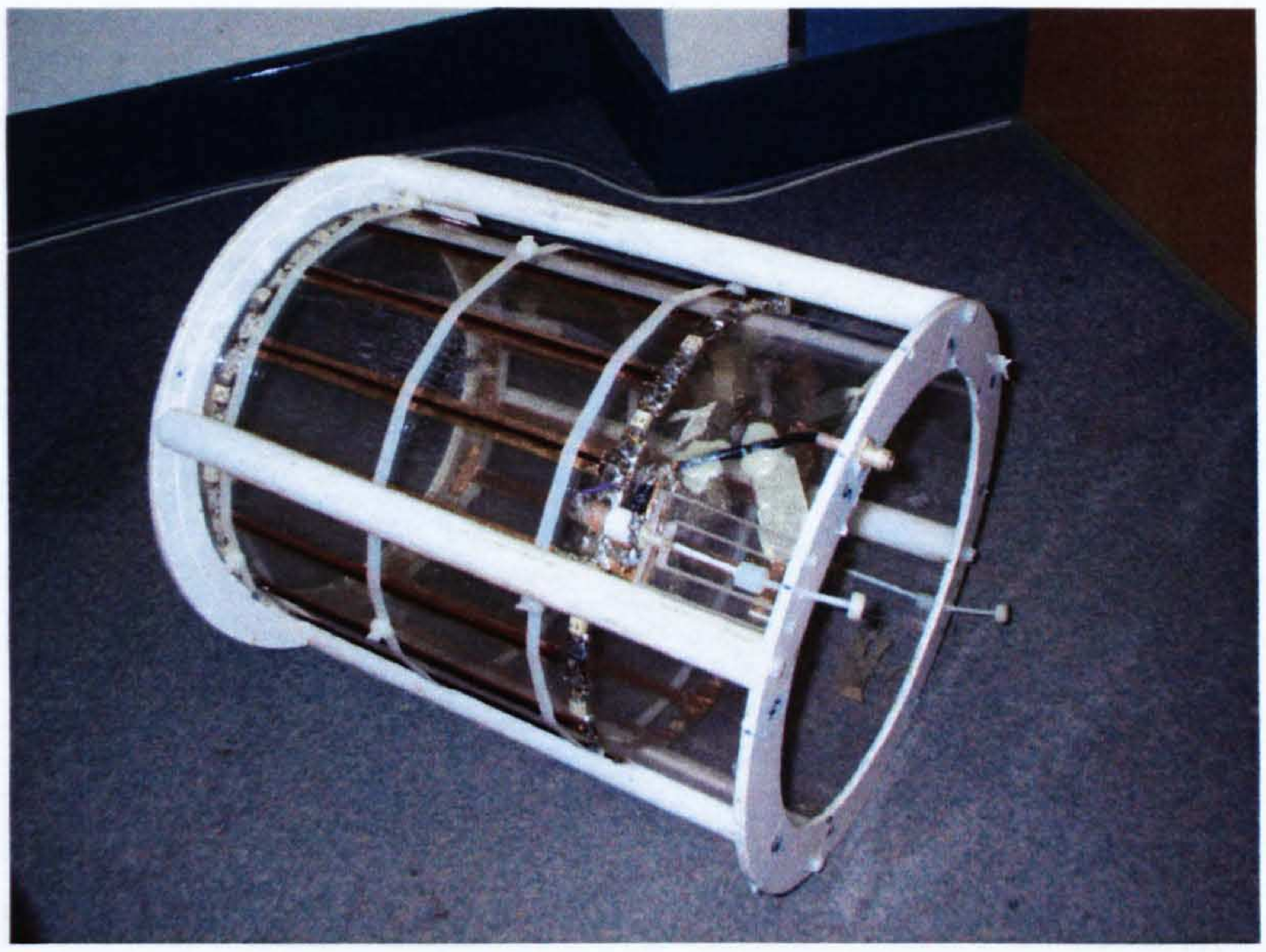

Figure 4.3: The quadrature birdcage coil, of 26.5 cm in diameter and length, used in this study.

Figure 4.4: The surface coil, of 9 cm in diameter, manufactured by *MR Instruments Inc.* used in conjunction with TEM coil in this study.

Figure 4.5: The home made surface coil, of 14 cm in diameter, used in this study and a phantom.

Figure 4.6: The TEM coil, of 26.5 cm in diameter and 23 cm in length, manufactured by *MR Instruments Inc.* used in this study.

gradient coils were $100mTm^{-1}kA^{-1}$ and $92mTm^{-1}kA^{-1}$ respectively, while the efficiency of the switching gradient was $336mTm^{-1}kA^{-1}$. The voltage across the gradient coil is given by $V = \frac{GL}{\eta\Delta}$, where Δ is the rise time indicating the response speed of the coil. [64] To prevent high power demand due to sharp rising or dropping of the current, a *sin* profile was used to replace the original step function design of the switching gradient. The switching gradient was driven by a LC resonant circuit whose frequency was determined by the connected capacitor. The switching frequency in this study was $1.9kHz$, which means that 128 lines of the reciprocal space could be sampled within $33.7ms$. The slice and broadening gradients did not use a resonant circuit, allowing sharp edge response.

Due to the *sin* profile of the switching gradient, the reciprocal space had to be sampled with a varying interval according to the strength of the gradient. The equipment used in this study can reach a sampling rate of $1MHz$ equivalent to $1\mu s$ per point. The minimal sampling interval was near this value, although the maximal sampling interval was well above it.

4.2 MEG Equipment

The MEG system used in this work was a 151-channel whole cortex OMEGA system manufactured by CTF Systems. (Fig 4.7) The sensors were uniformly distributed over the surface of the head in a closed packed hexagonal grid with one independent sensor per site. [46] Each sensor was a $2cm$ in diameter and $5cm$ baseline axial first order gradiometer connected to a low noise planar DC SQUID, with an average separation of $31mm$. The noise level of the sensors was typically 4 to $7fTHz^{-\frac{1}{2}}$ or approximately $1fTcm^{-1}Hz^{-\frac{1}{2}}$, where the noise amplitude was stronger at low frequencies. Ambient environmental magnetic noise can be reduced by synthetic higher order gradiometers and adaptive cancellation based on 29 reference channels. [47] The noise reduction algorithm was capable of reducing interference, independent of noise character and dewar orientation, by a factor of approximately 10^4. It was also possible to record EEG signals simultaneously with 32-64 low magnetic noise electrodes. Auxiliary channels consisted of 16 *analogue to digital* (AD) and 16 *digital to analogue* (DA) converters for monitoring and sending auxiliary signals. These channels were capable of functioning as ammeters or volmeters and had signal generator capabilities controlled by triggers.

Figure 4.7: The MEG system manufactured by *CTF Systems Inc.*, used in this study.

The detection system was cooled by liquid helium to maintain the working condition of the SQUIDs. The helium dewar was helmet shaped to fit the subject's head and maximize the detection coverage, with the sensors only a few millimeters away from the surface of the dewar. The rf shielding was integrated into the low magnetic noise dewar to contribute to the overall low system noise level.

All channels were measured simultaneously from a single master clock with *digital signal processing* (DSP) based circuitry. The sampling rate was from 0 to $4000Hz$ or even higher for a subset of channels, where each point was digitized to 32 bits. The dynamic range of the system was approximately $\pm 600nT$ and the least significant bit represented $0.3fT$, with linearity better than 10^{-6}. Online filtering and noise cancellation could be carried out in real time with the *field programmable gate array* (FPGA) circuitry.

4.3 Registration and Stimulation Facilities

The shape of a subject's head was acquired by running a three dimensional digitization system over the subject's scalp. A three dimensional digitization ISOTRAK system made by Polhemus was used (Fig 4.8), which determined localization by generating and sensing magnetic fields. The system consisted of maximal two receivers and one transmitter, and the effective distance between transmitter and receiver was less than $800mm$ and $1100mm$ with $TX2$ and $TX4$ transmitters respectively. The transmitter contained electromagnetic coils emitting the magnetic fields, which provided the reference frame for receiver measurement. The receiver also contained electromagnetic coils and purely passively detected the magnetic fields produced by the transmitter. The localization resolution could reach 0.0015 of the distance between transmitter and receiver in the radial direction and 0.1° in the radial orientation. The receiver was isotropic in all directions, with an update rate as high as 60 updates per second. A latency of $20ms$ was present during localization without software filtering. The head shape was sampled continuously with the assistance of a stylus, while reference points defining the MEG coordinates were sampled in a discrete manner.

The anatomical images were acquired with a $1.5T$ Siemens Magnetom Vision scanner, via a *three dimensional magnetization prepared rapid gradient echo* (3D MP-RAGE) sequence [62]. The scanner was actively shielded to have minimal field outside of the scanner and was equipped with an external interference shield. The scanner was a whole body system, supplied with gradient coils capable of delivering $25mT/m$. The 3D MP-RAGE sequence iterated through a magnetization preparation, rapid gradient echo acquisition and magnetization recovery to cover the desired range of reciprocal space. The T_1 contrast was encoded into the image through an inversion recovery sequence $TI = 300ms$ during the magnetization preparation period, with the application of 12° small flip angle pulses to raise the scanning speed. The resolution of the image was $1mm \times 1mm \times 1mm$ with the matrix size $256 \times 256 \times 256$.

The stimulator used in this study was of a vibrotactile nature, designed to produce minimal interference to the scanners. The core element of the stimulator

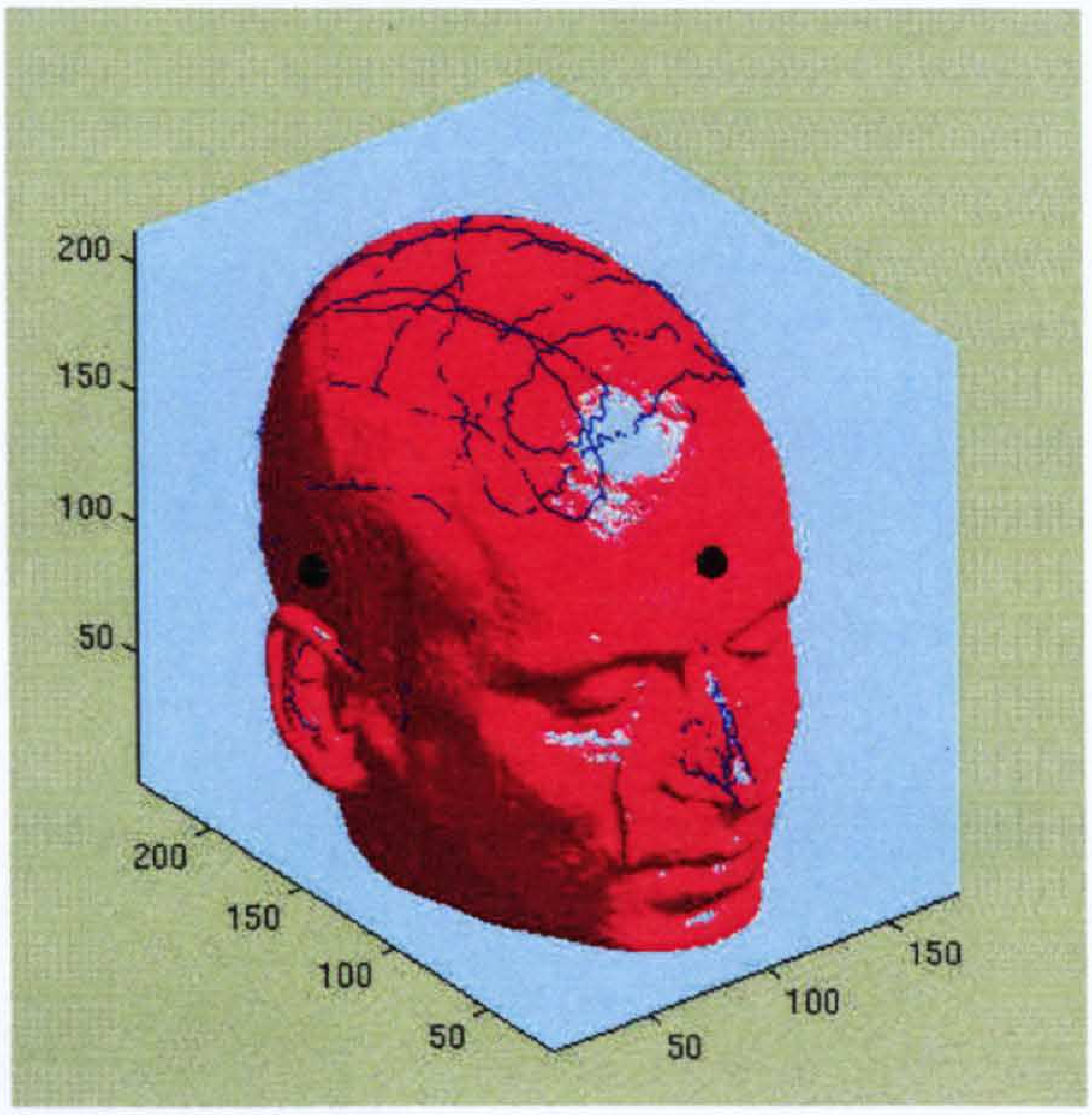

Figure 4.8: The picture shows the position of anatomical references, digitized head shape and reference coils, illustrating the mechanism of representing the brain activities in the same coordinate system.

was a bending motor piece made by Piezo System, part number $T220-H4-503Y$. The Piezo element was an unmounted double layered element with dimensions of $63.5mm \times 31.8mm \times 0.5mm$. It was made of $PSI-5H4E$ Piezoceramic material reinforced by brass, with the same polarization for both layers. The unit was capable of delivering stimulation within the frequency range $20Hz$ - $300Hz$ with a peak deflection of $400\mu m$. In the studies, a constant amplitude of $150\mu m$ was applied to the digit 2 and 5 of volunteer's right hand at frequencies $40Hz$ and $200Hz$.

Chapter 5

fMRI and MEG Spatial Comparison

5.1 Introduction

5.1.1 Aim of the study

FMRI and MEG are two independent functional brain research modalities, whose mechanisms are utterly different from each other. Appropriate strategies are necessary for the correct interpretation of the complementary information embedded in both modalities to derive an undistorted and comprehensive picture of brain function. To enable these two techniques to be compared, an approach capable of identifying signal sources without introducing artifacts or errors is needed.

The temporal characteristics of fMRI and MEG are substantially different. The temporal resolution of MEG is less than a millisecond, tracking rapid electrophysiological changes. FMRI often struggles to reach sub-second levels with reasonable *signal to noise ratio* (SNR) , monitoring the slow hemodynamic response. It is obvious that little in common can be found between fMRI and MEG with regard to temporal aspects. It is therefore inappropriate to base the combination of fMRI and MEG on their communal temporal features.

Although the spatial localization of fMRI and MEG is different, the feasibility of establishing spatial correspondence is still available. Signals detected by MEG are the direct results of neuronal electric activity, while the errors of activation localization are mainly due to noise and the imperfect modelling of the inverse problem. Although fMRI reflects the hemodynamic response induced by brain activity, the dense population of capillaries allows sufficiently accurate spatial representation of neuronal activity. Consequently, establishing the spatial correspondence appears to be the primary candidate for relating the modalities.

It is also a fact that these two modalities are based on two different mechanisms both from the point of view of physical principles and of physiological principles. Systematic errors may occur according to the degree of deviation of reality from the ideal model assumed by each modality. Different responses and sensitivities towards various configurations of brain activity can therefore be expected. It is fully possible that certain brain activity configurations are only detectable by a single modality, which challenges the correctness and accuracy in correspondence between modalities.

Facing these challenges, the following study examined the feasibility of establishing spatial correspondence between fMRI and MEG. The application of each modality followed its respective well established conventions of data acquisition and analysis to allow adequate robustness. The somatosensory stimulus is not only widely used and well explored, but has been proven to induce results of great simplicity in both modalities. The choice of a somatosensory stimulus and its application on different fingers allows an effective comparison of the two modalities. Spatial comparison between MEG and fMRI had been carried out on both sensory and motor cortex, resulting in an estimate of spatial mismatch between $10mm$ and $15mm$. [103, 104] The vibrotactile stimulus of different frequency applied to different fingers induces different patterns of cortical activity, allowing an effective spatial·comparison between modalities on both cortical and subcortical spatial scales. Therefore a finer assessment of the two modalities can be achieved both in terms of the spatial agreement and the consistency of the activation patterns.

5.1.2 Somatosensory Anatomy and Function

The human body is composed of several functionally distinctive systems such as the circulatory system, respiratory system and nervous system. Most systems act as infrastructure components to support active and dynamic reaction of the body towards the external environment, mostly under the charge of the nervous system. The nervous system observes the external environment via sensory receptors. The gathered information is delivered into the central nervous system to generate self protective reflexes, and transferred further into the brain to form conscious perceptions. After the neuronal process, the brain may command the skeletal muscles to contract in response to the perceived situation.

The nervous system involved in the sensation and perception of the external environment is known as the sensory system. The sensory system consists of all types of sensation, in which the somatosensory system dealing with mechanical stimulus is one of the most developed systems. The sensory system also performs the functions of limb proprioception and arousal, with related receptors allocated around the body.

Sensory stimulus is transformed into neuronal signals by receptors classified as dorsal ganglion neurons, where the cell body lies in a ganglion on the dorsal root of a spinal nerve. The axon has two branches with one projecting to the central nervous system, while the other projects to the periphery with its specialized terminal sensitive to a particular form of stimulus. The function and capability of receptors depend on the anatomical structure of the terminals. Mechanical stimuli applied on finger tips activate four different types of mechanoreceptors, namely Meissner's corpuscle, pacinian corpuscle, Merkel's corpuscle and Ruffini's corpuscle. Based on their receptive fields, Meissner's corpuscle and Merkel's corpuscle are superficial receptors in contrast to the pacinian corpuscle and Ruffini's corpuscle of subcutaneous receptors. Mechanoreceptors can also be divided according to their rate of adaptation, with slowly adapting receptors continuing to respond to a steady stimulus whereas the rapidly adapting mechanoreceptors only respond at the beginning of the stimulus. Meissner's corpuscle and pacinian corpuscle are rapid adapting receptors, while the Merkel's corpuscle and Ruffini's corpuscle are slowly adapting receptors. The response function of rapidly adapting receptors can be studied by applying a threshold level monochromatic mechanical waveform onto the terminals at a series of frequencies, from which it can be deduced that Meissner's corpuscle is more sensitive to low frequency stimuli, whereas the pacinian corpuscle is more sensitive to high frequency stimuli. However, mechanical stimuli generally cause the activation of all four types of mechanoreceptors, providing sufficient information to the higher order nervous system for constructing a comprehensive picture of the input stimulus.

The information from receptors is passed by afferent nerve fibres, which together with local efferent nerve fibres form peripheral nerves. Peripheral nerves join together and form spinal nerves near the spinal cord. The afferent fibres separate dorsally from efferent fibres and enter the spinal cord through dorsal roots. The dorsal roots are organized segmentally, while the peripheral nerves in a local region are redistributed among nearby segments of dorsal roots. The spinal cord is a structure of butterfly shaped gray matter surrounded by white matter. The gray matter contains nerve cell bodies, while white matter contains axons ascending to and descending from the brain, most of which are myelinated. The spinal cord is also topographically organized, where the dorsal areas mainly deal with afferent pathways and the ventral areas are in charge of the efferent issues. The spinal cord is the first level relay point, where the convergence and divergence of neuronal messages take place with some possible basic reflexes generated. The white matter is organized into columns, and the tactile sensation is relayed to brain through the dorsal column medial lemniscal system.

The dorsal column delivers tactile sensation ipsilaterally to the caudal medulla, where the nerves synapse on the cells of the dorsal column nuclei. (Fig 5.1) At that point, the tract decussates and projects to the thalamus as the medial lemniscus, a brain stem pathway, and subsequently to the anterior parietal cortex through the internal capsule. (Fig 5.2)

The human cerebral cortex is anatomically divided into lobes according to their specific functions. (Fig 5.4) The tactile sensation is under the charge of the parietal lobe. The parietal lobe is locates posterior to the central sulcus, anterior to the parieto-occipital sulcus and superior to the lateral fissure. The

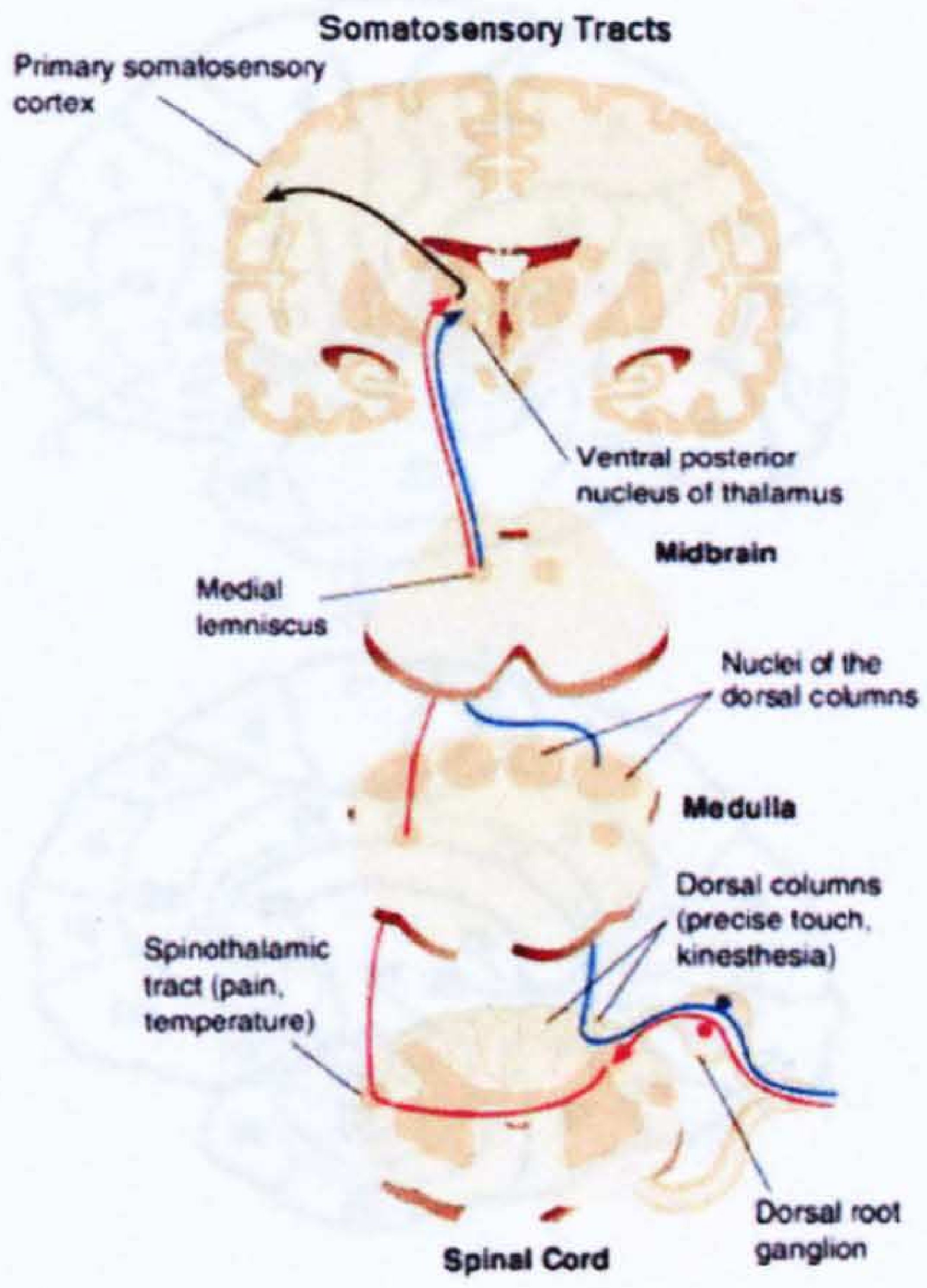

Figure 5.1: A diagram showing the transfer path of somatosensory signal. The tactile sensation is passed ipsilaterally in the spinal cord in contrast to the pain stimulus. From *Fundamental Neuroscience* by *Duane E. Haines.*

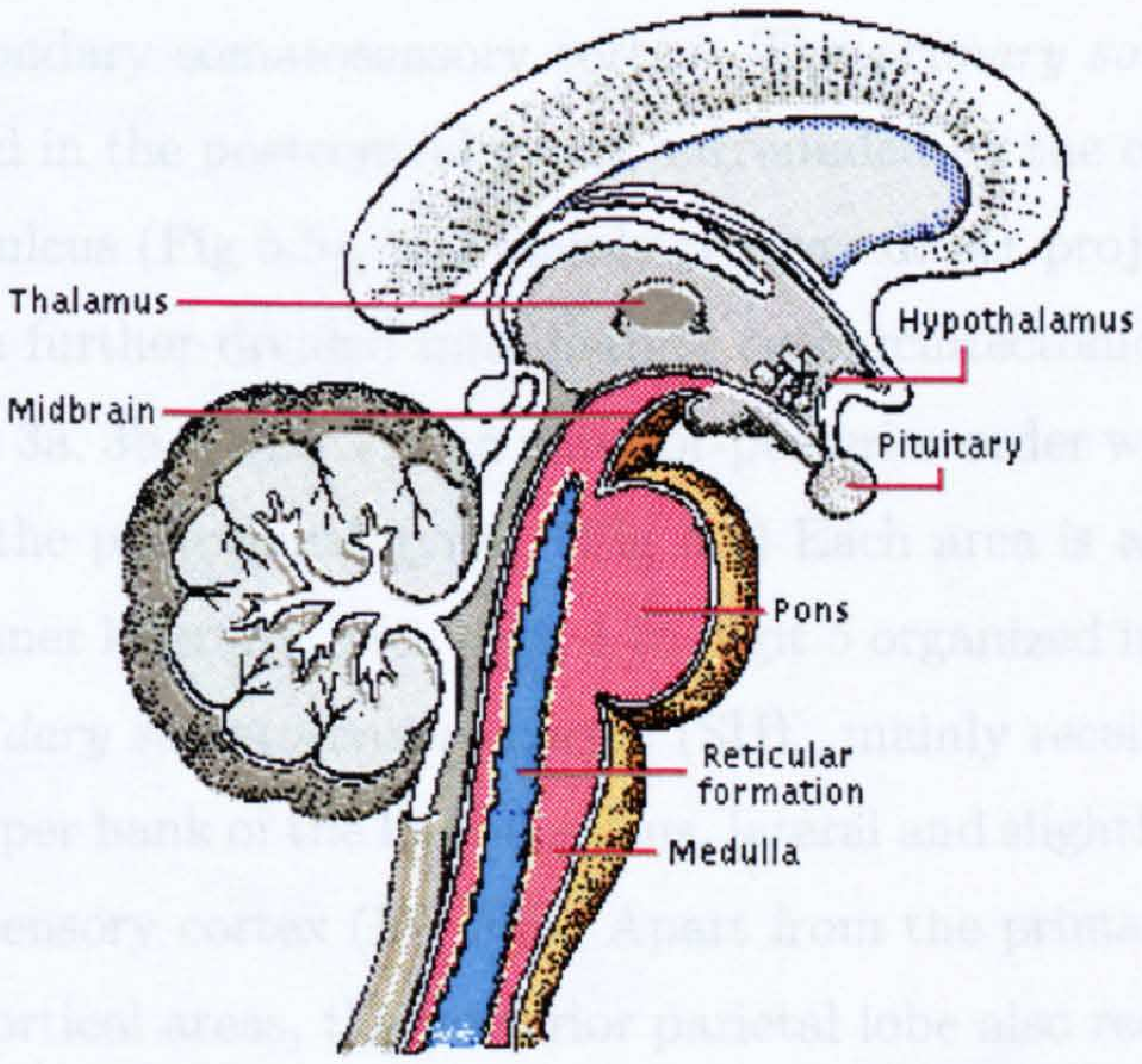

Figure 5.2: A map demonstrating the anatomical components of the human brain. From *Human Brain - An Introduction to Its Functional Anatomy* by *John Nolte.*

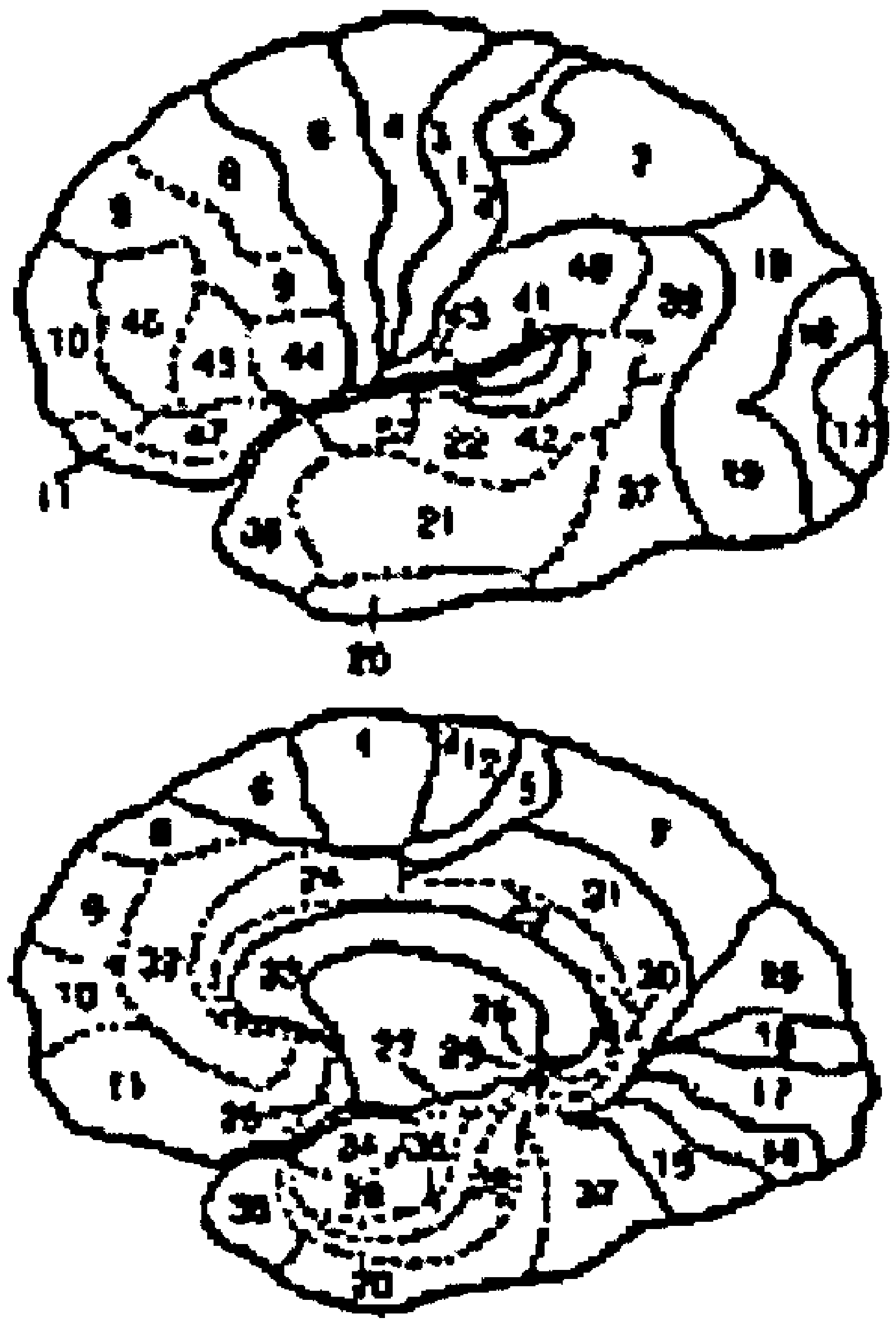

Figure 5.3: A lateral medial view of the Brodmann anatomical division system. From *Fundamentals of Human Neuropsychology*, by *Bryan Kolb* and *Ian Q Whishaw.*

somatosensory cortex lies on the anterior parietal cortex, mainly consisting of primary and secondary somatosensory cortex. The *primary somatosensory cortex* (SI) is located in the postcentral gyrus, surrounded by the central sulcus and the postcentral sulcus (Fig 5.5), and mainly receives direct projections from thalamus. SI can be further divided into distinct cytoarchitectonic regions, namely Brodmann's area 3a, 3b, 1 and 2 in an anterior-posterior order with area 1 located at the centre of the postcentral gyrus. (Fig 5.3) Each area is also arranged in a somatotopic manner laterally, with digit 1 to digit 5 organized in a lateral-medial order. The *secondary somatosensory cortex* (SII) , mainly receives input from SI and lies in the upper bank of the lateral sulcus, lateral and slightly posterior to the primary somatosensory cortex (Fig 5.5). Apart from the primary and secondary somatosensory cortical areas, the posterior parietal lobe also receives somatosensory input and acts in higher order functions such as integrating somatosensory modalities to form perception and relating sensory and motor processing. Similar to the primary somatosensory cortex, the posterior parietal cortex is subdivided into Brodmann's area 5 and 7 in an anterior-posterior order.

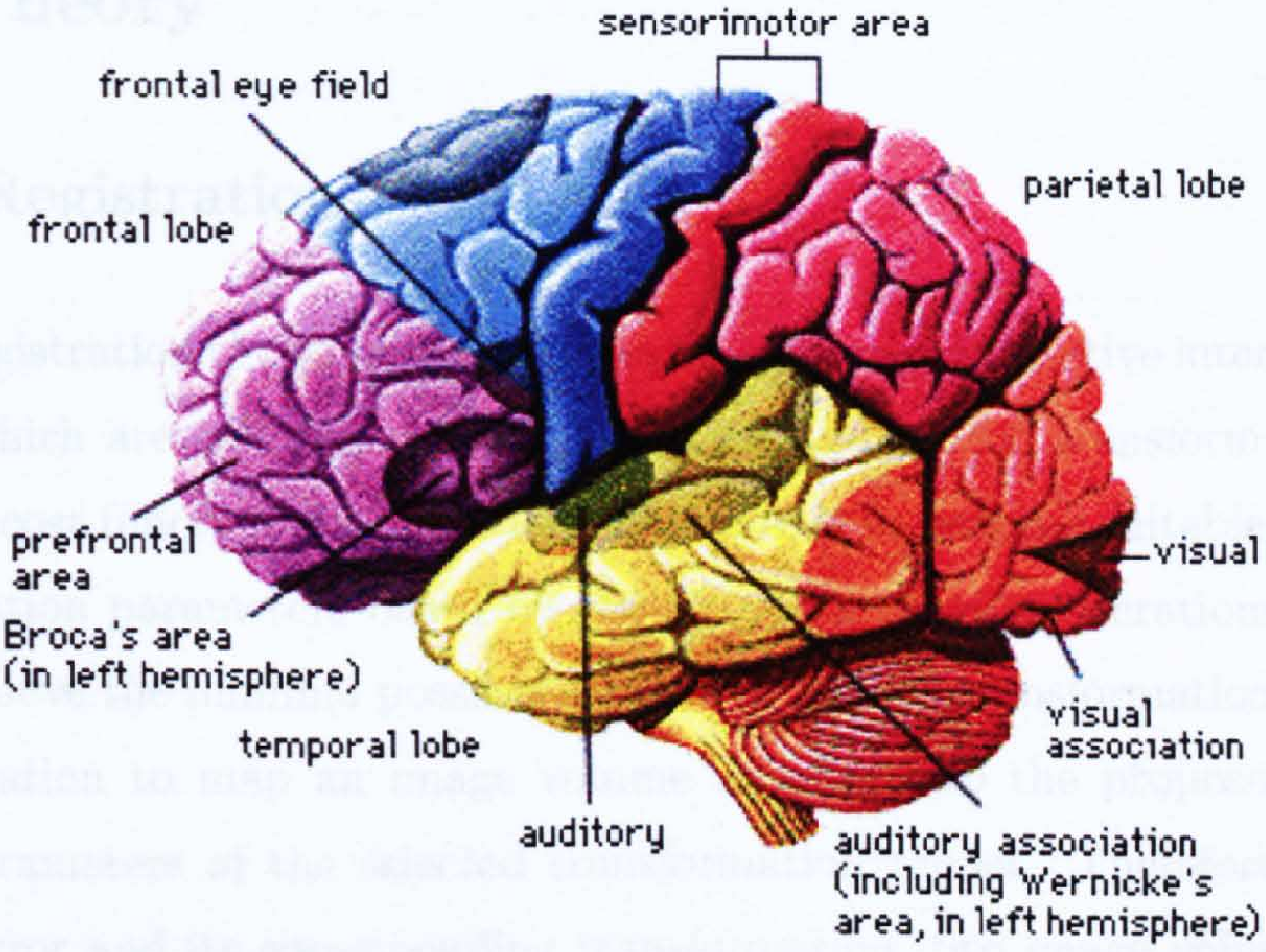

Figure 5.4: A diagram showing the division of cerebral cortex according to specific functions. The coordinate system adopted originates at right-superior-anterior corner,and has x from right to left, y from superior to inferior and z from anterior to posterior. From *Fundamental Neuroscience* by *Duane E. Haines.*

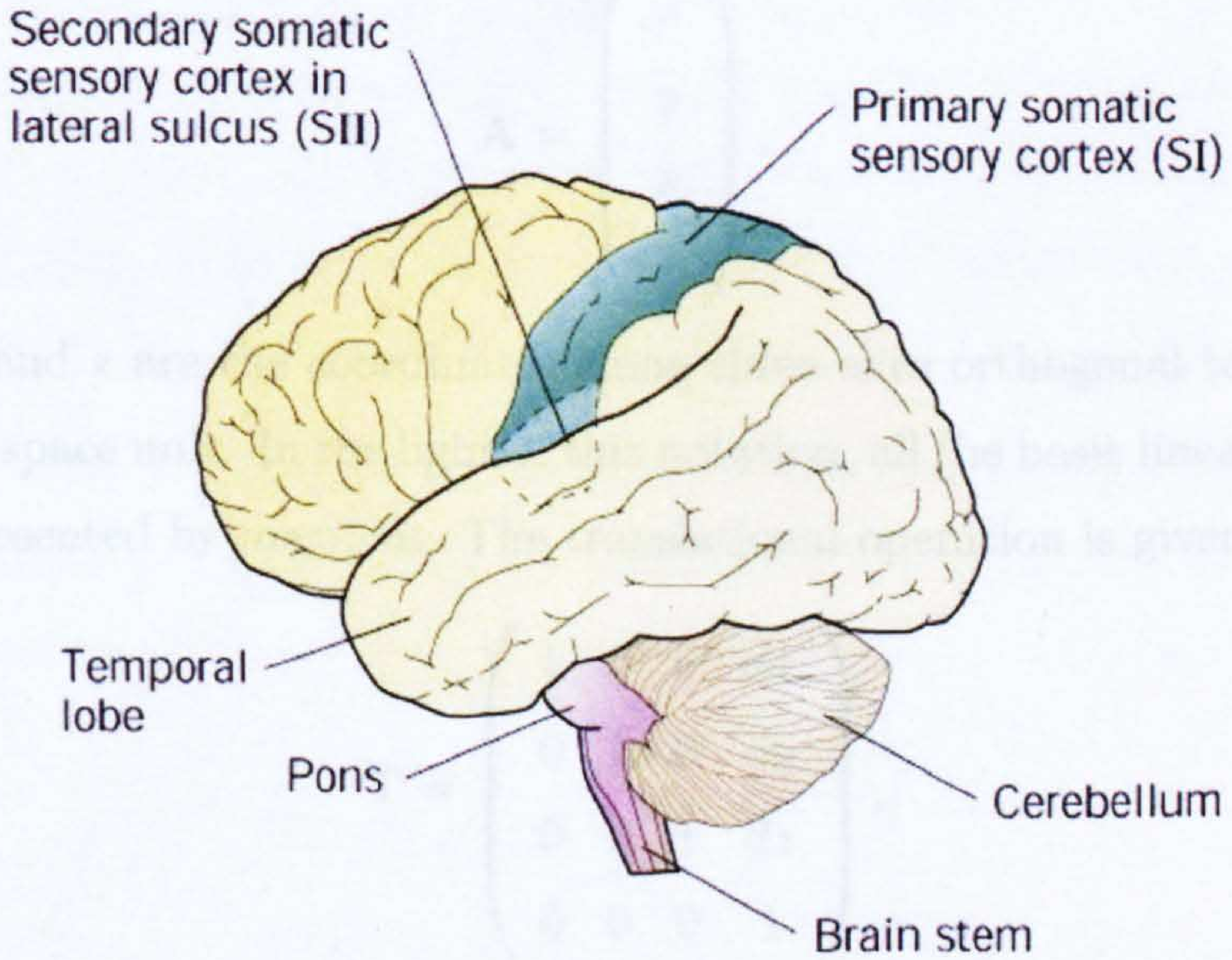

Figure 5.5: A diagram illustrating the location of primary and secondary somatosensory areas. From *Human Brain - An Introduction to Its Functional Anatomy* by *John Nolte.*

5.2 Theory

5.2.1 Registration

The registration of two image volumes involves two distinctive interlinked procedures, which are cost function minimization and spatial transformation. The aim of the cost function minimization procedure is to propose suitable changes in transformation parameters based on the results of previous iterations, and ultimately achieve the minimal possible error. The spatial transformation procedure is an operation to map an image volume according to the proposed transformation parameters of the selected transformation model. Therefore, with the minimal error and its corresponding transformation, two image volumes can be aligned together on the basis of the definition of the cost function and the applied transformation model.

A point in space can be identified by its cartesian coordinates and a clear definition of the space unit, so that a spatial position, $\mathbf{A}$, can be described by a four element vector as

$$\mathbf{A} = \begin{pmatrix} x \\ y \\ z \\ 1 \end{pmatrix}, \tag{5.2.1}$$

where x, y and z are the coordinates along three axes orthogonal to each other, and 1 is the space unit. In the light of this notation, all the basic linear transforms can be represented by matrices. The translational operation is given by

$$\mathbf{T} = \begin{pmatrix} 1 & 0 & 0 & dx \\ 0 & 1 & 0 & dy \\ 0 & 0 & 1 & dz \\ 0 & 0 & 0 & 1 \end{pmatrix}, \tag{5.2.2}$$

where dx, dy and dz are the spatial displacement along x, y and z axes respectively. The resultant coordinates are given by $\mathbf{A}' = \mathbf{TA}$. Since the translation operations commute with one and another, all the translations can be written into one matrix to be performed together or carried out separately in any order. The rotational operations do not commute with one another, and therefore should be performed separately in sequence. The matrix representation of rotation is given by

$$\mathbf{R}_x = \begin{pmatrix} 1 & 0 & 0 & 0 \\ 0 & \cos\theta_x & -sin\theta_x & 0 \\ 0 & sin\theta_x & \cos\theta_x & 0 \\ 0 & 0 & 0 & 1 \end{pmatrix}, \tag{5.2.3}$$

$$\mathbf{R}_y = \begin{pmatrix} sin\theta_y & 0 & \cos\theta_y & 0 \\ 0 & 1 & 0 & 0 \\ \cos\theta_y & 0 & -sin\theta_y & 0 \\ 0 & 0 & 0 & 1 \end{pmatrix}, \tag{5.2.4}$$

$$\mathbf{R}_z = \begin{pmatrix} \cos\theta_z & -sin\theta_z & 0 & 0 \\ sin\theta_z & \cos\theta_z & 0 & 0 \\ 0 & 0 & 1 & 0 \\ 0 & 0 & 0 & 1 \end{pmatrix}, \tag{5.2.5}$$

where $\mathbf{R}_x$, $\mathbf{R}_y$ and $\mathbf{R}_z$ are the rotation matrices on x, y and z axes respectively with the rotation angles θ_x, θ_y and θ_z denoted in right hand conventions. The translation and rotation constitutes the rigid body transformation, governed by six parameters. (Although 12 matrix elements are involved in these operations, they are not independent from each other, and only 6 independent variables exist in this model.)

If the model is chosen to allow plasticity, additional scaling and shear operations are involved. The scaling operations commute with one and another, and are described by

$$\mathsf{S} = \begin{pmatrix} S_x & 0 & 0 & 0 \\ 0 & S_y & 0 & 0 \\ 0 & 0 & S_z & 0 \\ 0 & 0 & 0 & 1 \end{pmatrix}, \tag{5.2.6}$$

where S_x, S_y and S_z are the scaling factors along x, y and z axes respectively. Shear is an operation that shifts the object along the shearing line at a displacement proportional to the distance between them. The matrix representation of the shear operation is given by

$$\mathbf{H}_x = \begin{pmatrix} 1 & k_{xy} & k_{xz} & 0 \\ 0 & 1 & 0 & 0 \\ 0 & 0 & 1 & 0 \\ 0 & 0 & 0 & 1 \end{pmatrix}, \tag{5.2.7}$$

$$\mathbf{H}_y = \begin{pmatrix} 1 & 0 & 0 & 0 \\ k_{yx} & 1 & k_{yz} & 0 \\ 0 & 0 & 1 & 0 \\ 0 & 0 & 0 & 1 \end{pmatrix}, \tag{5.2.8}$$

$$\mathbf{H}_z = \begin{pmatrix} 1 & 0 & 0 & 0 \\ 0 & 1 & 0 & 0 \\ k_{zx} & k_{zy} & 1 & 0 \\ 0 & 0 & 0 & 1 \end{pmatrix}, \tag{5.2.9}$$

where k_{ij} is the shearing factor of the ith axis on the jth component. Since the shear operations do not commute with each other, this transformation should be carried out in sequence.

Any number of linear transformations can be combined by matrix multiplications:

$$\begin{aligned} \mathbf{A}' &= \mathbf{O}_n \ldots \mathbf{O}_2\mathbf{O}_1\mathbf{A} && (5.2.10) \\ &= \mathbf{OA}, && (5.2.11) \end{aligned}$$

where $\mathbf{O}_i$ is the ith operation performed on $\mathbf{A}$, and $\mathbf{O} = \mathbf{O}_n \ldots \mathbf{O}_2\mathbf{O}_1$ is the combined operation performed on $\mathbf{A}$ to derive the new position $\mathbf{A}'$. Since $\mathbf{O}$ is a 4×4 matrix with only 12 active elements to adjust the outcome of the operation, the highest flexible model that can be used is a 12 parameter model.

Nonlinear transformation solutions have also been developed. The result of nonlinear transformation depends on the weighted sum of polynomial combinations of all the axes to a certain order. The number of changeable parameters and highest order are often limited to ensure that the minimization algorithm can be performed successfully.

After a transformation, a discretely digitized object is transformed into another form with new spatial coordinates. However, the spatial sampling is changed in consequence, imposing an obstacle for comparing two objects originally based in the same discrete sampling space. To restore the same sampling space, the object has to be sampled again following appropriate interpolation. Various interpolation algorithms are available, among which trilinear sampling is most widely used. Trilinear interpolation is simply a distance weighted average of the first level neighbour object points to the new sampling point. Consequently a new object in a fixed sampling grid can always be attained after any spatial transformation.

After correctly formulating the registration problem into cost functions and transformation models, minimization algorithms are applied to align the two objects. A huge variety of minimization algorithms has been developed to reliably and quickly reduce the residual error. Although some algorithms use multi resolution searching through error space to guard against local minima issues, no guarantee can be given to ensure correct results are reached. Since most algorithms investigate the local error space rather than iterating through the whole error space, chances of mismatch due to local minima can never be eliminated. The quality of a minimization algorithm is assessed by its robustness against local minima and speed of convergence.

5.3 Methods

5.3.1 Materials and Stimulus Presentation

This study was carried out on three healthy right-handed male volunteers aged from 20 to 40. The tactile stimulus was delivered to the right hand of subjects, on digit 2 and digit 5 separately during different experimental sessions.

The stimulus was generated by a piezoelectric sensory stimulator, which had the capability of producing a peak deflection of $400\mu m$ to the finger in the frequency range between $20Hz$ and $300Hz$. The vibration of a sinusoidal oscillation at an amplitude of $150\mu m$ was applied to individual fingers. For each finger, two sessions were performed with stimulator oscillation frequencies at $40Hz$ and

$200Hz$. It was proven that the interference of the stimulator on both fMRI and MEG systems was neglectable.

The paradigms for fMRI and MEG studies were tailored to each modality. In the fMRI studies, an $8s$ long stimulus was adopted to achieve the full reaction of the hemodynamic response and was followed by a $24s$ long resting period to allow the response to adequately return to the baseline. This stimulus cycle was repeated 15 times for each subject with additional saturation scans appended in front. A $2s$ long stimulus followed by a $4s$ long resting period was used in MEG studies to shorten the cycle length while maintain a large number of cycles.

5.3.2 fMRI Methods

The fMRI studies were performed with a surface coil of $14cm$ diameter on a $3.0T$ home built scanner. The *Modulus Blipped Echo Planar Single-Pulse Technique* (MBEST) EPI sequence with an echo time of $TE = 35ms$ and switching gradient frequency of $1.9kHz$ was selected to acquire T_2^* weighted images. Ten contiguous sagittal slices with matrix size of 128×128 were acquired continually with the same interval between slices at a volume wise repetition time of $TR = 2s$. The volume has $2.5mm$ and $4mm$ resolution in plane and through plane respectively.

With reasonable rf shielding, it was not necessary to perform any rf correction of the acquired data to remove rf lines. The raw data was ghost corrected using home written software, although the *pre-sampling delay* (PSD) had been set to minimize the first order ghost. Subsequently, the data was reorganized to correspond to an ordered grid in reciprocal space, and was two dimensional Fourier transformed into real space magnitude images with appropriate scaling to retain sufficient dynamic range. The centre of each image was replaced with the averaged value of neighbor pixels to correct the DC offset arising from the analogue electronics.

The saturation scans were then extracted, and the images were segmented to reduce the matrix size for computational efficiency. The images were organized into volumes for motion correction based on the six parameter rigid body transformation. The motion correction algorithm performed was provided by *Automated Image Registration* (AIR) integrated within *MEDx* (Sensor Systems, Inc.) with an appropriate threshold to outline the boundary of the brain. The 6 parameters corresponded to translation and rotation in three mutually orthogonal directions, as demonstrated in detail in the previous sections. The aligned images were then normalized (intensity wise) to eliminate the effect of variation in global inflow. Although no spatial smoothing was performed on the processed images, temporally the individual pixel time series were convolved with a Gaussian kernel of $3s$ *Full Width at Half Maximun* (FWHM) and high pass filtered to $0.02Hz$ to eliminate low frequency hardware drift.

The individual pixel time course was correlated to the stimulus time course convolved with a gamma variate function to derive statistical parametric maps. Based on the Gaussian random field theory, the statistical map was then clustered and displayed with a threshold of corrected p-value of 0.05. The activation sites were then located according to the *centre of mass* (CoM)of each cluster.

5.3.3 MEG Methods

The MEG studies were performed on a 151 channel whole cortical MEG system (CTF System, Inc.). The MEG space was defined by three reference coils attached to the subject at nasion and bilateral preauricular points, both fitting into anatomical features and providing robust signal to the system. Fingerprint frequencies were fed into the coils pre and post the experiment to be located by the system. The cumulated spatial displacement of subject can therefore be determined, which gives an indication of the robustness of the result. Although remaining in place, the reference coils were not in use during the experiment due to the increased solution instability, which would result from an increased number of signal sources.

The extracranial magnetic field was detected in the third order gradiometer mode. The signal was digitized at a sampling rate of $2083Hz$ and filtered with a $400Hz$ anti aliasing filter. The time series were then low pass filtered at $80Hz$, high pass filtered at $10Hz$ and power line frequency eliminated, to enclose the usual neuronal activity range and at the same time reduce the interference of noise. Each experiment was averaged over 100 trials, selected on the basis of the evoked responses and recognized artifacts and noise, to derive the mean trial with increased *signal to noise ratio* (SNR) . The localization of the *Equivalent Current Dipole* (ECD) was achieved by comparing the ideal field with the measured field map and maximizing the goodness of fit index. The ideal field map was generated based on a spherically symmetric conductor model, with the sphere best fitted to the inner surface of the skull. The residual error was assessed to determine the necessity of introducing extra sources, until the goodness of fit index was better than 80 percent. The stability of the solution was subsequently tested by *Monte Carlo* analysis to derive the 95% confidence range.

5.3.4 Registration

The anatomical images of the subjects were acquired on a $1.5T$ MRI scanner (Siemens, Magneton Vision), using a 3D MPRAGE sequence. The images were T_1 weighted, with an echo time of $TE = 4ms$, an inversion time of $TI = 25ms$ and a slice repetition time of $9.7ms$. The volume had an resolution of $1 \times 1 \times 1mm^3$, with a sampling number of 256 on both anterior-posterior and superior-inferior directions. The *Field of View* (FOV) in the lateral direction is sufficiently large to cover the whole head.

In fMRI studies, a mean volume image was generated by averaging all the volumes in the fMRI time series, while the anatomical images were segmented to include only brain tissues to reduce the contrast difference imposed by the sequences. By best fitting the mean fMRI image volume with the anatomical images, a transformation can be achieved based on a 12 parameter transformation algorithm provided by AIR integrated within MEDx. The transformation was performed on translation, rotation, scaling and shear on three mutually orthogonal directions, as detailed in previous sections. The resultant transformation was then applied to the cluster positions to form the activation pattern in anatomical space.

In MEG studies, a bite bar system was devised to allow the subject's head to be secured for a short period. (The subject's jaw position was locked by the personalized indentation on the bite bar.) After the MEG experiment, the subject moved out of the scanner with the reference coils intact, and bit onto the bite bar in a firm and stable position. Each reference coil was sampled ten times by ISOTRAK (Polhemus) to render its spatial relationship with respect to the bite bar, and subsequently removed. The MEG spatial coordinate system could then be mapped onto the space defined by the bite bar. With the subject maintaining the same position, the profile of the subject's scalp was then sampled by running the detector around with the landmark features such as the nose highlighted. The profile of the subject's scalp was also attained by extracting the outmost layer in the anatomical images with a three dimensional segmentation algorithm provided by the MEG system. A volume lookup table was constructed, in which the value in each pixel was the distance from that pixel to the nearest scalp surface. Therefore the distance between one point in the digitized scalp profile to the surface of scalp could be retrieved efficiently by treating the corresponding pixel in the lookup table. The mismatch between the two scalp profiles was calculated by the summation of all the distances indicated by the lookup table. A six parameter rigid body transformation, based on translation and rotation on three mutually orthogonal directions described in previous sections, was used to minimize this mismatch. Since the digitized scalp profile was sampled in the space defined by the bite bar, the MEG spatial coordinate system, defined by reference coils, could then be mapped onto anatomical space with the assistance of the derived transformation. Through all these linear transformation, the activation site and related confidence range can be finally mapped onto anatomical references.

5.4 Results

5.4.1 fMRI Results

Following identical statistical analysis, all the experiments in the fMRI studies resulted in several distinguishable and consistent clusters. The cluster positions were represented in pseudo Talairach coordinates, sharing the same orientation as the conventional Talairach space, for ease of comparison. Talairach space is defined using the line crossing through the superior edge of the anterior commissure and the inferior edge of the posterior commissure which is taken as the anterior-posterior direction. The modified coordinates thus have origins at the right-superior-anterior corner of the anatomical volume instead of the anterior commissure, with the x-axis pointing from right to left, y-axis along from superior to inferior and z-axis directing from anterior to posterior.

Subject	1	2	3
Digit 2 SI area 1 $40Hz$	(178,52,108)	(182,65,110)	-
Digit 2 SI area 3b $40Hz$	(169,62,109)	(175,70,110)	(170,51,114)
Digit 2 SI area 1 $200Hz$	(178,52,108)	(182,65,110)	-
Digit 2 SI area 3b $200Hz$	(169,62,109)	(175,70,110)	(170,51,114)
Digit 5 SI area 1 $40Hz$	(151,35,96)	(153,53,88)	-
Digit 5 SI area 3b $40Hz$	(168,58,105)	(173,68,110)	(172,49,113)
Digit 5 SI area 1 $200Hz$	(151,35,96)	(153,53,88)	-
Digit 5 SI area 3b $200Hz$	(168,58,105)	(173,68,110)	(172,49,113)

Table 5.1: The centre of mass (mm) of clusters identified in the primary somatosensory area for all three subjects, where both the frequency and the digit the stimulus was applied to are shown.

According to the corresponding centre of mass, these clusters were anatomically recognized as Brodmann's area 1 (Table 5.1) located at the crown of the postcentral gyrus, Brodmann's area 3b (Table 5.1) and the secondary somatosensory area. Two clusters were identified in the secondary somatosensory area and anatomically recognized as anterior and posterior operculum. All the activation clusters appeared on the contralateral side to the stimulus presentation, restricted by the employment of a surface coil.

The studies performed on different fingers showed a shift in cluster position in Brodmann's area 1 and 3b (Table 5.2). Consequently a subcortical topography can be analyzed for the respective fingers. This type of cluster shift was not noticed in the secondary somatic sensory area.

Subject	Digit 2 and Digit 5 Separation
1	6.9
2	2.8
3	3.0
$M \pm \delta$	4.2±2.3

Table 5.2: The differences between the centres of mass (mm) of clusters identified in Brodmann's area 3b, induced by the different digits the stimulus applied to. The coordinates for each finger were obtained by averaging the corresponding 40 Hz and 200 Hz results.

The attained results agree with the established knowledge, in terms of both the expected activation site and subcortical arrangement, following the knowledge of neuronal projections.

5.4.2 MEG Results

All the channels of the averaged trial were analyzed, from which two analysis time windows were identified based on evoked responses of $50ms$ to $69ms$ and $90ms$ to $147ms$ post onset of the stimulus (Fig 5.6). To map the brain activities detected by MEG, rigid body transformation described in previous section was employed to match the MEG coordinates defined by reference coils and anatomical space. An *Equivalent Current Dipole* (ECD) can be reliably fitted from the first time windows for both fingers and stimulus frequencies, and was subsequently identified anatomically as located in Brodmann's area 3b of the primary somatosensory cortex (Table 5.3). However, no ECD could be reliably fitted to the second analysis window for the stimulus frequency of $40Hz$, while the results from the studies with a stimulus frequency of $200Hz$ indicated an ECD located in the secondary somatosensory cortex. All the dipoles were located contralaterally to the side of the stimulus presentation.

The dipoles located in Brodmann's area 3b in the primary somatosensory cortex can be further distinguished according to the fingers stimulated, and therefore the separation of the dipoles can be used to mark the dipole pattern presented

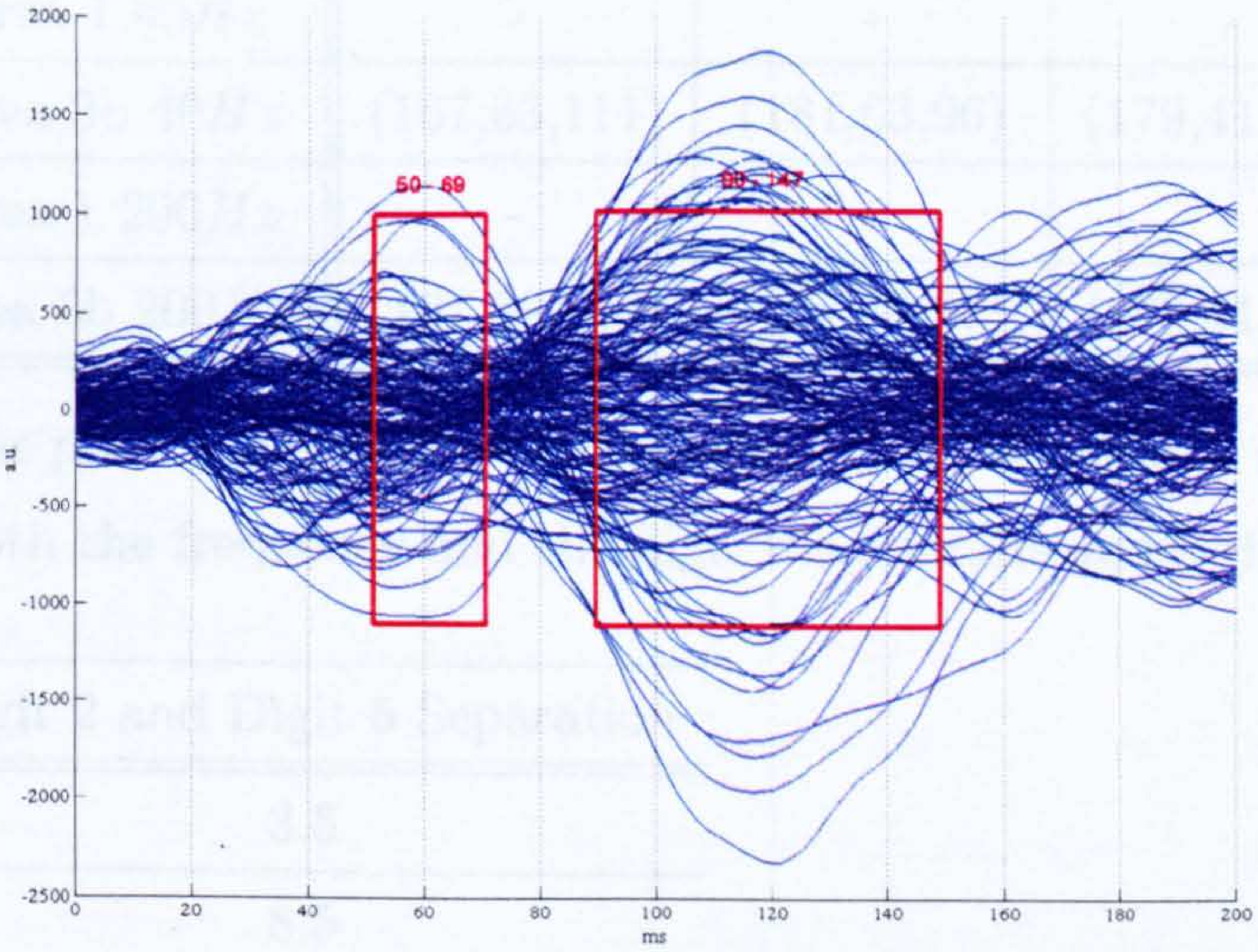

Figure 5.6: The time courses of all the channels overlayed together post the onset of the stimulus acquired from a typical subject, with a stimulus of 200 Hz delivered to digit 2, showing the evident analysis windows of 50 ms to 69 ms and 90 ms to 147 ms post onset of the stimulus. The equivalent current dipoles located in first and secondary somatosensory area were identified from the first and the second window respectively.

by the cortical topography (Table 5.4). However, the cortical topographical representation of different fingers could not be distinguished in our experiments.

Subject	1	2	3	4	5	6
Digit 2 SI area 1 40Hz	-	-	-			
Digit 2 SI area 3b 40Hz	(168,65,115)	(180,54,107)	(170,52,110)			
Digit 2 SI area 1 200Hz	-	-	-			
Digit 2 SI area 3b 200Hz	(168,63,112)	(169,71,102)	(168,52,104)			
Digit 5 SI area 1 40Hz	-	-	-			
Digit 5 SI area 3b 40Hz	(167,63,111)	(181,63,96)	(179,41,107)			
Digit 5 SI area 1 200Hz	-	-	-			
Digit 5 SI area 3b 200Hz	(167,62,110)	(164,58,97)	(179,41,107)			

Table 5.3: The positions (mm) of ECDs identified in the primary somatosensory area, where both the frequency and the digit the stimulus applied to are shown.

Subject	Digit 2 and Digit 5 Separation
1	3.5
2	8.5
3	14.5
$M \pm \delta$	8.8±5.5

Table 5.4: The differences between ECDs (mm) identified in Brodmanns area 3b, induced by the different digits the stimulus applied to. The coordinates for each finger were obtained by averaging the corresponding 40 Hz and 200 Hz results.

These findings conform to the literature. The detected temporal feature and the location of revealed dipoles are expected.

5.5 Discussion

5.5.1 Spatial Comparison between fMRI and MEG

It is apparent from the results presented that no dipole was found by MEG in Brodmann's area 1, whereas the fMRI studies have clearly shown a cluster within this region. This is likely to be the result of the insensitivity of MEG towards radial current dipoles under a symmetric spherical conductor model, since the cortical formation of Brodmann's area 1 dictates an evoked current dipole mainly pointing at radial direction. In this case, the magnetic field induced by the tangential component of the evoked current dipole was trivial and regarded as noise. However, the fitting error was reasonably small, putting this speculation into question. The disappearance of Brodmann's area 1 in MEG studies can also be the result of modelling error. Since anatomically Brodmann's areas 1 and 3b are in close proximity to each other, a single dipole model may be sufficient to match the fields from both. The field map resulting from two adjacent current dipoles is more diffused compared to that from single dipole, so that the imagined current dipole is located deeper compared to the two real current dipoles in the radial direction and between them in the tangential direction. The depth of the fitted dipole depends on the actual depth, orientation and relative strength of the current dipoles and the distance between them. Without a full knowledge of the real dipole configuration, the displacement taking place during dipole fitting is impossible to evaluate correctly. Because of the relative short distance between area 1 and area 3b and their shallow locations, the possible displacement of the current dipole may be smaller than the imaging resolution of fMRI studies. The possibility of an insignificant MEG signal coupled with obvious BOLD contrast does exist. The MEG detection is only sensitive to a large amount of synapses acting synchronously, while the BOLD contrast reflects the accumulated effect of neuronal activities. A sustained weak continuous stimulation in respect to the neuronal activity can result in an activation only detectable by fMRI. This situation could be reversed, with a transient strong stimulation which may result in neuronal activity only detectable by MEG. The disappearance of Brodmann's area 1 in MEG studies is a mixture of the above factors, although the degree of dominance of each factor is impossible to identify.

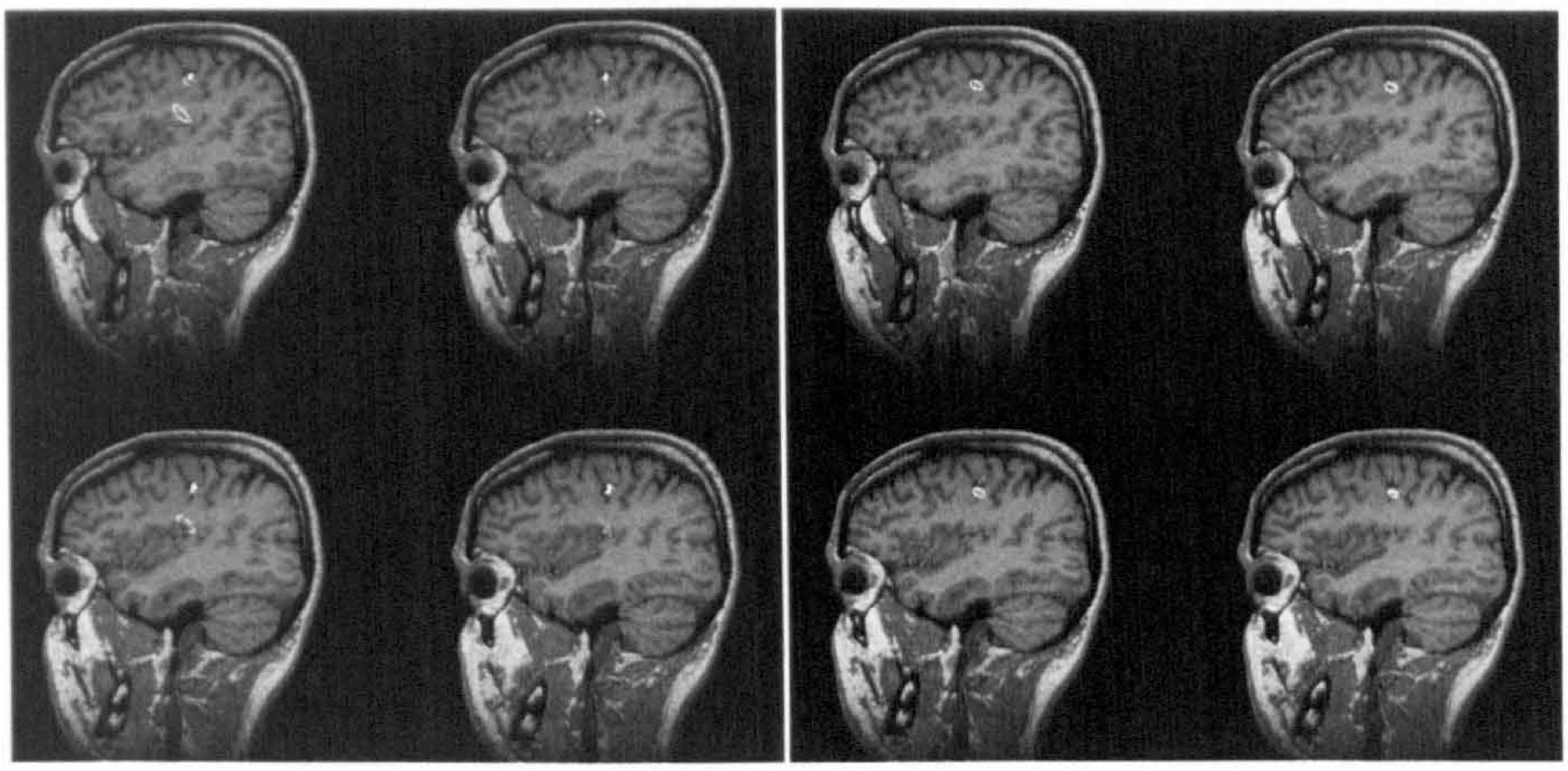

(a) Digit 2, 200 Hz (b) Digit 5, 200 Hz

Figure 5.7: The pictures show the fMRI clusters (red) and MEG ECDs (white) reflecting corresponding regions derived from same stimuli applied to different fingers.

The regions corresponding to Brodmann's area 3b, detected by fMRI and MEG, are in good agreement, with a spatial displacement less than $15mm$. The fitted dipoles are located deeper than the cluster observed from fMRI. Since Brodmann's area 3b is an extended area, the synchronous activation in this region produced a more diffuse field map than an ideal single dipole scenario. The error in dipole depth is therefore easy to interpret, and reasonably matches the extent of individual finger representation in Brodmann's area 3b. In addition to this close agreement between the absolute activation coordinates detected from fMRI and MEG, the relative separation between the cortical representations of digit 2 and 5 also showed a close and stable match between the two modalities. The capability of fMRI and MEG to reveal similar patterns is conformed.

Within the secondary somatosensory area, fMRI revealed activation clusters at both $40Hz$ and $200Hz$, whereas the current dipole can only be localized with the $200Hz$ stimulus. This is possibly due to the fundamentally different receptor projection of the secondary somatosensory cortex, and the relatively low sensitivity of the receptors to low frequency vibration. Despite the existence of neural activity induced by the low frequency stimulus, the signal sensed by MEG is small with regard to the noise and resulted in an unresolved field map. The fMRI studies showed two activation clusters in close proximity within the secondary somatosensory area, while only a single current dipole within the same region was derived from MEG studies on the $200Hz$ stimulus. The fitted dipole is much deeper than the activation clusters observed in fMRI. This depth mismatch is likely to be the result of modelling two separate neuronal activities as a single current dipole. As before, the field map generated by multiple neuronal activity sites presents a more diffuse pattern and leads in the fitting process to a single current dipole of great depth.

The complementary relationship between fMRI and MEG is self evident (Fig 5.7, Fig 5.8), enabling a more complete picture of neuronal processes to be achieved than ever before.

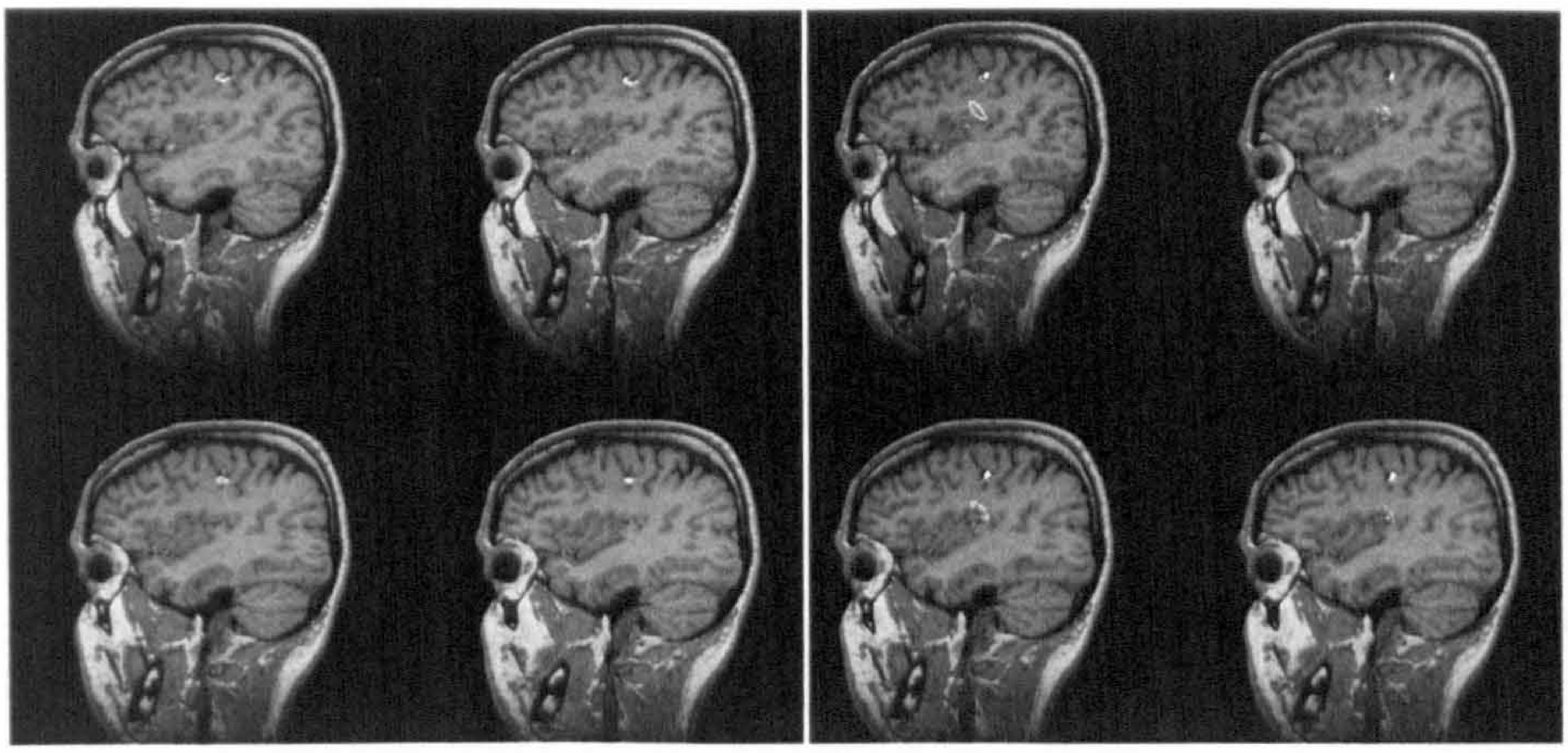

(a) Digit 2, 40 Hz (b) Digit 2, 200 Hz

Figure 5.8: The pictures show the fMRI clusters (red) and MEG ECDs (white) reflecting corresponding regions derived from different stimuli applied to the same subject.

In conclusion, the spatial capability of fMRI and MEG conform to each other at the cortical level, where broad cortical regions can be matched in fMRI and MEG measurements. However, this agreement cannot be extended to the subcortical representation, where similar neuronal topography is unlikely to be revealed in both modalities.

5.5.2 Analysis of Errors

The co-registration of fMRI and MEG involves a series of complex transformations, indicating a high possibility of accumulated errors in spatial comparison. These errors directly affect the validity of the conclusions drawn in these studies.

As an imaging technique, fMRI monitors the spatial location of the subject throughout the experiment. Under the assumption of no sudden movement from the subject, the motion artefact presented between the slices of the same volume can be neglected. The *Automated Image Registration* (AIR) algorithm is capable of correcting for reasonable movements of the subject during the experiment. It does require the cooperation of the subjects. The unresolved image displacement is generally well below the size of a single voxel. The mapping from fMRI images onto anatomical MRI images is a purely computational graphic manipulation to minimize the difference between two images via any possible linear means. As for the motion correction step, the algorithm can be refined to have an error much smaller than the size of a voxel. Therefore, the activation clusters mapped onto anatomical MRI images from fMRI images are expected to possess an uncorrectable error of $2mm$ at maximum. This error is so small that gives fMRI the reference position in this study.

In contrast to fMRI, MEG is incapable of monitoring the position of the subject during the experiment, but instead only acquires the position of the subject at the start and end of each experiment. The movement of the subject during the experiment is therefore impossible to assess and correct. A maximal displacement of $5mm$ was setup as the screening parameter to exclude experiments with excessive movement, while the employment of constraints resulted in a general displacement of less than $2mm$. The position of the reference coils needs to be digitized to allow the registration, which did not take place in the MEG system. The inevitable movement of the subject from the MEG system to the digitization equipment may cause the change in relative position of reference coils to the head of the subject. With careful removal of constraints and caution over other potential movement, this displacement was so small that the assumption of no displacement can be made. The position of the reference coils and the shape of the subject's scalp were sampled with the assistance of a bite bar. Under tension, the bite bar may deform and induce errors. Two sets of these auxiliary data were acquired on the same subject to assess the potential error involved in this step. The displacement between two sets of reference coil measurements is sufficiently small to be neglected, indicating the average of measured positions are sufficiently accurate. (Fig 5.9)

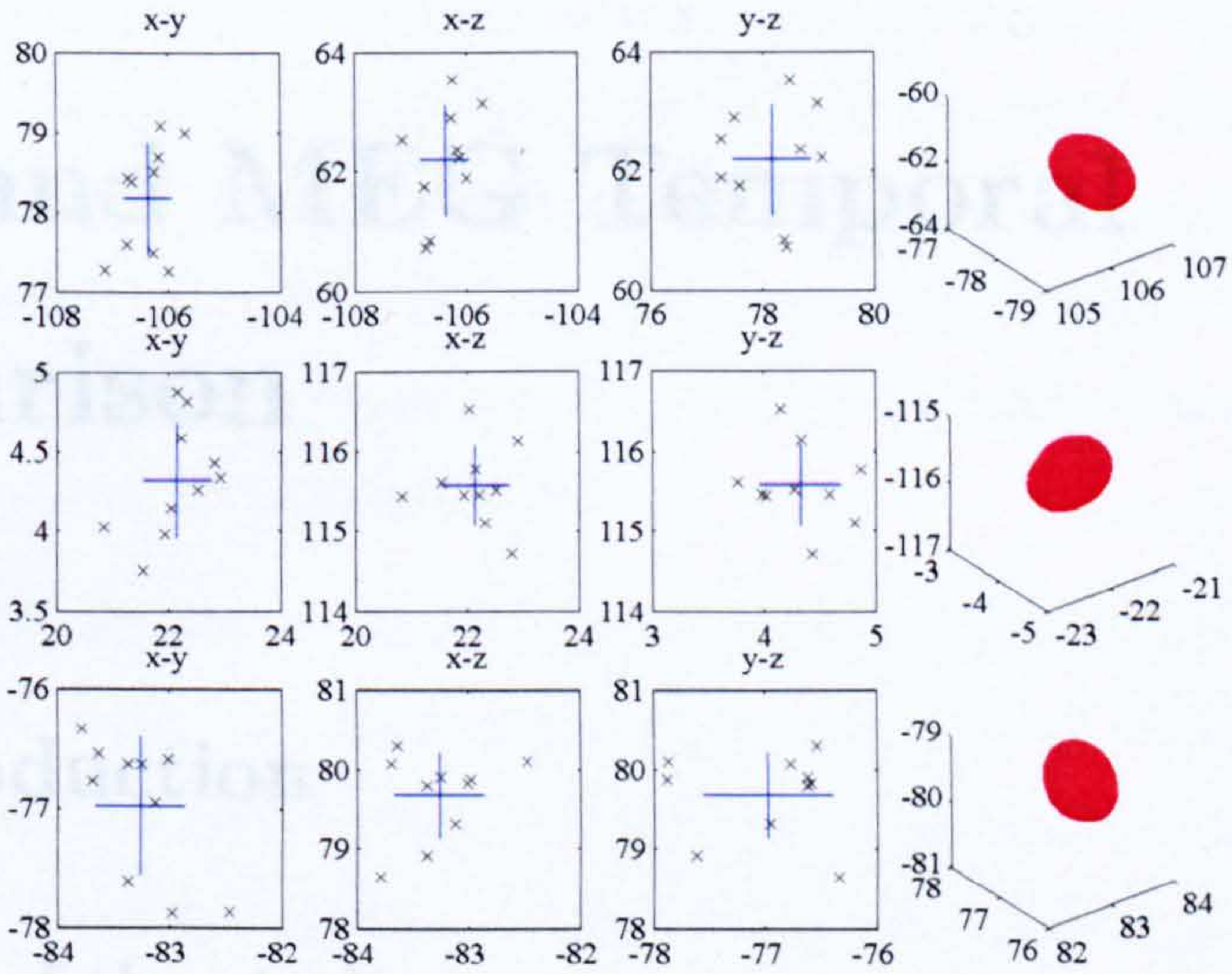

Figure 5.9: The scatter plots and standard deviation ellipsoids of ten repeated sampling of three reference coils. It can be appreciated that standard deviation is well below 1mm in any direction, with all the samples in a near Gaussian distribution manner

Chapter 6

fMRI and MEG Temporal Comparison

6.1 Introduction

6.1.1 Aim of the study

The mechanism of human brains is encoded in both the architecture of this complex processor and the flow path of the information. In this sense, the static platform and the dynamic information both contribute to a comprehensive understanding of its functionality. Since the structure reflects the functions, a complete knowledge alone of the human brain formation would be sufficient to reveal its mechanisms. However, the large quantity of information and the dynamic development of the brain determines that this full knowledge can never be achieved. Even if a full description of brain structure were available, it is sufficient to create disorientation in the exploration, and leading to a specific case study rather than the better understanding of general brain functions. The knowledge of processing procedures therefore shows irreplaceable value on the way towards the construction of a complete picture of brain functions. Implications can be derived and tested on the level of brain functions, as well as the supporting infrastructures. It is undoubtable that this temporal related information should be adopted as the main measure in disclosing brain dynamics, with solid anatomical knowledge of neuronal projections.

In accordance with these apparent advantages, further gains in thorough understanding brain functions are possible by analyzing the temporal information from different research modalities. Since different modalities often reveal different aspects of brain activities, the immediate benefit of comparing different modalities temporally is apparent. Further analysis can also disclose the relationship between different infrastructure systems involved. While fMRI detects hemodynamic change induced by the metabolism requirement of brain activities, MEG senses neuronal electric activity coupled with flow of information. Combination of fMRI and MEG can therefore provide precious knowledge on the relationship between metabolic and electric functions.

Despite all the attraction offered, difficulties and obstacles do appear at a more fundamental level. Because of the close proximity of signal sources for fMRI and MEG to the actual brain activity region, the spatial representations of fMRI and MEG can be regarded as the direct approximation of the neuronal activities. Built on this foundation, the spatial combination of fMRI and MEG has solid ground with readily interpretable results. However, the detected signals generated from fMRI and MEG are both geared by many underlying factors, whose relationship to the neuronal and internal interactions are far from full disclosure. This situation asserts the fact that all the available approaches are either data driven model or mechanism postulated model. This ultimately puts doubts on the validity and correctness of the modality combination algorithm, in spite of possible quantitative match.

It is possible to recognize the temporal precedence of brain regions involved in the activity by correlating the fMRI clusters with MEG dipoles and their corresponding response peak time. However, the spatial correspondence between fMRI and MEG is not fully resolved as discussed in the previous study. Since MEG peak responses are the result of synchronized activity of a large amount of synapses in a localized space and time, its representation of the temporal characteristics of brain activities is reasonably coarse. This type of partial knowledge may not only prevent correct understanding of the information processing procedures, but also mislead to faulty findings. It is therefore suggested that the spatial knowledge is only adopted as the safeguard against artifacts rather than the active constraint of the processing. This study concentrated only on the MEG recording on somatosensory cortex activated by tactile stimulus, to explore the feasibility of abstracting the information from MEG to match a well known fMRI time scale. Both adaptive linear decomposition and time frequency analysis were adopted in a hope to expose the aspects of MEG to serve as a correlate to fMRI with justified physical meaning.

Since the metabolic demand of brain is maintained at a certain level in the resting state, there is a possibility that the dominant change in metabolic requirement comes from reorganization of the neuronal network. In this study, this hypothesis was probed by adopting linear decomposition and wavelet analysis. The linear decomposition method [105] has been applied to MEG measurement in the past mainly for noise reduction and artifact rejection, while wavelet analysis [106] has been used to assess brain oscillations. The joint application of both techniques might expose the neuronal network reorganization features.

6.1.2 Neurocortical Network Connections

An accurate picture of the dynamics of brain functions requires an detailed knowledge of brain anatomy as the foundation. The physical links between different brain parts and even the substructures of the same area need to be greatly understood, as well as their possible functions.

Once reaching the brain, the somatosensory system projects to the thalamic *ventrobasal* (VB) complex. The sensory input terminates on the *ventroposterior* (VP) nucleus, where the inputs from the body project to the lateral subdivision (VPL), and those from the head to the medial subdivision (VPM). The projection of neuronal input to VPL shows a functional division, in which the core region dominantly receives cutaneous inputs and the shell region mainly for deep tissue inputs. The VB therefore faithfully represents the somatosensory inputs from all around the body in a small complex.

The higher processing centre of somatosensory cortex is divided into *primary somatosensory cortex* (SI) and *secondary somatosensory cortex* (SII) . The primary somatosensory cortex is located in the posterior bank of the central sulcus and on the crown of the postcentral gyrus, while the second somatosensory cortex sits on the lip and upper bank of the lateral fissure. Both areas receives projection from VB, as well as a dense projection from each other. Subsequently, they send projection to other somatosensory system in the parietal lobe and insula, as well as the areas of the motor cortex.

SI is further divided into four areas, Brodmann's areas 3a, 3b, 1 and 2, where each area receives direct inputs from VB. Since neurons in VB rarely sends two collaterals to two areas in SI, the physiological properties of neurons in one area differ appreciably from those of other areas. It is found that neurons in areas 3b and 1 are responsive to cutaneous stimuli, while the areas 3a and 2 responding to inputs from deep tissues, such as muscles and joints respectively. From lesion studies, it was concluded that area 3b is the conduit of all cutaneous sensibilities. Area 1 is in charge of the texture recognition, while area 2 integrates the knowledge of limb position with the edge detection to form the perception of the shape of an object. Cerebral cortex of SI generally present six layer structure, where axons arising from neurons in one layer terminate upon neurons in another layer. Neurons are organized in a column architecture in a true radial path through different layers, maintaining space and modality specification. Area 3b receives dense innervation from the core region in VB, taking place in the layer III and IV. Neurons in layer II and III of area 3b subsequently relay inputs to layer IV of other areas in SI, termed feed forward. This gives the implication that the fundamental parallel processing of somatosensory system is manipulated by the serial processing. The receptive fields presented in the layer IV of area 3b is similar to those of peripheral afferents, while layers II and III show more complex receptive fields with presence of distinct excitatory and inhibitory subregions. The output from layer II and III is relayed to area 1 to construct receptive field with properties of texture recognition. The projection from area 3b to area 2 conveys the cutaneous information to the present knowledge of joint position to establish the shape of the object in mind. Area 3a is located between the precentral motor area and area 3b, receiving dense innervation from the parietal association cortex and the supplementary motor area. Projections from VB into area 3a are mainly responsible for the prioceptive stimuli arising from muscles. Projections from area 3a terminates on area 2 and area 5 located in parietal association cortex, from which sensory information reaches precentral motor and premotor area. It is therefore can be recognized that area 3b is an intermediate stage of somatosensory processing. Their cortical projections to motor and association areas provide evidence that areas of SI integrates somatosensory information and to relay such information to areas that control and coordinate body and limb movement. In addition to this, SI also projects to SII and surrounding cortex as well as several subcortical structure. These subcortical structure are mostly a part of the somatosensory system already, forming the descending control pattern. The function of descending control is under intensive investigation, with the current accepted theory of attentional influence. This attentional mechanism within the somatosensory context serves as to selectively activate neurons that are processing information from a specific body location and modality. It is therefore easy to understand that the response in SI is influence by the attentional status that can be due to the previous activity of the somatosensory cortex.

The *secondary somatosensory cortex* (SII) , approximately occupying one fourth the size of the SI in cortical surface, receives direct projection from VB with neurons responsive to cutaneous stimulation of low intensity. Destruction of SII results in incapability of discriminant objects on the basis of texture and impairment in discriminating objects based on their size. The neuronal projection from both sides of the body surfaces reaches the SII of both brain hemisphere. Inputs from the ipsilateral body surface reach SII predominantly through the corpus callosum from contralateral hemisphere. The function of this transcallosal input can be summarized as midline fusion and knowledge cross hemisphere transfer. Since the two sides of the body surface project to different side of the brain, the midline fusion allows the coherent perception of a single body map. The knowledge cross hemisphere transfer enables a tactile discrimination task learnt by one side to be easily and quickly performed by the other. SII is also the recipient of inputs from all the four areas of SI, with dense intracortical axon termination on layer IV in each case. Subsequently SII innervates two adjacent areas of insular cortex, from which somatosensory information reaches the amygdala and hippocampus. It is therefore can be recognized that SII is vital as the obligatory route taken by sensory inputs mediating tactile learning and memory. Attentional mechanism heavily influences the behavior of SII, since more than 80 percent of the neurons in SII are directly affected by the attentional status.

Apart from SI and SII, posterior parietal areas, parietal cortical area posterior to area 2, also play an key role in the processing of somatosensory information. The rostral part of this area consists area 5a and 7b, both receiving direct innervation from area 2and projects to precentral motor area. It is therefore evident that integrating of somatosensory information with motor behavior, especially the attentional and motivational control of movements related to tactile stimuli, take place in these areas. The caudal part of the posterior parietal cortex accommodates the convergence of somatosensory and visual inputs, with the visual function of localizing and directing attention to a stimulus. It was shown that this area is involved in directing eye movements, implying its pivot position in somatosensory, visual and motor system.

6.2 Theory

6.2.1 Attention and Brain Waves

Although human brain consists of huge amount of neurons forming complex connections, the full appreciation of even some simple stimuli and their environmental implication may result in a significant processing time. Following long term evolution and development, human has accumulated a substantial amount of neuronal processing capability. However, in a natural evolution and selection procedure, sufficiency can never be achieved in spite of abundance. This is especially obvious in emergency, while marginal advantage can determine the outcome of a fatal situation. The solution introduced by the evolution is a biased processing mechanism, which effectively and efficiently concentrates available resources on one or several tasks. This mechanism is commonly known as attention, with the feature that alarming stimulus can still be processed and responded to. The effect of attentional selection may be achieved by many different systems via various mechanisms, appearing as a seamless function of allocating neuronal resources.

Although attentional selection is involved in all the levels of the medial nervous processing, it is most obvious in cognitive and psychophysical studies. Those studies well expose the limitation of brain of the neuronal processing capacity, revealing the need of dealing certain tasks at the expenses of performance on other simultaneous activities. The attentional selection exhibits influences on very primary levels, as well as its obvious effects on higher order processing. It was found that an increased in the firing rate was coupled with the direction of attention towards the stimulus. It was shown that the neuron did not respond to a very faint stimulus, regardless of whether it was attended or not. A slightly higher contrast stimulus also did not elicit a response when it was ignored, but elicited a clear response when it was attended. A very high contrast stimulus elicited strong response whether or not it was attended. It is therefore can be recognized that the effect of attention is to increase the sensitivity of the neuron to stimuli, enabling it to detect a stimulus that was too weak to elicit a response. By increasing neuronal responses, attention enables neurons to send signals that better differentiate between stimuli with different physical characteristics. Since two nearby stimulus can activate largely overlapping neurons, the presence of attention can increase the reliability of separating nearby sources.

These functional phenomena are the direct result of underlying complex neuronal organization. It has been show that the receptive fields of individual neurons might contribute to the limitation in neuronal processing capacity. This also matches the philosophical analysis of attention, because the change in receptive field implies the change in distribution and deployment of neuronal processing power. It also consolidates the need of attentional selection mechanisms, since neurons limited in bandwidth cannot simultaneously send signals of all of the stimuli inside their receptive fields. It is therefore understandable that neurons with large receptive fields, such as those in higher order structures, are influenced more pronouncedly by attention.

To facilitate the change in receptive fields, the transmission of neuronal signals follows the competition and bias principles. Competition occurs when several neuronal inputs are preparing to recruiting the same circuit, whose resolution determines the passage selection between the inputs. The outcome of this competition is not only determined by the strength of each input, but also the bias imposed from other neuronal processing and physical connection. This bias principle acts as the attentional selection mechanism, where other neuronal activities influence the deployment of processing neuronal circuits. The bias can be the result of configuration left by previous similar process or brain activities of other nature and modality.

The completion of attentional selection relies on the maintenance of a certain level of alertness. The level of alertness is mediated by several pathways originated in the brain stem employing special neurotransmitters. The presence of these neurotransmitters modulates the response of neurons to normal neurotransmitters. The overall alertness affects the degree of spontaneous brain activity, and subsequently the signal to noise ratio of the signal processing.

To facilitate the attentional selection, neurons has formed complicated networks, both in small and broad scale. The competition and bias are achieved by dense synaptic connections, via which excitatory and inhibitory bias and strength evaluation between inputs can be made. The activities in the neuronal circuits expose the nature of the nature of the network as brain waves. This may be represented as a unique network frequency, or neuronal synchronization or desynchronization. However, the logistics of neural networks is still of great uncertainty.

6.2.2 Blind Source Separation

Observations of a physical system are via the measurement of a set of signals over a time period. Similarly MEG detects the magnetic field field strength at sensors distributed over the head during the experiment. In the same way as most natural recordings, the signal picked up by a single MEG detector is a mixture of many underlying factors. Each sensor provides such a mixture; a multi channel MEG system gives an account of the underlying factors with different proportions to each sensor time course. In this sense, a mathematical problem can be formulated as resolving the time varying underlying factors based on the gathered mixtures.

Unfortunately, a mathematical solution to the above problem is impossible, without ample knowledge of mixing procedure. With the assumption that each source signal has a defined constant portion of a sensor detected signal, a linear mixing procedure can be reached, and is given by

$$\mathbf{Y} = \mathbf{M}\mathbf{X}, \tag{6.2.1}$$

where $\mathbf{Y}$ is the measured signal matrix, $\mathbf{M}$ the mixing matrix and $\mathbf{X}$ the source signal matrix. The signal matrices are organized in a way so that each row corresponds to sensor or source time course, while each column represents a time snapshot of all the sensors or sources. This assumption can be easily satisfied by most MEG observation, since the theory of lead field and superposition theorem ensures the validity of this constraint. However, exceptions can still take place, where the source does not remain stationary in the sensor space. This can also be encountered when modelling the activated cortex as a single source, although in most cases it can be approximated as stationary. Based on the assumption of linear mixing procedure, the mathematical problem of blind source separation can be written as searching for an unmixing matrix $\mathbf{W}$ capable of transforming the mixture $\mathbf{Y}$ into source signals $\mathbf{X}$ by

$$\mathbf{X} = \mathbf{W}\mathbf{Y}. \tag{6.2.2}$$

This problem is still unsolvable without the assistance of the characterization of the difference between mixtures and sources. Since the mixture signals are composed of many sources, the independence between different sensors is limited. On the contrary, each source signal contains unique information. Pursuing the sources is therefore equivalent to seeking the independent components. The analysis following this strategy is subsequently named *Independent Component Analysis* (ICA). It can also be found that the mixture signals often present a *probability density function* (pdf) of Gaussian distribution, while source signals often exhibit super or sub Gaussian distribution. The difference between source and mixture signals is further reflected by the complexity of the temporal structure, where sources and mixtures correspond to low and high complexity respectively.

Based on above descriptive statements, mathematical representation can be formulated to maximize or minimize each feature, result in different ICA approaches. The linear transformation from source signals to mixtures, can be visualized as stretching the orthogonal source space into a sheared space, with mixture axes defining the new orthogonal space. It is therefore possible to reconstruct a source signal from mixtures by applying a weight vector, whose direction is orthogonal to all the other transformed source signal axis. According to the statement above regarding the normality characteristics of the source signals, it is possible to find a weight vector to extract a signal with maximal non-Gaussian distribution. This strategy is called projection pursuit, simply because it searches for an ideal projection to maximize the non-normality of the extracted signal. The method is iteratively repeated to find sources one by one, with assistance of deflation procedures. The mathematical measure of normality is named kurtosis, and is given by

$$K = \frac{E[(y - \bar{y})^4]}{(E[(y - \bar{y})^2])^2} - 3, \tag{6.2.3}$$

where y represents the extracted signal with a mean value of $\bar{y}$, and $E[x]$ stands for the expected value of x. The value of kurtosis can be positive, zero and negative corresponding to suer Gaussian, Gaussian and sub Gaussian distributions. Approaches can also originate from the fundamental independence assumption, while two main explanatory strategies, namely infomax and maximum likelihood methods have been developed. The infomax account shows that the independent sources are achieved by maximize the information flow or entropy of a neural network. It can be shown that this neural network resembles the cumulative density function of the extracted source signal, via which a probability density function match can be achieved between model and the decomposed signals. Based on the assumption of the probability density function of the source signals, the probability of finding the mixtures can be calculated corresponding to each mixing matrix. Following the maximum likelihood description, the actual detected mixtures should hold the maximal probability. It is therefore possible to adjust the mixing to satisfy this condition. Both infomax and maximum likelihood reach same result, with advantages of multiple source extraction and a more specific source description over projection pursuit. Complexity can be used as another criterion os discriminating source signals from mixtures. A source signal possesses less complexity than mixtures, which can also be interpreted as that the source signal is more predictable. This assumption is generally true, since most physical system are unlikely to exhibit abrupt changes. Complexity can be mathematically represented as Kolmogorov complexity, allowing the minimization to take place. The complexity based ICA decomposition is least used in the current research world.

In most cases, all the ICA approaches derive the same result based on same assumptions. Although differences do present between statistical independence and the independence in common sense, the results from ICA are mostly in line with the observation. Therefore ICA is regarded as a precious tool to reveal the nature of complex systems.

In practice, the recorded MEG data is organized into a channel-time two dimensional matrix. To reduce the computational demand, PCA is performed on this matrix to reveal the desired principle components within the data. Each component is given in the same amount of time points to represent the strength of each component in time, where a weight array, with the dimension of the number of sensors, is also achieved to indicate the strength of the component on each MEG sensor. Subsequently, ICA exposes the independent components of the data in the same format as the results from PCA.

6.2.3 Time Frequency Analysis

Physical measurements made on any system are fundamentally in a domain constituted by space and time. To restrict the analysis of the observations in this domain restricts the chance of better understanding the nature of the phenomenon. The development of mathematical tools provides an alternative view of conventional phenomena that can expose their true nature. To achieve this, raw signals are decomposed into spaces matching natural features of the signal, in which a central or dominant component accounts for the main feature with peripheral components describing marginal features.

Basic physical exploration of the world emphasizes the behavior of systems in a stable condition. This stable condition can be time invariant or periodic. For time invariant signals, the analysis in real time space is general sufficient. Although the real time domain can be seen as an indefinite orthogonal space, this does not provide further insight into the nature of the data. Because the time invariant signals are equivalent to a constant periodic function, all the stable signals are composed of Fourier atoms, which form the orthogonal basis of frequency space. It is then possible to analyze the response of a system towards a single component and in turn the collective reaction towards to full signal. Fourier atoms constitute a complete orthogonal basis and any signal can therefore be decomposed into the frequency domain. The mathematical representation of Fourier transformation is given by

$$F|f\rangle_t = |f\rangle_\omega, \tag{6.2.4}$$

where F is the Fourier transform operation, $|f\rangle_t$ and $|f\rangle_\omega$ are the function expressed in time and frequency representation respectively.

Although the analysis of stable systems provides a precise approach to unlock the nature of the world, it is unfortunate that a stable system nearly does not exist in practice. The world is full of dynamic phenomena, and nature certainly devised most systems, in particular biological systems, to respond more effectively to short term or transient information rather than stable conditions. To address the need of a mathematical tool to grasp the essence of this type of process, the *Short Term Fourier Transform* (STFT) was first constructed. An STFT analysis is a procedure of applying a window weight function on the signal to extract a portion of the signal. The frequency components are then revealed by the application of Fourier transform on the extracted signal. By sliding the window weight function through time, the frequency components for each time point can therefore retrieved. Following this, the dynamics in the frequency domain are available. The window is further phase adjusted for each time frequency point, so that the window is centred at that point both in time and frequency domains. Since the Fourier transform is formulated based on an infinite continuous signal model, the application of the window weight function results in a blurring effect determined according to convolution theory. Based on the same window width in time, the width of the window in frequency domain is larger at low frequency and smaller at high frequency. This in effect indicates that the resolution of the time frequency window is not unform, since accurate time and frequency values cannot be known simultaneously (as stated by Heisenberg's uncertainty principle). To allow the observation of a unform resolution in the frequency domain, the width of the window function is adjusted according to the processed time point, so that the width of the function in frequency is constant throughout the analysis. Unfortuantely, the implication of this method is that the resolution in time varies for different frequencies.

The above windowed analysis can be viewed as a type of wavelet transformation, since the window function can be viewed as a wavelet function. Simply by using scale, a reciprocal version of frequency, the dynamics of a signal can be expressed in time sclae space with uniform resolution. Subsequently, each atom of the wavelet is a spatial basis for decomposing the signal. However, these bases are not necessarily mutually orthogonal, depending on the applied window function. With a robust wavelet function, all the atoms form a complete orthogonal basis, which allows a full decomposition and reconstruction of the signal. Non orthogonal bases may result in partial information decomposition, and cannot serve to reconstruct the original signal. Different choices of wavelet functions simply establish different orthogonal bases in space, and more readily expose different aspects of the signal.

6.3 Methods

6.3.1 Materials and Stimulus Presentation

This study was carried out on six healthy volunteers aged from 20 to 30. All subjects are right-handed, who are four males and two females. The tactile stimulus was delivered to the right hand of each subject, on digit 2 only.

The stimulus was generated by a piezoelectric sensory stimulator, which had the capability of producing a peak deflection of $400\mu m$ to the finger in the frequency range between $20Hz$ and $300Hz$. The vibration of a sinusoidal oscillation at an amplitude of $150\mu m$ and a frequency at $200Hz$ was applied to the subject. It was proven that the interference of the stimulator on MEG systems was neglectable.

A paradigm of 40 cycles was used, where each cycle was composed of $2s$ baseline, $9s$ of stimulus delivery and $4s$ rest.This design ensures the availability of a reasonable baseline for comparing the activation status against baseline. The lengthy stimulus allows the tracking of the neuronal activity change following a sustained stimulus, and increase the difficulty for subject to predict the onset and offset of the stimulus. It further gives the potential of discriminating the weak neuronal activity from stimulus coupled noise.

6.3.2 MEG Methods

The MEG measurements were performed on a 151 channel whole cortical MEG system, as described in the previous chapter. An inflated pad was made available according to the wishes of the subject. A criteria was set to control the quality of the data with respect to the motion, where a displacement of more than $5mm$ causes the data to be rejected.

The extracranial magnetic field was detected in the third order gradiometer mode. The signal was digitized at a sampling rate of $625Hz$, which is ample to cover the frequency band of most neuronal activities. Once the data was collected, a visual check to make sure no large scale artefact presents in the data. The dataset was extracted to two portions to suit the maximal computational capacity available. The first portion starts from $1.5s$ prior to the onset of the stimulus to $4.5s$ post the onset of the stimulus, while the second portion starts from $4.5s$ prior to the offset of the stimulus to $1.5s$ post the offset of the stimulus. This extraction may also provide certain information regarding the coherence between the two portions. The extracted data were low pass filtered at $45Hz$, through which the power line interference were removed simultaneously. The mean of each channel was removed on the channel by channel basis, and subsequently all the epoches were concatenated following the corresponding channel. Therefore each MEG sensor correspond to a long time course composed by all the time points of this channel during the experiment. Subsequently, a *Principle Component Analysis* (PCA) was carried out on the signal matrix, and the first 30 components were picked out for the rest of the analysis. At the end of this procedure, the computational requirement for the reset of the analysis was significantly reduced, since only 30 instead of 151 channels need to be considered. These 30 channels are mutually uncorrelated to each other following the PCA, and accounted for most observation in the original channel space. Subsequently, ICA procedure based on probability density function matching was performed to derive independent components.

6.4 Results

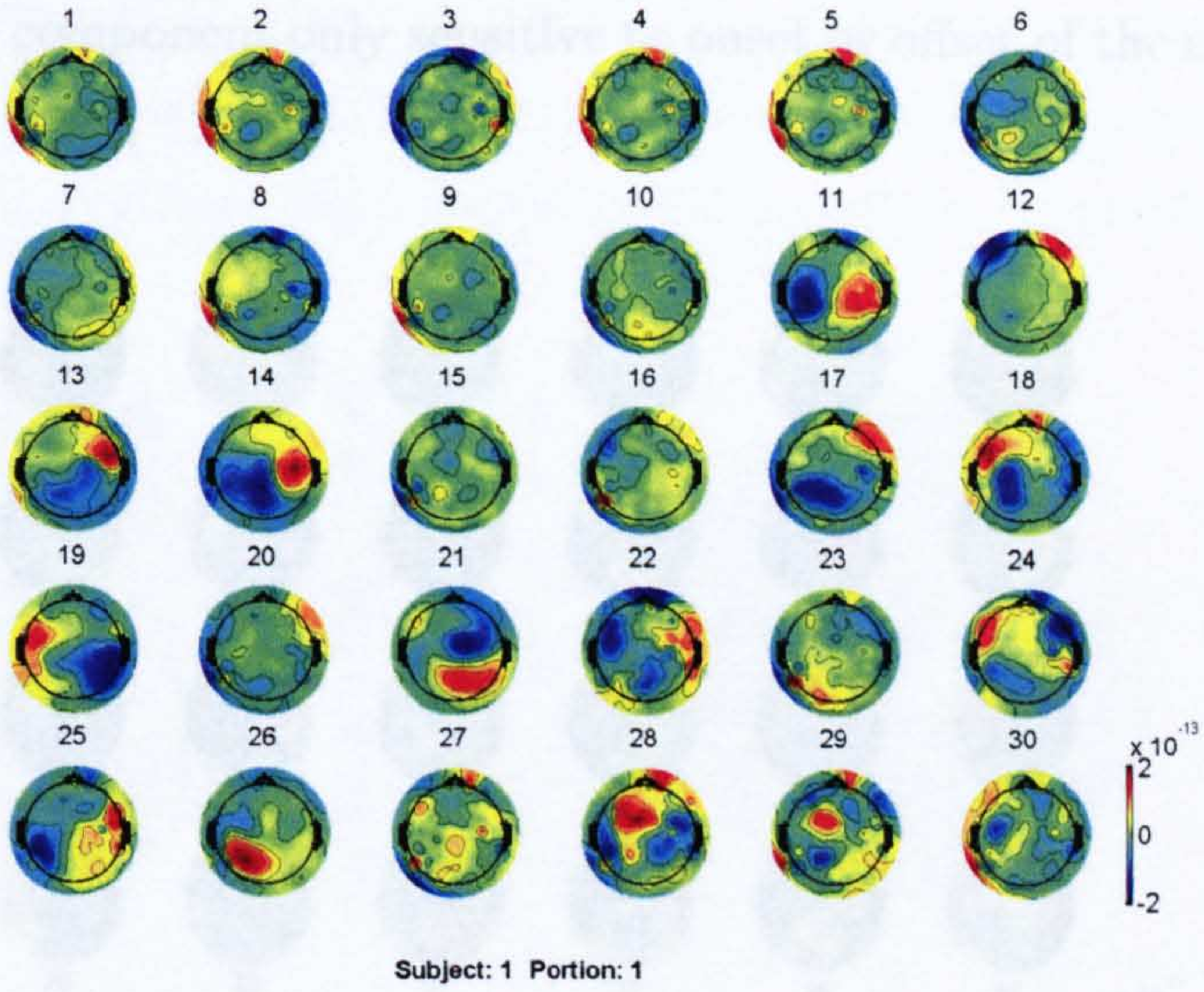

Figure 6.1: The component distribution based on the unmixing matrix of the first portion of the data(1.5 s prior to the onset of the stimulus to 4.5 s post stimulus onset).

Based on the ICA decomposition, the spatial distribution of the extracted independent components were plotted based on the sensor positions, so that a preliminary exclusion of unrelated components can be carried out. A typical display of all the components maps extracted from one data set is shown here (Fig 6.1).

Since the dataset was extracted into two portions earlier in the process, the comparison between these two portions can show the consistency of neuronal behavior. The component distribution found in the other portion related to the above data is shown here (Fig 6.2). The component distribution in both portions is extremely similar both in the component order and distribution profile. The order in the components indicates the level of the component accounting for the total signal variance, while the distribution profile reflects the spatial position and orientation of the underlying source. Since neuronal sources are virtually stationary in well defined regions in the cortex, the component distribution profiles are expected to be similar. Additionally, since the MEG detection is biased by the spatial position of the sources, the relative strength of each component is expected to follow the same order in similar neuronal processes. The agreement between these two portions demonstrates that most components are active in both portions, and component only sensitive to onset or offset of the stimulus are rare or weak.

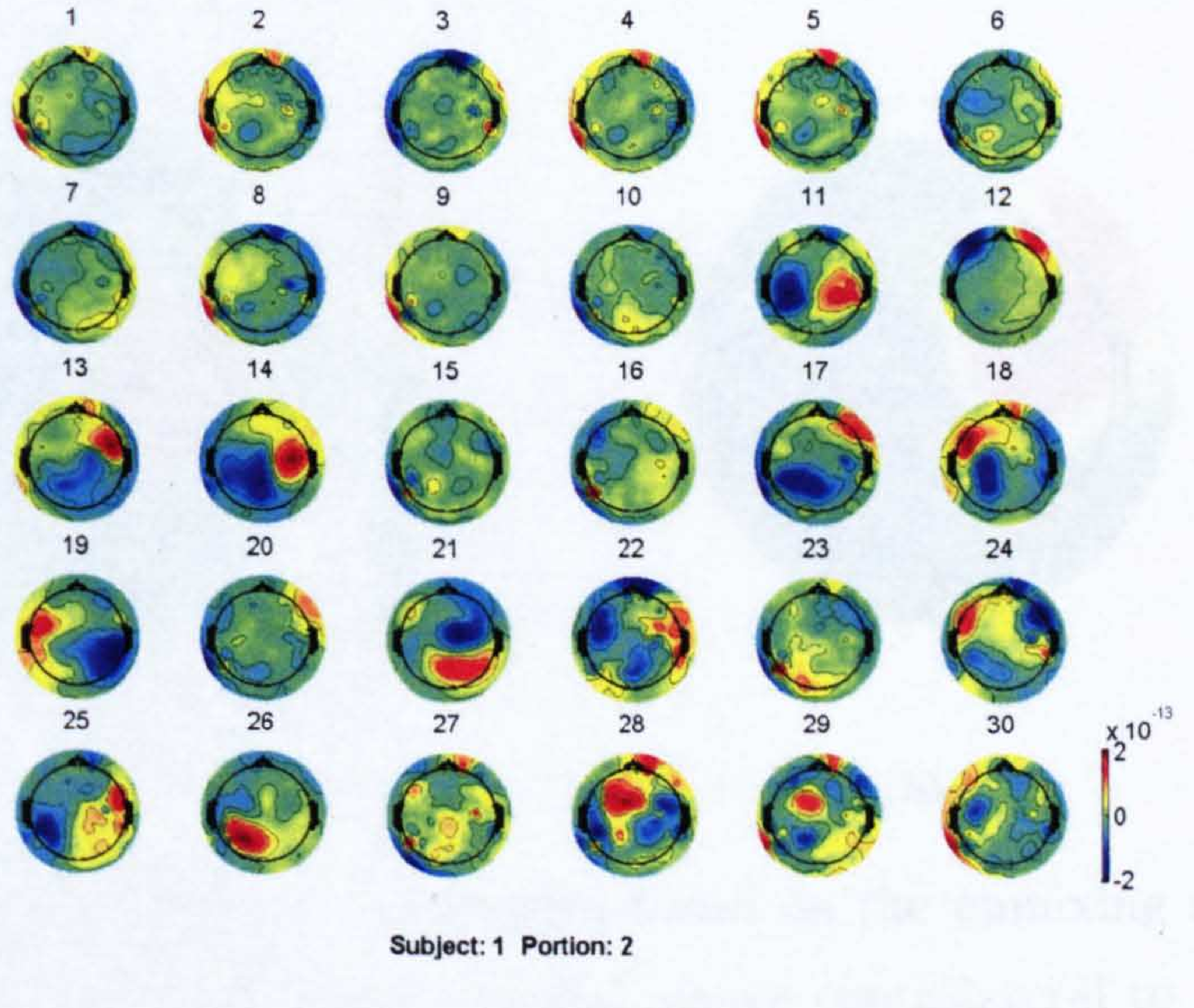

Figure 6.2: The component distribution based on the unmixing matrix of the second portion of the data (4.5 s prior to the offset of the stimulus to 1.5 s post stimulus offset) showing good consistency between two portions.

Although somatosensory processing is perhaps the simplest form of neuronal activity, the number of areas involved is high. This introduces clear difficulty in assessing the behavior of a small region. This becomes apparent when the region of interest is in close proximity to other activation sites, which may induce similar field maps to other regions. Since the somatosensory system is relatively well studied, some a priori knowledge can be used to simplify the situation. Since the delivery of the stimulus directly activates SI, while only SII is responsible for the cross hemisphere talk. The components can be separated by identifying the position of their underlying dipoles. It can be observed that a strong SI (Fig 6.3) source in relative shallow medial position is always present. The activity in SII ipsilateral to the stimulus can either be found on its own (Fig 6.4) or present as joint component as other areas. Since SII has strong influence on attentional status, both stand alone and joint component presence does not however guarantee that SII activity is present. Also SII is regarded as a type of deep source, the capability of identifying SII from background noise is therefore seriously compromised. This is particularly obvious when two deep sources present in the same component, since the diffused field map easily obscures the origin of the source.

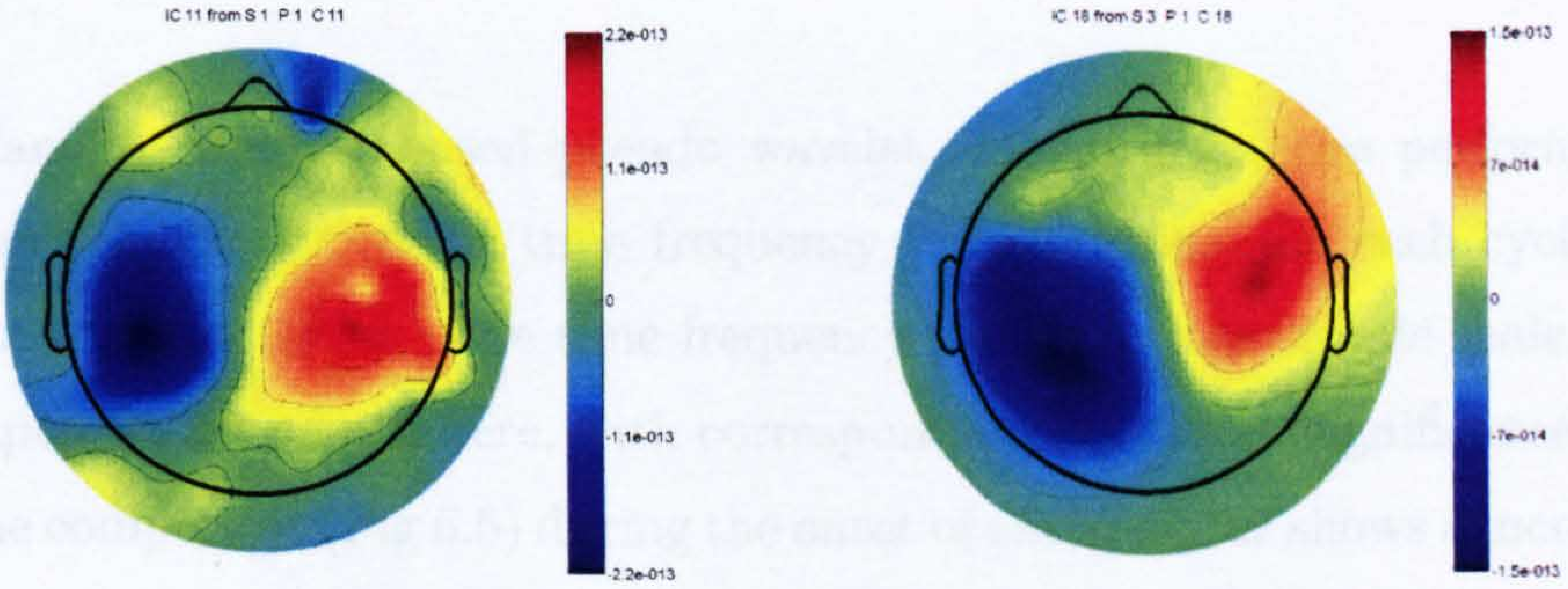

(a) (b)

Figure 6.3: The component distribution based on the unmixing matrix of the first portion of the data showing a medial source contralateral to the stimulus. The source locates relatively shallow in depth according to the degree of diffusion of the distribution map, and is likely to be one part of SI.

It is apparent that ICA is capable of separate different neuronal activity sources based on the statistical feature of the detected signals, while the wavelet analysis can expose the underlying reorganization of neuronal networks. The results shown indicate that the neuronal network reorganization can be a possible underlying factor of the change in metabolical demand. Therefore there is a possibility of having neuronal network reorganization as a close correlate to the BOLD contrast.

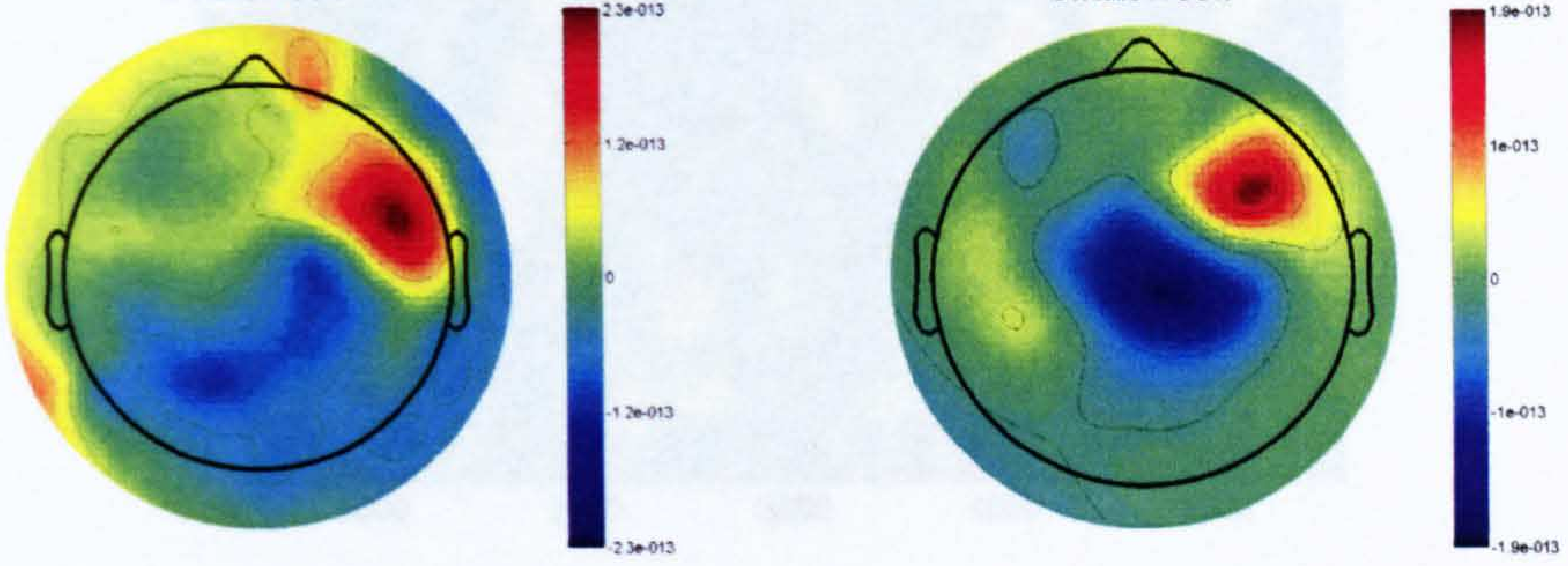

(a) (b)

Figure 6.4: The component distribution based on the unmixing matrix of the second portion of the data. The position of the source is ipsilateral to the stimulus with a deeper and more lateral location. This source can therefore be a part of SII.

A Hanning window based pseudo wavelet transform can be performed on the component to derive the time frequency profile during the each cycle, and average across the cycles. The time frequency profile in logarithmic scale of the two component are shown here, with corresponding Bootstrap significance set to 0.05. The component (Fig 6.5) during the onset of the stimulus shows a increase in power, synchronization, in the frequency band between $20Hz$ and $35Hz$, followed by a power reduction in the same frequency band. It also appears that the low frequency end slowly gains power after the onset of the stimulus. The significance analysis based on Bootstrap confirms the above observation (Fig 6.6). The time frequency map of the second component (Fig 6.7) shows an increase in power of a large frequency band at the offset of the stimulus. It can be seen that during the application of the stimulus this component has relatively low power compared to the strong synchronization at the change of the stimulus status. The Bootstrap based significant analysis (Fig 6.8) confirms the above observation.

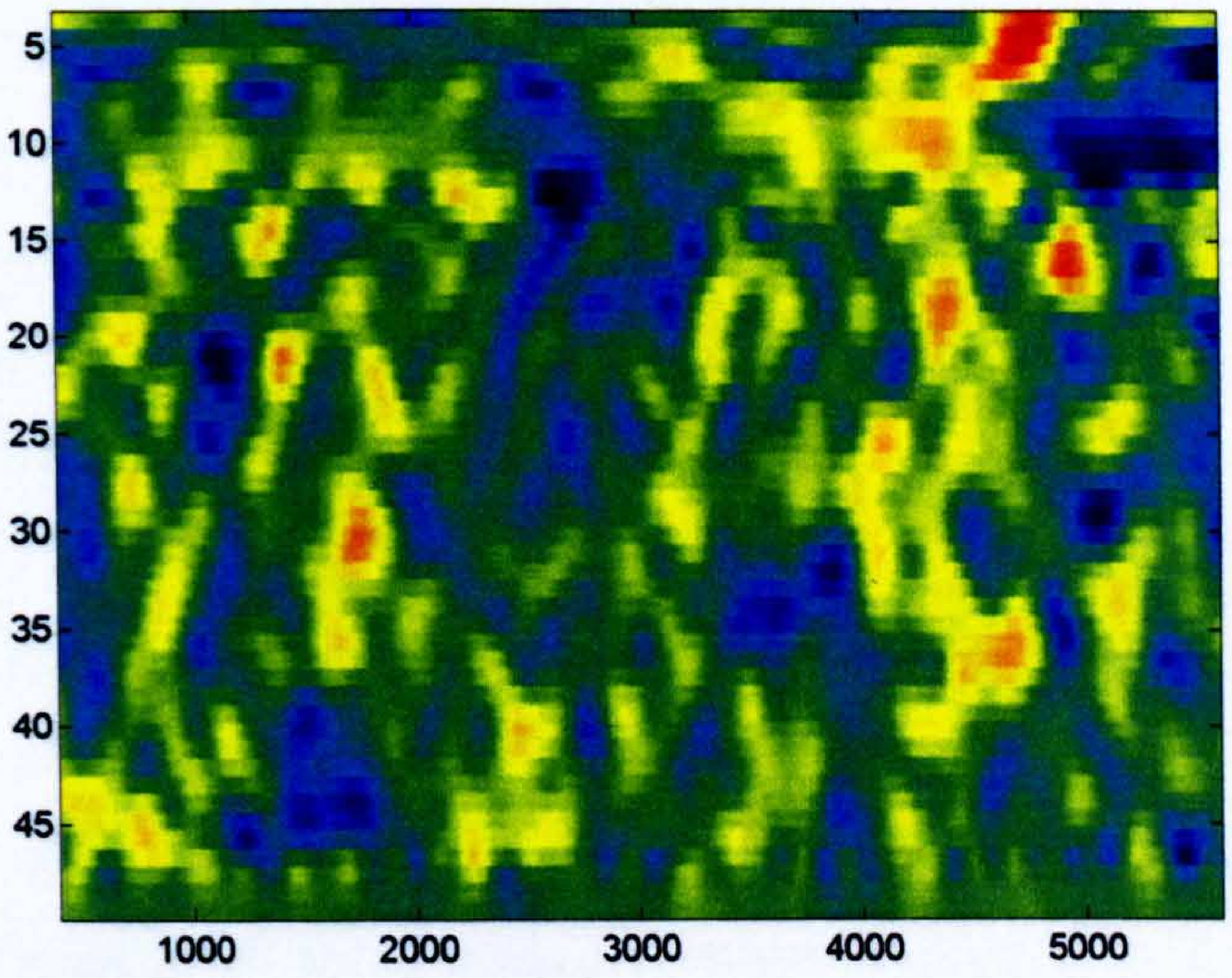

Figure 6.5: The time frequency profile of the first component demonstrated, where the onset of the stimulus is at 1500ms. The horizontal axis stands for time in ms, while the vertical axis is the frequency in Hz.

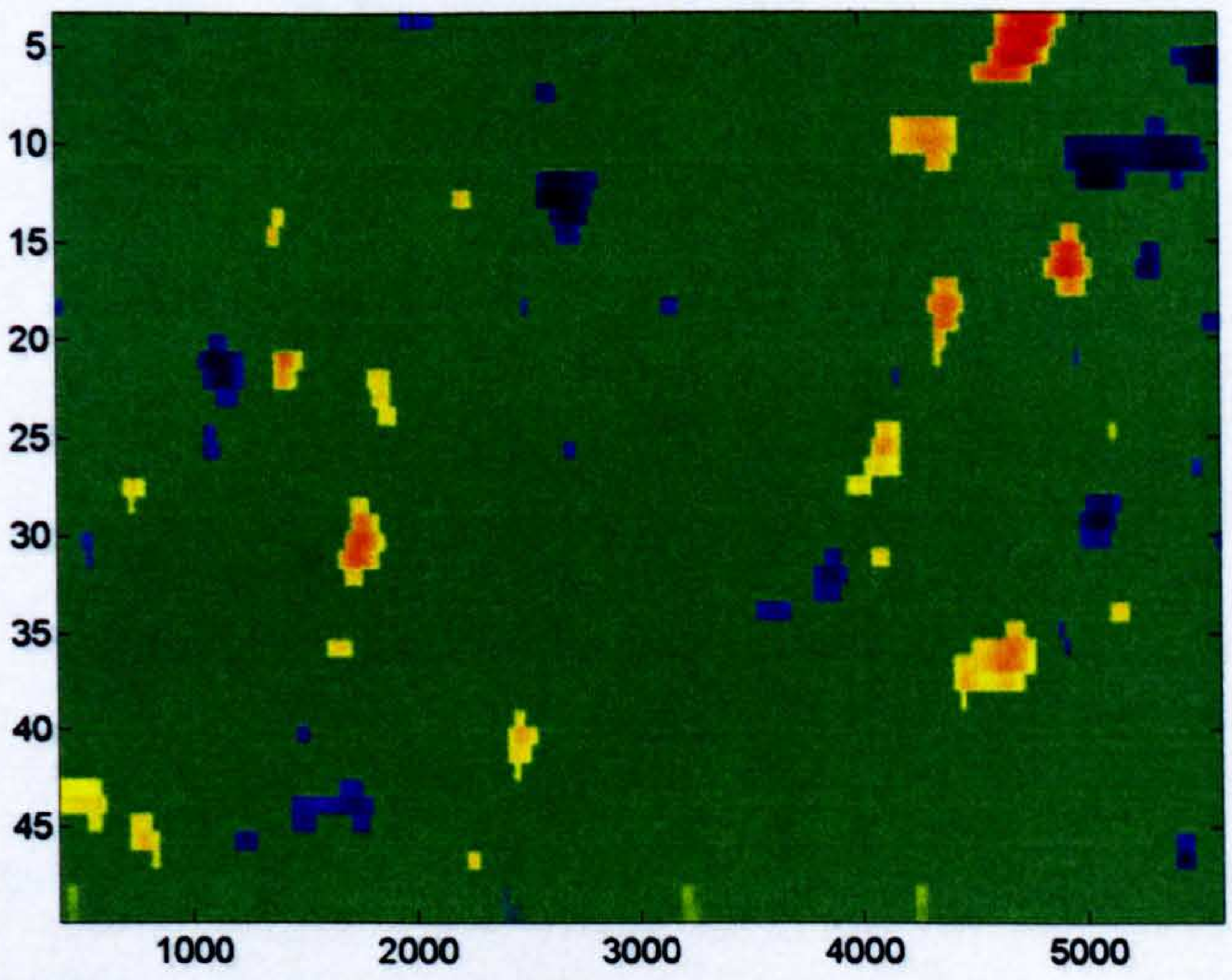

Figure 6.6: The time frequency profile of the first component demonstrated, where the onset of the stimulus is at 1500ms. The horizontal axis stands for time in ms, while the vertical axis is the frequency in Hz. The Bootstrap significance was set to 0.05, with the pixels failing to pass the significance test set to zero.

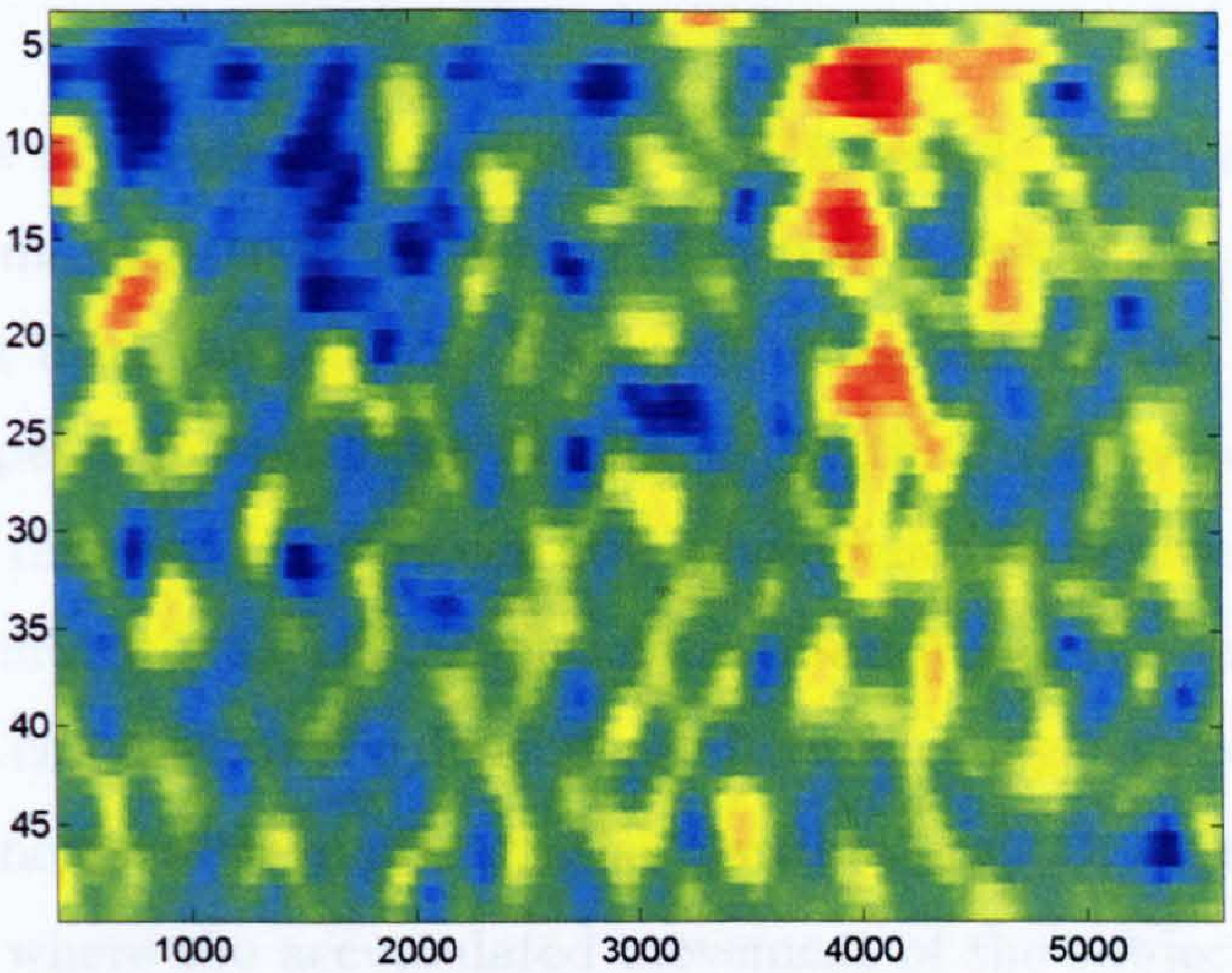

Figure 6.7: The time frequency profile of the second component. The offset of the stimulus is at 4000ms. The horizontal axis stands for time in ms, while the vertical axis is the frequency in Hz.

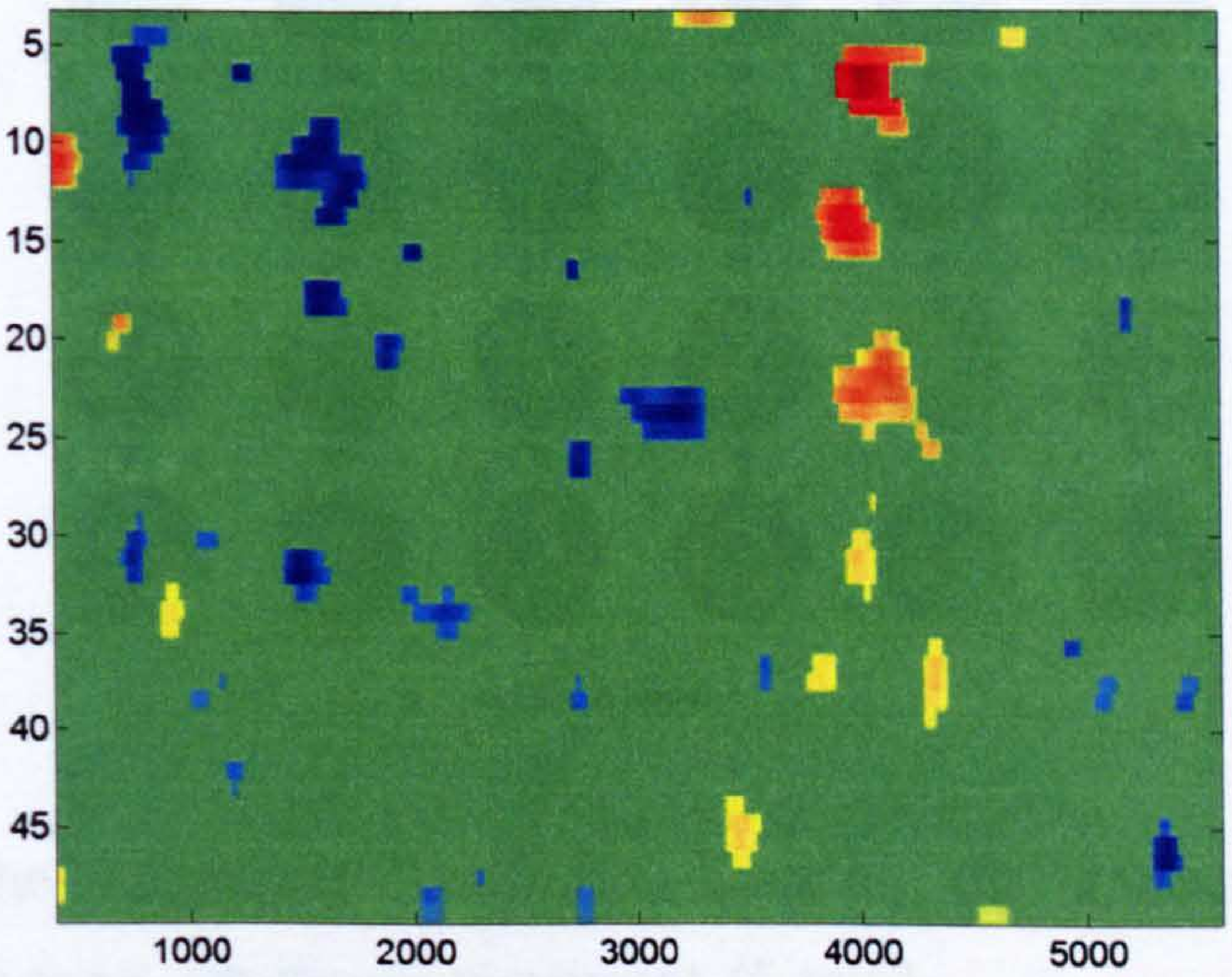

Figure 6.8: The time frequency profile of the second component. The offset of the stimulus is at 4000ms. The horizontal axis stands for time in ms, while the vertical axis is the frequency in Hz. The Bootstrap significance was set to 0.05, with pixels failing to pass the significance test set to zero.

6.5 Discussion

The analysis performed in this study is ICA based, which implies that the source signals remain spatially stationary. The major obstacle to this assumption is the movement from the subject. If subject moves during the experiment, the same source appears in two different places. With a mild movement artefact, these sources at different location can still be modelled as dependent, and resulting one component with inaccurate spatial distribution and time course. However, large movement can destroy the dependence between these sources, and resulting in many components with similar spatial distributions. One example (Fig 6.9) is shown here , where the accumulated movement of the subject during the experiment was just under $5mm$, and it does not appear small enough for ICA to perform successfully.

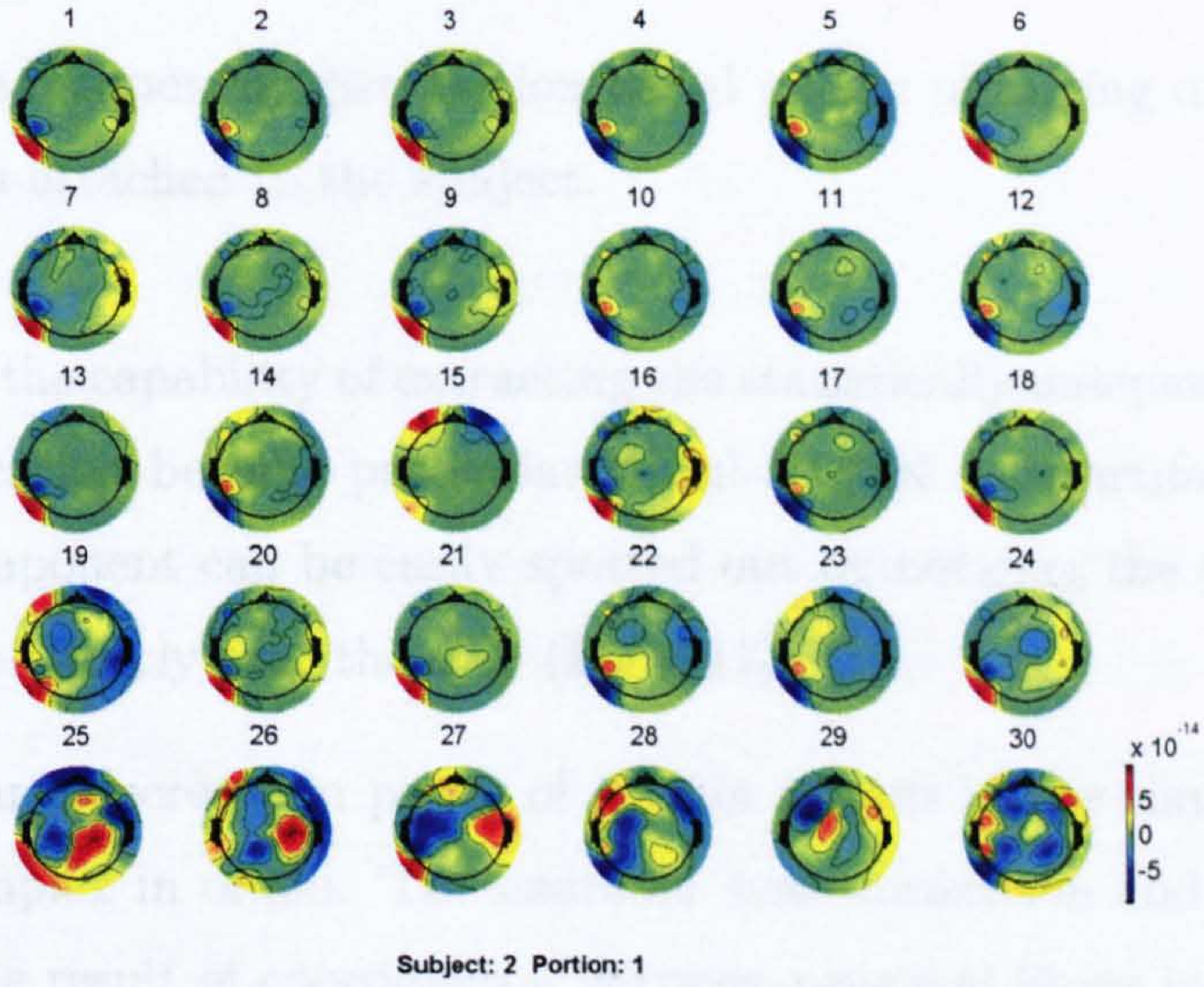

Figure 6.9: The component distribution based on the unmixing matrix when the subject undergoes significant movement (5 mm).

Since MEG is a sensitive equipment to measure neuronal electrophysiological activities, any metal objects can cause strong disturbance to the measurement. This issue is worsened by ICA, since ICA only extract independent components to account for signal variance. Since the disturbance is strong, small movement from the subject can induce large number of components of the similar pattern (Fig 6.10).

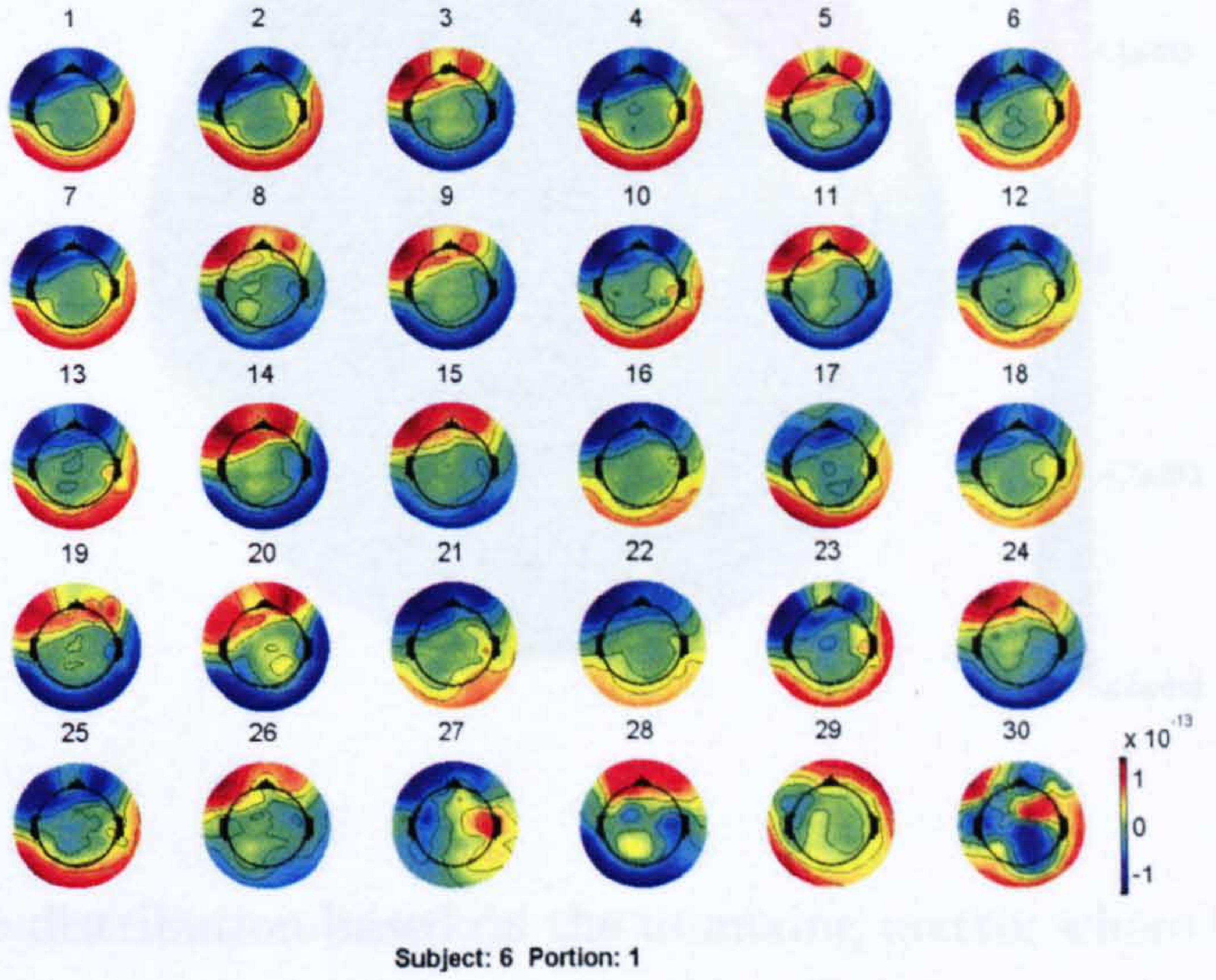

Figure 6.10: The component distribution based on the unmixing matrix when a metal object was attached to the subject.

Since ICA has the capability of extracting the statistically independence components, its application become particular useful to deal with artifacts like eye blinking. This component can be easily spotted out by noticing the distribution of the components directly over the eyes (Fig 6.11).

The increase and decrease in power of certain regions in the time frequency power map, is complex in origin. The neuronal synchronization and desynchronization can be the result of coordination between neuronal fibers in a neuronal bundle, where a synchronized activity causes an increase in the power. This can also result from the breakdown of large cortical network and formation of small networks. It is worth noting that these two explanation does not necessarily contradictory to each other, since logically both can stand at the same time. It is very likely these two explanations are linked as the cause and the result. However, it is still very unclear which one is fundamental.

The available technique is still coarse, and the analysis technique is far from perfect. It is clear that the current technique is still susceptible to artifacts,

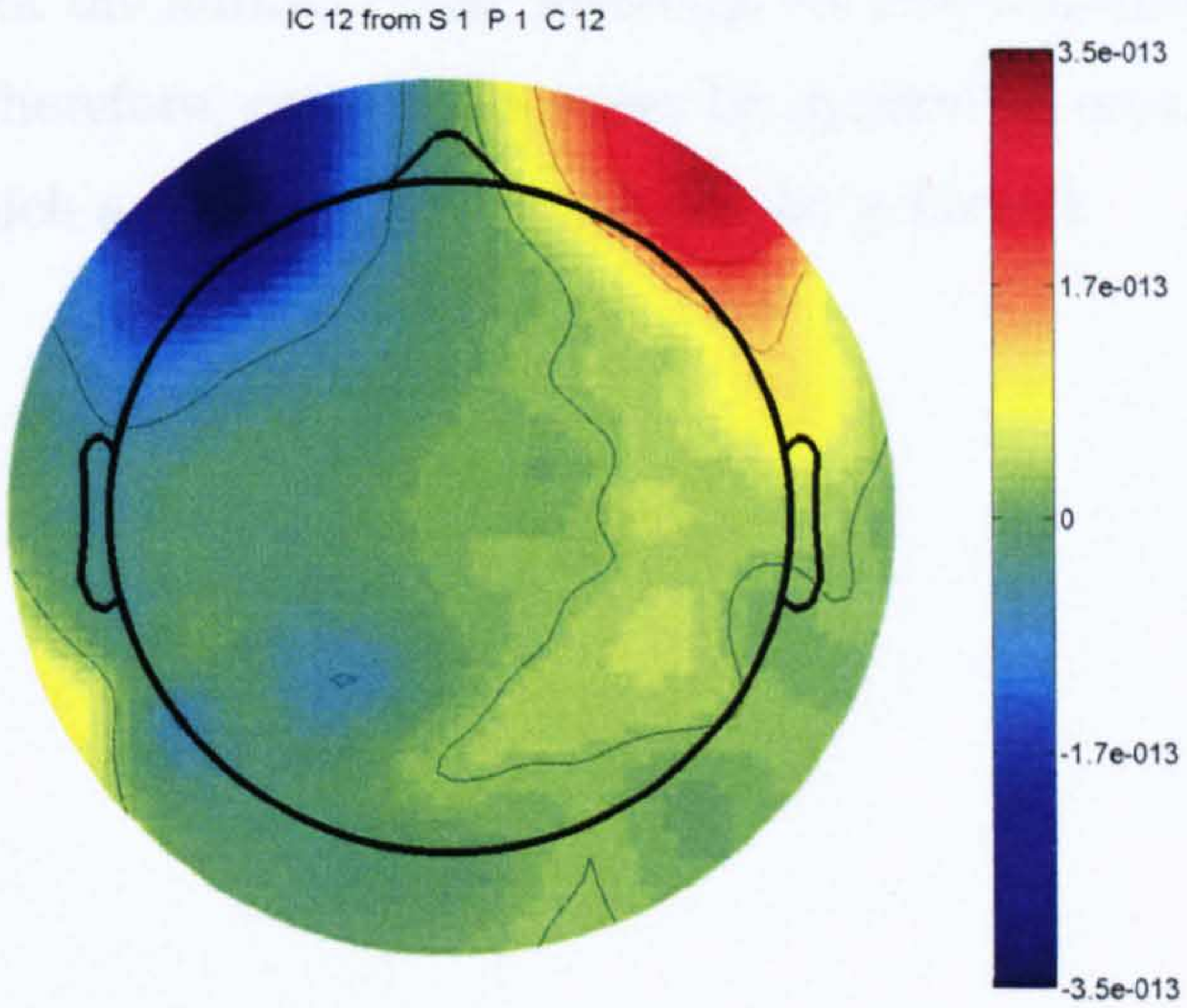

Figure 6.11: The distribution based on the unmixing matrix where the component (IC 12) reflects the eye blinking artefact.

while identifying the correspondence between different subject and portions of data can be challenging. Further algorithms to address this issue is required to facilitate this technique with more prosperity. The limitations mentioned above put an strong restriction on the capability of revealing the insight of neuronal activities and summarizing the general behavior of human brain towards certain stimulus. The complexity of the results is related to the approach of carrying out the analysis. The analysis describe in this study does not concern about the spatial information, but rather the statistical independence between signals. This allows all the components in play to show up, and consequently a high complexity. Although somatosensory system is relatively simple in comparison to other systems in human brain, 30 components perhaps still underestimate the complexity of the mechanism. Since each system in human central nervous system still have connections with other systems, it is likely that other neuronal systems are triggered during the process. Unfortunately this reaction cannot be summarized over the population, because the system triggered and followup processing varies among subjects according to their natural construction of the brain and related previous experiences. This method is therefore useful to expose the full scale dynamics of the human brain, although its practicability can easily become unreachable. Therefore, constraints must be applied to compromise the complexity, through which a explainable answer can be achieved.

Chapter 7

Conclusion

7.1 Thesis Overview

This work ventured through the potential combination between fMRI and MEG. It started with a brief history of fMRI and MEG, and a philosophical debate of the potential benefits of integrating the information provided by both modalities. Subsequently, the theoretical basis of NMR, MRI and fMRI were illustrated to demonstrate the intrinsic features of fMRI measurements. Similarly, the fundamentals of MEG were described together with dipole fitting theory. It was shown through studies that fMRI and MEG present reasonable agreement in the activation pattern induced by a somatosensory tactile stimulus, following conventional analysis techniques. This finding was supported by known neuronal projections, and cortical folding patterns. It was shown that a potential chance exists of mistakenly linking unrelated activation sites between modalities. It was also clear that certain brain activities may be only detected by one of the modalities. Despite these issues, fMRI and MEG showed convincing convergence in discriminating the same brain activities. Unlike spatial combination, the philosophical foundation of performing a temporal combination between two modalities is much weaker. Attempts were made to extract corresponding features from MEG recorded data to match fMRI detection characteristics. To extract a temporal coherent source, ICA was carried out on the basis of lead field theory. Subsequently, a wavelet transform was performed to monitor the time frequency dynamics of the component, providing some indication of the organization of the neuronal network.

During the process of this work, it has become clear that the joint application of fMRI and MEG can certainly provide precious information regarding the mechanisms of the human brain. It also become clear that to account for the observations on both modalities, further understanding of the intrinsic nature of each modality is required.

7.2 Future Development

The motivation of scientific research is the urge to understand a phenomenon, by finding robust solutions to formulated questions. This work was carried out to understand better the mechanism of the human brain, based on a possible establishment of a bridge between hemodynamic and electrophysiological behavior. However, since any modality is only a partial representation of its underlying phenomenon, this ambition appeared to be impractical based on the available equipment and processing techniques. Nevertheless, these studies exposed the insufficiency in the tools, and unveiled the route leading to the final vision.

The underlying mechanisms of BOLD contrast based fMRI are not entirely clear, and the quantification appears incompatible with any of the models proposed. It is therefore more appropriate to adopt other type of fMRI contrast as the metabolic representative of brain activity. The likely candidates for this role are cerebral blood flow and volume, both of which can be measured quantitatively through MR techniques.

Large amounts of data are produced during MEG recording, implying that effective organization and interpretation are crucial for revealing the mechanism of the brain. It is lucky and unfortunate at the same time that a huge variety of analysis techniques is available. Therefore physical meaning should be in focus during the selection of the appropriate method. Facing large quantities of data and a wide range of analysis approaches, an effective and efficient strategy of information abstraction and compressing is of the highest priority.

The combination of fMRI and MEG begins to reveal the true relationship between different aspects of brain activities. Since brain mechanisms dictate the outcome of this model, the fundamentals of brain construction are ready to be exposed. However, with this finer view of brain processes, more questions and puzzles will arise to induce the appetite of scientists to fully appreciate the functions of the human brain.

References

[1] Baule GM, McFee R, *Detection of the magnetic field of the heart*, Am Heart J., 66, 95-96, 1963

[2] Geoge JS, Jackson PS, Ranken DM, Flynn ER, *Three-dimensional volumetric reconstruction for neuromagnetic source localization*, Advances in Biomagnetism, Plenum, New York, 737-740, 1989

[3] Suk J, Cappell J, Ribary U, Yamamoto T, Linás RR, *Magnetic localization of somatically evoked responses in the human brain*, Advances in Biomagnetism, Plenum, New York, 165-168, 1989

[4] Schneider S, Abraham-Fuchs K, Daalmans G, Folberth W, Hoenig HE, Reichenberger H, Röhrlein G, Seifert H, Wirth A, *Development and performance of a multichannel for studies of biomagnetic signals of brain and heart*, Advances in Biomagnetism, Plenum, New York, 669-672, 1989

[5] Hämäläinen M, *Anatomical correlates for magnetoencephalography: integration with magnetic resonance images*, Clin Phys Physiol Meas Suppl A, 12, 29-32, 1991

[6] Malmivuo J, *On the Detection of the Magnetic Heart Vector - An Application of the Reciprocity Theorem*, Acta Polytechnica Scandinavica, Electrical Engineering, 39, The Finnish Academy of Technical Science, Helsinki, 1976

[7] Yamamoto T, Williamson SJ, Kaufman L, Nicholson C, Llinás R, *Magnetic localization of neuronal activity in the human brain*, Proc Natl Acad Sci, USA, 85, 8732-8736, 1988

[8] Meijs J, *The influence of head geometries on electro- and magnetoencephalograms*, PhD thesis, University of Twente, The Netherlands

[9] Hari R, Ilmoniemi J, *Cerebral magnetic fields*, CRC Crit Rev Biomed Eng, 14, 93-126, 1986

[10] Cuffin BN, Cohen D, *Magnetic fields of a dipole in special volume conductor shapes*, IEEE Trans Biomed Eng, BME-24, 372-381, 1977

[11] Cohen D, Cuffin BN, Yunokuchi K, Maniewski R, Purcell C, Cosgrove GR, Ives J, Kennedy JG, Schomer DL, *MEG versus EEG localization test using implanted sources in the human brain*, Ann Neurol, 28, 811-817, 1990

[12] Hari R, Hämäläinen M, Ilmoniemi R, Lounasmaa OV, *MEG versus EEG localization test (Letter to the Editor)*, Ann Neurol, 30, 222-224, 1991

[13] Williamson S, *MEG versus EEG localization test (Letter to the Editor)*, Ann Neurol, 30, 222, 1991

[14] Anogianakis G, Badier JM, Barrett G, Erné S, Femici R, Fenwick P, Grandori F, Hari R, Ilmoniemi R, Mauguiére F, Lehmann D, Perrin F, Peters M, Romani GL, Rossini PM, *A consensus statement on relative merits of EEG and MEG*, Electroencephalogra Clin Neurophysiol, 82, 317-319, 1992

[15] van den Noort, Altrocchi P, Brin MF, Ferguson J, Greenberg J, Jacobs L, Kittredge F, Markham C, Nuwer M, Tindall R, *Assessment: Magnetoencephalography (MEG). Report of the therapeutics and technology assessment subcommittee of the American Academy of Neurology*, 1992

[16] Tripp JH, *Physical concepts and mathematical models*, Biomagnetism: An Interdisciplinary Approach, Plenum, New York, 101-139, 1983

[17] Heller L, *Computation of the return current in encephalography: the auto solid angle*, Digital Image Synthesis and Inverse Optics, Proc SPEE 1351, 376-390, 1990

[18] Helmholtz H von, *Ueber eimige Gesetze der Vertheilung elektrischer Ströme in körperlichen Leitern, mit Anwendung auf die thierisch-elektrischen Versuche*, Ann Phys Chem, 89, 211-233, 355-377, 1853

[19] Meijs JWH, Bosch FGC, Peters MJ, da Silva FHL, *On the magnetic field distribution generated by a dipolar current source situated in a realistically shaped compartment of model of head*, Electroencephalogr Clin Neurophysiol, 66, 286-298, 1987

[20] Nenonon J, Katila T, *Noninvasive functional localization by biomagnetic methods, part I*, J Clin Eng, 16, 423-434, 1991

[21] Hämälänen MS, Sarvas J, *Realistic conductivity geometry model of the human head for interpretation of neuromagnetic data*, IEEE Trans Biomed Eng, 36, 165-171, 1989

[22] Nenonon J, Katila T, *Noninvasive functional localization by biomagnetic methods, part II*, J Clin Eng, 16, 495-503, 1991

[23] van Oosterom A, Strackee J, *The solid angle of a plane triangle*, IEEE Trans Biomed Eng, BME-30, 125-126, 1983

[24] Urankar L, *Common compact analytical formulas for computation of geometry integrals on a basic Cartesian subdomain in boundary and volume integral methods*, Eng Anal Boundary Elements, 7, 124-129, 1990

[25] de Munck JC, *A linear discretization of the volume conductor boundary integral equation using analytically integrated elements*, IEEE Trans Biomed Eng, 39, 956-990, 1992

[26] Barnard ACL, Duck IM, Lynn MS, Timlake P, *The application of electromagnetic theory to electrocardiography, II, Numerical solution of the integral equation*, Biophys J, 7, 463-491, 1967

[27] Lynn MS, Timlake WT, *The use of multiple definition in the numerical solution of singular systems of equations with applications to potential theory*, SIAM J Numer Anal, 5, 303-322, 1968

[28] Horacek BM, *Digital model for studies in magnetocardiography*, IEEE Trans Magn, MAG-9, 440-444, 1973

[29] Ilmoniemi RJ, Hämäläinen MS, Knuutila J, *The forward and inverse problems in the spherical model*, Biomagnetism: Applications and Theory, Pergamon, New York, 278-282, 1985

[30] Arthur RM, Geselowitz DB, *Effect of inhomogeneities on the apparent location and magnitude of a cardiac current dipole source*, IEEE Trans Biomed Eng, BME-17, 141-146, 1970

[31] de Much JC, *The potential distribution in a layered anisotropic spheroidal volume conductor*, J Appl Phys, 64, 464-470, 1988

[32] Blakemore C, , Mechanism of the mind, Cambridge University Press, Cambridge, 1977

[33] Bloch F, Hansen WW, Packard ME, *Nuclear induction*, Physics Review, 69, 127, 1946

[34] Katila TE, *On the current multipole presentation of the primary current distributions*, Nuovo Cimento D, 2, 660-664, 1983

[35] Hayes CE, Edelstein WA, Schenck JF, Mueller OM, Eash M, *An Efficient, Highly Homogeneous Radiofrequency Coil for Whole-Body NMR Imaging at* 1.5T, Journal of Magnetic Resonance, 63, 622-628, 1985

[36] Geselowitz DB, *On the magnetic field generated outside an inhomogeneous volume conductor by internal current sources*, IEEE Trans Magn, MAG-6, 346-347, 1970

[37] Sarvas J, *Basic mathematical and electromagnetic concepts of the biomagnetic inverse problem*, Phys Med Biol, 32(1), 11-22, 1987

[38] Jacks1998on JD, *Classical Electrodynamics, 3rd ed*, John Wiley and Sons, New York, 1998

[39] Wikswo JP Jr, Barach JP, Freeman JA, *Magnetic field of a nerve impulse: First measurements*, Science, 208, 53-55, 1980

[40] Hämäläinen M, Hari R, Ilmoniemi RJ, Knuutila J, Lounasmaa OV, *Magnetoencephalography - theory, instrumentation, and applications to noninvasive studies of the working human brain*, Reviews of Modern Physics, 65(2), 413-497, 1993

[41] Kuffer SW, Nicholls JG, Martin AR, *From Neuron to Brain*, 2nd ed, Sinauer Associates, Sunderland, 1984

[42] Hari R, Hämäläinen H, Hämäläinen M, Kekoni J, Sams M, Tiihonen J, *Separate finger representations at the human second somatosensory cortex*, Neurosci, 37, 245-249, 1990

[43] Mansfield P, Morris PG, *NUM imaging in biomedicine*, Academic Press, New York, 1982

[44] Glover GH, Hayes CE, Pelc NJ, Edelstein WA, Mueller OM, Hart HR, Hardy CJ, O'Donnell M, Barber WD, *Comparison of Linear and Circular Polarization for Magnetic Resonance Imaging*, Journal of Magnetic Resonance, 64, 255-270, 1985

[45] Chmurny GN, Hoult DI, *The Ancient and Honourable Art of Shimming*, Concepts in Magnetic Resonance, 2, 131-149, 1990

[46] Vrba J, *Multichannel SQUID biomagnetic systems*, Applications of superconductivity, Dordrecht, Kluwer Academic Publishers, 61-138, 2000

[47] Fife AA, Vrba J, Robinson SE, Anderson G, Betts K, Burbank MB, Cheyne D, Cheung T, Govorkov SA, Haid G, Haid V, Hunter C, Kubik PR, Lee S, McKay J, Reichl E, Schroyen C, Sekachev I, Spear P, Taylor B, Tillotson M, Sutherling W, *Synthetic Gradiometer Systems for MEG*, IEEE Trans Appl Supercond, 9, 4063-4068, 1999

[48] Chen CN, Hoult DI, Sank VJ, *Quadrature Detection Coils - A Further $\sqrt{2}$ Improvement in Sensitivity*, Journal of Magnetic Resonance, 54, 324-327, 1983

[49] Vaughan TJ, Hetheringtan HP, Otu JO, Pan JW, Pohost GM, *High Frequency Volume Coils for Clinical NMR Imaging and Spectroscopy*, Magnetic Resonance in Medicine, 32, 206-618, 1994

[50] Brazier MAB, *The Historical Development of Neurophysiology*, Handbook of physiology, 1, 1-58, American Physiological Society, Washington, 1959

[51] Cohen D, *Magnetoencephalography: evidence of magnetic field produced by alpha rhythm currents*, Science, 161, 784-786, 1968

[52] Jin J, *Electromagnetic Analysis and Design in Magnetic Resonance Imaging*, CRC Press, 1999

[53] Freeman WJ, *Mass Action of the Nervous System*, Academic, New York, 1975

[54] Seelig J, Burlina AP, *Carbon-13 magnetic resonance in biology and medicine*, Clin Chim Acta, 206, 125-136, 1992

[55] Kraut MJ, Arezzo C, Vaughan HG, *Intracorticál generators of the flash VEP in monkeys*, Electroencephalogr Clin Neurophysiol, 62, 300-312, 1985

[56] Chapman RM, Ilmoniemi RJ, Barbanera S, Romani GL, *Selective localization of alpha brain activity with neuromagnetic measurements*, Electroencephalogr Clin Neurophysiol, 58, 569-572, 1984

[57] Cohen D, *Magnetoencephalography: detection of brain's electrical activity with a superconducting magnetometer*, Science, 175, 664-666, 1972

[58] Scott AC, *Neurophysics*, Wiley, New York, 1977

[59] Pechura CM, Martin JB, *Mapping the brain and its functions*, National Academy, Washington, DC, 1991

[60] Bellivveau JW, Kennedy DN, McKinstry RC, Buchbinder BR, Weisskoff RM, Cohen MS, Vevea JM, Brady TJ, Rosen BR, *Functional mapping of the human brain visual cortex by magnetic resonance imaging*, Science, 254, 716-719, 1991

[61] Turner R, *Gradient coil design: a review of methods*, Magnetic Resonance Imaging, 11, 903-920, 1993

[62] Mugler III JP, Brookeman JR, *Three-dimensional magnetization-prepared rapid gradient-echo imaging (3D MP RAGE)*, Magnetic Resonance in Medicine, 15, 152-157, 1990

[63] Josephson BD, *Possible new effects in superconductive tunnelling*, Phys Lett, 1, 251-253, 1962

[64] Schmitt F, Stehling MK, Turner R, Bandettini PA, *Echo-Planar Imaging: Theory, Technique and Application*, Springer Verlag, 1998

[65] Goldman DE, *Potential, impedance, and rectification in membranes*, J Gen Physiol, 27, 37-60, 1943

[66] Stehling MK, Turner R, Mansfield P, *Echo-planar imaging: Magnetic resonance imaging in a fraction of a second*, Science, 254, 43-50, 1991

[67] Ogawa S, Tank DW, Menon R, Ellermann JM, Kim SG, Merkle H, Ugurbil K, *Intrinsic signal changes accompanying sensory stimulation: Functional brain mapping with magnetic resonance imaging*, Proc Natl Acad Sci, USA, 89, 5951-5955, 1992

[68] Knoll GF, *Single-photon emission computed tomography*, Proc IEEE, 71, 320-329,1983

[69] Kessler RM, Partain CL, Price RR, James E, *Positron emission tomography: Prospectus for clinical utility*, Invest Radiol, 22, 529-537, 1987

[70] Jaszczak RJ, *Tomographic radiopharmaceutical imaging*, Proc IEEE, 76, 1079-1094, 1988

[71] ter-Pogossian MM, Phelps ME, Hoffman EJ, Mullani NA, *A positron emission transaxial tomograph for nuclear medicine imaging (PETT)*, Radiology, 114, 89-98, 1975

[72] Damadian R, *Nuclear magnetic resonance: a noninvasive approach to cancer*, Hosp Pract., 12, 63-70, 1977

[73] d'Arsonval JA, *Dispositifs pour la mésure des courants alternatifs de toute fréquences*, C R Soc Biol, 2, 450-451, Paris, 1896

[74] Zimmerman JE, Thiene P, Harding JT, *Design and operation of stable rf-based superconducting point-contact quantum devices and a note on the properties of perfectly clean metal contacts*, Journal of Applied Physics, 41, 1572-1580, 1970

[75] Griffiths D, *Introduction to Elementary Particles*, Wiley, 1987

[76] Edelstein WA, Hutchison JMS, Johnson G, Redpath TW, *Spin-warp NMR imaging and applications to human whole-body imaging*, Physics in Medicine and Biology, 25, 751-756, 1980

[77] Ernst RR, Anderson WA, *Application of Fourier Transform spectroscopy to magnetic resonance*, Review of Scientific Instrumentation, 37, 93, 1966

[78] Garroway AN, Grannell PK, Mansfield P, *Image formation in NMR by a selective irradiactive process*, Journal of Chemical Physics, C7, L457, 1974

[79] Hahn E, *Spin echos*, Physical Review, 850, 580-594, 1950

[80] Kumar A, Welti D, Ernst RR, *NMR Fourier zeugmatography*, Journal of Magnetic Resonance, 18, 69-83, 1975

[81] Mansfield P, Grannell P, *NMR 'diffraction' in solids?*, J Phys, C6, L422-L426, 1973

[82] Lauterbur P, *Image formation by induced local interactions: examples employing nuclear magnetic resonance*, Nature, 242, 190-191, 1973

[83] Mansfield P, Maudsley P, *Planar and line-scan spin imaging by by NMR*, Proc XIXth Congree Ampere, Heidelberg, 247-252, 1976

[84] Mansfield P, *Mansfield, P. (1977) Multi-Planar Image Formation Using NMR Spin Echoes*, J. Phys. C. 10,L55-L58, 1977

[85] Jallabert J, *Expériences Sur L'électricité Avec Quelques Conjectures Sur La Cause De Ses Effects*, Geneva, 1748

[86] Galvani L, *De viribus electricitatis in motu musculari*, Bononiesi Scientarium et Ertium Instituto atque Academia Commentarii, 7, 363-418, 1791

[87] Matteucci C, *Sur le courant électrique ou propre de la grenouille. Second mémoire sur l'électricité animale, faisant suite à celui sur la torpille*, Ann Chim Phys (2ème série), 67, 93-106, 1838

[88] Matteucci C, *Deuxième mémoire sur le courant électrique propre de la grenouille et sur celui des animaux à sang chaud(1)*, Ann Chim Phys (3ème série), 6, 301-339, 1842

[89] du Bois-ReymondEH, *Vorläufiger Abriss einer Untersuchung ueber den sogenannten Fische*, Ann Physik und Chemie, 58, 1-30, 1943

[90] Caton R, *The electric currents of the brain*, Br Med J, 2, 278, 1875

[91] Beck A, *Opobudiwosciróznych miejsc tego samego nerwu*, Rozpr Wydzprzyr polsk Akad Um, 15, 165-195, 1888

[92] Beck A, *The determination of localization in the brain and spinal cord by means of electrical phenomena*, Polska Akademija Umiejetnosci, Series 2, 187-232, 1891

[93] Berger H, *Über das Elektroenkephalogram des Menschen*, Arch f Psychiat, 87, 527-570, 1929

[94] Gibbs FA, Davis H, Lennox WG, *The clectroencephalogram in epilepsy and in conditions of impaired consciousness*, Arch Neurol Psychiatry, 34, 1133-1148, 1935

[95] Gerlach W, Stern O, *Uber die Richtungsquantelung in Magnetfield*, Zeischrift fur Physik, 8, 110, 1921

[96] Ogawa S, Lee T, Kay A, Tank D, *Brain magnetic resonance imaging with contrast dependent on blood oxygenation*, Proc Natl Acad Sci, 87, 9868-9872, USA, 1990

[97] Pauli JR, , Natturwissenschaften,. 12, 741, 1924

[98] Purcell EM, Torrey HC, Pound RV, *Resonance absorption by nuclear magnetic moments in solids*, Physics Review, 69, 37-38, 1946

[99] Stern O, , Zeischrift fur Physik, 7, 249, 1921

[100] Swammerdam J, *Biblia Nathurae*, 2, 839-850, Leyden, 1738

[101] Jacklevic RC, Lamb J, Silver AH, Mercereau JE, *Quantum interference effects in Josephson tunnelling*, Phys Rev Lett, 12, 159-160, 1964

[102] Anderson AC, Salinger GL, Wheatly JC, *Thermal Conductivity of Liquid He*, Phys Rev Lett, 6, 443-446, 1961

[103] Korvenoja A, Huttunen J, Salli E, Pohjonen H, Martinkauppi S, Palva JM, Lauronen L, Virtanen J, Ilmoniemi RJ, Aronen HJ, *Activation of multiple cortical areas in response to somatosensory stimulation: combined magnetoencephalographic and functional magnetic resonance imaging*, Hum Brain Mapp. 1999;8(1):13-27

[104] Beisteiner R, Gomiscek G, Erdler M, Teichtmeister C, Moser E, Deecke L, *Comparing localization of conventional functional magnetic resonance imaging and magnetoencephalography*, Eur J Neurosci. 1995 May 1;7(5):1121-4.

[105] Moran JE, Drake CL, Tepley N, *ICA methods for MEG imaging*, Neurol Clin Neurophysiol. 2004 Nov 30;2004:72

[106] Makinen VT, May PJ, Tiitinen H, *The use of stationarity and nonstationarity in the detection and analysis of neural oscillations*, Neuroimage. 2005 Nov 1;28(2):389-400. Epub 2005 Jul 15